

AD-A244 504
██████████

PL-FR-91-2193

✓
(2)

20000831/53

AN INVESTIGATION IN ATMOSPHERIC DYNAMICS
AND ITS EFFECTS ON OPTICAL EMISSIONS

T. P. Tuan

University of Cincinnati
Department of Physics
Cincinnati, OH 45221-0011

1 August 1991

DTIC
S ELECTE D
DEC 30 1991
D

Final Report
February 1987-June 1991

APPROVED FOR PUBLIC RELEASE; DISTRIBUTION UNLIMITED




PHILLIPS LABORATORY
AIR FORCE SYSTEMS COMMAND
HANSCOM AIR FORCE BASE, MASSACHUSETTS 01731-5000

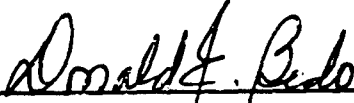
91-19172
██████████

Reproduced From
Best Available Copy

"This technical report has been reviewed and is approved for publication"


RICHARD H. PICARD
Contract Manager


WILLIAM A.M. BLUMBERG
Branch Chief


DONALD E. BEIDO
Acting Division Director

This report has been reviewed by the ESD Public Affairs Office (PA) and is releasable to the National Technical Information Service (NTIS).

Qualified requestors may obtain additional copies from the Defense Technical Information Center. All others should apply to the National Technical Information Service.

If your address has changed, or if you wish to be removed from the mailing list, or if the addressee is no longer employed by your organization, please notify PL/IMA, Hanscom AFB, MA 01731-5000. This will assist us in maintaining a current mailing list.

Do not return copies of this report unless contractual obligations or notices on a specific document requires that it be returned.

REPORT DOCUMENTATION PAGE

Form Approved
OMB No. 0704-0188

Public reporting burden for this collection of information is estimated to average 1 hour per response, including the time for reviewing instructions, searching existing data sources, gathering and maintaining the data needed, and completing and reviewing the collection of information. Send comments regarding this burden estimate or any other aspect of this collection of information, including suggestions for reducing this burden, to Washington Headquarters Services, Directorate for Information Operations and Reports, 1215 Jefferson Davis Highway, Suite 1204, Arlington, VA 22202-4302, and to the Office of Management and Budget, Paperwork Reduction Project (0704-0188), Washington, DC 20503.

1. AGENCY USE ONLY (Leave blank)		2. REPORT DATE August 1, 1991	3. REPORT TYPE AND DATES COVERED Final Report (Feb. 1987 - June 1991)	
4. TITLE AND SUBTITLE An Investigation in Atmospheric Dynamics and Its Effects on Optical Emissions			5. FUNDING NUMBERS PE 61102F PR 2310 TA G5 WU AD Contract F19628-87-K-0028	
6. AUTHOR(S) T. F. Tuan				
7. PERFORMING ORGANIZATION NAME(S) AND ADDRESS(ES) University of Cincinnati Department of Physics Cincinnati, Ohio 45221-0011			8. PERFORMING ORGANIZATION REPORT NUMBER	
9. SPONSORING/MONITORING AGENCY NAME(S) AND ADDRESS(ES) Phillips Laboratory Hanscom AFB, MA 01731-5000 Contract Manager: Richard Picard/OPS			10. SPONSORING/MONITORING AGENCY REPORT NUMBER PL-TR-91-2193	
11. SUPPLEMENTARY NOTES				
12a. DISTRIBUTION/AVAILABILITY STATEMENT Approved for public release; distribution unlimited			12b. DISTRIBUTION CODE	
13. ABSTRACT (Maximum 200 words) This report describes theoretical research and modeling carried out over the period of this contract on the properties of small-scale gravity waves and on the response of mesospheric and lower thermospheric airglow to gravity waves. The work on small-scale waves has shown that the variation of the Brunt period with altitude, combined with Doppler shifting by background winds, can lead to fully guided modes (Brunt-Doppler ducting). The dependence of the modal properties on phase-velocity dispersion, wind shear, viscosity, and instability is investigated. It is also shown that, for small-scale waves, pressure, density, and temperature changes are due primarily to buoyancy forces. Theoretical work on airglow response to gravity waves has emphasized calculation of the nonlinear response of both the airglow volume emission rate and the airglow column brightness to a gravity wave (local and integrated responses). These calculations are carried out in both the Eulerian and Lagrangian frames. Finally, results of observation of OH airglow wave structures in Maui during the ALOHA 90 campaign are described. The above work has been described in several papers in J. Geophys. Res. and Geophys. Res. Lett.				
14. SUBJECT TERMS Atmospheric dynamics, atmospheric waves, acoustic-gravity waves, airglow, airglow structure, OH airglow.			15. NUMBER OF PAGES 200	
			16. PRICE CODE	
17. SECURITY CLASSIFICATION OF REPORT Unclassified	18. SECURITY CLASSIFICATION OF THIS PAGE Unclassified	19. SECURITY CLASSIFICATION OF ABSTRACT Unclassified	20. LIMITATION OF ABSTRACT SAR	

CONTENTS

		<u>PAGE</u>
I.	Introduction	1
II.	Small-Scale Gravity Waves	9
	A. Brunt-Doppler Ducting of Small Period Gravity Waves	
	B. On The Importance Of The Purely Gravitationally Induced Density, Pressure and Temperature Variations in Gravity Waves; Their Application To Airglow Observations.	55
III.	Nonlinear Responses	90
	A. On The Nonlinear Response Of Airglow To Linear Gravity Waves	
	B. Perturbation Treatment of The Nonlinear Response To Linear Gravity Waves	
IV.	Measurements of OH Airglow Wave Structures	167

Accession For	
NTIS CRA&I	<input checked="" type="checkbox"/>
DTIC TAB	<input type="checkbox"/>
Unannounced	<input type="checkbox"/>
Justification _____	
By _____	
Distribution / _____	
Availability Codes	
Dist	Avail and/or Special
A-1	



(I) Introduction

Our primary objective is to report on the investigations of the behavior of small-scale gravity waves; their effects on the fluctuations of mesospheric and lower thermospheric airglow such as the OH infrared bands and the oxygen green lines. This research was carried out under the ARC-AARC airglow modelling program and forms part of the MAPSTAR program which includes the following organizations: The Brigham Young University, the University of Cincinnati, the University of Southampton (England), Utah State University, the University of Western Ontario (Canada) and the Phillips Laboratories.

The theoretical analysis of our part of the investigation have resulted in four papers, two of which have already appeared in the Journal of Geophysical Research, the third has just been accepted by the same Journal, while a fourth has been written up and is now undergoing its final revisions before being submitted, again to the same Journal. The experimental part of our program has also resulted in several papers which have been submitted and accepted by Geophysical Research Letters.

In Section (II), we present two papers which deal with small-scale gravity waves (G.W.) and their effects on spatial-temporal variations in airglow structure.

The first paper, "Brunt-Doppler ducting of small-period gravity waves",

investigates the simultaneous effects of two possible ducting mechanisms on small-period G.W.; mechanisms which enhance spatial-temporal fluctuations. The first mechanism is the ducting produced by variations of the Brunt period with altitude. At low altitudes (below mesopause) the Brunt period is of the order of 5 minutes and it increases to 10-15 minutes in the thermosphere. A gravity wave with period less than say 10 minutes will become evanescent above a certain height level. The downward reflection from such height levels is the only mechanism in the atmosphere that can produce fully guided modes. Other reflection mechanisms such as the inhomogeneous background density and temperature variations can only produce partially guided modes. The second mechanism is the downward reflection from horizontal winds which Doppler shifts the frequency of the wave. We do not consider the case for critical layers when the situation is far more complicated in this report. The combined Brunt-Doppler ducting can produce both the fully and the partially guided modes.

The dispersion of these modes with respect to frequency and wind propagation have been examined. In general, the frequencies of each set of guided modes increase with the phase velocity in a complicated way. With wind dispersions, if the direction of the wave propagation is along the wind direction, the wave period is Doppler-shifted to large values and vice versa. This is expected from the formula for the Doppler-shifted frequency.

Whilst the effects of viscosity have been negligible over nearly all the guided modes, the effects of instability are not negligible for most of the modes. In fact, only in the lowest mode (corresponding to lowest eigenvalue ($1/v_x^2$), or the highest horizontal phase velocity v_x), i.e. the Lamb mode, can the instability be neglected.

After the publication of this paper, we have found an error in our wind profiles, which would make a difference for the higher modes but would make no difference for the lower modes. Since, owing to instability problems with the higher modes, the results would in any case be suspect, there is therefore no good reason for elaborate re-calculations with the corrected profile; the error occurs only at relatively high altitudes.

Simultaneous observations of the low altitude (< 100 km) airglow such as the 557.7 nm OI and the OH bands seem to reveal considerably more short period structures (of the order of minutes) than at higher altitudes (say the 630.0 nm red line). In this part of the report we have shown that such short-period structures can just as easily be produced by the prevalence of short-period ducted wave modes at lower altitudes as by instabilities from larger scale waves.

The second paper (Section II) that deals with small-scale spatial-temporal fluctuations is entitled "On the importance of the purely gravitationally induced density, pressure and temperature variations in gravity waves; their application to

airglow observations". The paper shows that for small-scale gravity waves where $v/c \ll 1$, the variations in pressure, density and temperature are produced primarily by the changes in the background gravitational and buoyancy forces as the air parcel moves up and down in altitude. For such waves the "acoustic component", i.e. the pressure, density and temperature variations generated from the pressure gradient in "purely acoustic wave propagation" play a very small role. The first and primary effect will be hence referred to as G.I.C. (gravitationally induced compression and expansion).

We begin by showing that the three fluctuating variables (pressure, density and temperature) can be explicitly expressed as a sum of two terms, one describing the G.I.C., and the other the "wave motion". The term describing G.I.C. vanishes if we let $g \rightarrow 0$ where g is the acceleration due to gravity, leaving only the "wave motion".

The dependence of three variables on v_x/c are then plotted for different G.W. periods. The results show that for small-scale G.W. (e.g. $v/c < 18\%$) the G.I.C. term by itself accounts for 95% of the temperature and density fluctuations. This permits us to make quick estimates of say height variations in the airglow corresponding to any observed temperature variation. For instance, a 10° temperature variation corresponds to a height variation of 1 km; the simple conversion readily establishes a relation between small-scale temperature and height fluctuations.

In summary, for Section II, we have examined mechanisms such as ducting which can enhance small-scale temporal fluctuations in airglow and we have also separated the G.I.C. from acoustic wave compression to show that the small-scale G.W. is mainly dominated by G.I.C. which can lead to the simple relationships in small-scale fluctuations mentioned above.

In Section III we also present two papers which deal with the nonlinear integrated and local response to a strictly linear G.W. These papers are important to the study of airglow fluctuations because G.W. behavior has often been inferred from the airglow response through assuming that a linear G.W. produces a linear response. If such inferences are in fact unjustified, we need to study G.W. by means other than their indirect effect on some minor species with say a layered background structure. The presence of additional structures in the airglow produced from the nonlinear response should add to our general study of spatial-temporal airglow fluctuations; the fluctuations in this case are produced from nonlinear effects.

We were led to the first work in Section III by the paper of Hines & Tarasick [Planet. Space Sci. 35, 851 (1987)] who showed that unlike radar and lidar observations which measure the local fluctuations at each height level, the ground-based photometer and radiometer measure the integrated airglow that can, at least in first order, allow the large nonlinear local Eulerian response, produced from the steep density gradient of the bottom side of the minor species, to be transformed

away with a Lagrangian transformation. Since the large nonlinear local response from the bottom-side of the minor species structure has often been blamed for the importance of the higher order response terms, such a transformation, which can be realized in the integrated airglow, would seem to indicate two things: (1) in the integrated airglow the higher-order terms are filtered out so that a linear G.W. can only elicit a linear response; (2) in studying G.W. the measurement of integrated airglow would therefore enjoy an advantage over the measurement of local responses, since the former filter out the undesirable nonlinear effects, whilst the latter would show such effects even if they do not exist in the linear G.W. itself.

In this report we have computed the higher order response terms in the Lagrangian frame and found that they remain too large to be ignored. This means that the higher order harmonics should exist in the response even if the G.W. is linear and monochromatic and irrespective of whether the local or the integrated airglow is observed.

We were, however, unable to determine if the large magnitude of the higher order terms is due to the steep vertical density gradient just mentioned. Nevertheless, the assumption that the higher order terms are unimportant and that a linear G.W. can only produce a linear response has to be questioned.

In the second paper in Section III, we have developed a perturbation expansion

for computing the higher-order response terms in the purely Eulerian system. The results again show that the integrated higher-order response terms are important and that they cannot be transformed away either by a Lagrangian transformation or by integration by parts. In this case, the importance of the higher-order terms appears to be connected with the steep density gradient, even though such a connection cannot be established in the Lagrangian system.

We should mention that in general the gravity wave from a ground source always consists of a linear combination of two waves: one is a purely travelling wave along both the vertical and horizontal directions, while the other is stationary along the vertical but travelling along the horizontal direction. The linear combination takes into account both the purely travelling part of the gravity wave and the partial (which may sometimes be very small and sometimes be very large) reflection. The purely travelling part can only be computed in the usual first order response without encountering the problem of secularity which requires renormalization techniques of the KBM (Krylov-Bogolinbov-Mitropolsky), (See also "Averaging Methods in Non-Linear Dynamical Systems, Appl. Math. Sci. (Springer-Verlag) by Sanders and Verhulst). For the present problem, we shall consider only the stationary vertical propagation which does not encounter the secularity problem in any order of response.

Our overall theoretical conclusion for this part of the report is: (1) so long as a minor species is used for determining gravity-wave behavior, the nonlinear response

is always important for an average wave amplitude whether one uses photometer, a riometer, a lidar or radar as probes. In this case only from direct measurements of some major species in hydrostatic equilibrium can one expect the behavior of the response to strictly reflect the G.W. behavior; (2) in measuring the local minor species response (with say either the radar or lidar), the density gradient at the bottom-side of the minor-species layer plays a crucial role in both the linear and the nonlinear response terms, since the gradient cannot be transformed away by an integration by parts as it can be for the first order integrated airglow; (3) for the integrated airglow we are not able to determine if the large nonlinear response in the Lagrangian formulation is caused by the steep gradient, since a nonlinear transformation is required to go from the Eulerian to the Lagrangian system. Further work is needed to clarify this point.

In Section IV we present the imaging of the OH airglow wave structure measured in late March and early April 1990 at Maui, Hawaii. A second set of measurements on April 18-28, 1990 were taken at Haleakala following the success of the first. The results have been submitted to Geophys. Res. Lett. and preprints of these publications are presented in Section IV. The principal investigators for the MAPSTAR portion of the ALOHA 1990 campaign are Drs. M. J. Taylor (Univ. of Southampton) and R. P. Lowe (Univ. of Western Ontario).

II. SMALL-SCALE GRAVITY WAVES

PART A: BRUNT-DOPPLER DUCTING OF SMALL PERIOD GRAVITY WAVES

D. Y. Wang

and

T. F. Tuan

Physics Department, University of Cincinnati

Cincinnati, Ohio 45221

***Permanent Address: Institute of Geophysics, Academia Sinica, Beijing, PRC**

ABSTRACT

The variation of the Brunt period with height leads itself to a natural ducting and filtering mechanism for low altitude short-period gravity waves. We investigate this mechanism in combination with Doppler-ducting produced by the variation in horizontal winds. Both the frequency dispersion at fixed propagation direction and the direction dispersion at fixed frequency have been examined in a COSPAR background atmosphere with zonal and meridional winds.

Our results show that indeed the low altitude short-period gravity waves are not only ducted, but unlike the usual ducting mechanisms due to uneven structure and dissipation which only produce the partially guided modes, this mechanism produces primarily guided modes in the absence of winds and a mixture of fully and partially guided modes with the winds. The wind effects are very large on the higher modes and less significant on the few lowest modes, including the Lamb mode.

Investigations of viscous dissipation, non-linearity and instability have shown that viscosity is unimportant for most altitudes of interest and that non-linearity and instability can play a role for all but the lowest guided modes.

We propose that simultaneous continuous observation of airglow at mesospheric and ionospheric altitudes be made to verify not only the low-altitude Brunt-Doppler ducting for short-period gravity waves, but also the vertical energy distribution of the medium and large-scale TID's.

1. INTRODUCTION

There has been considerable interest in the small to medium scale atmospheric fluctuations with periods in the range of a few minutes to low tens of minutes and horizontal phase velocities in the range of low tens to low hundreds of meters per second. They have been detected through many different techniques including, for instance, the mesospheric and lower thermospheric airglow observations (e.g. Okuda, 1962; Silverman, 1962; Krassovsky and Shagaev, 1974a,b, and 1977; Myrabo et al., 1983, 1984; Peterson, 1979; Freund and Jacka, 1979; Hapgood and Taylor, 1982; Peterson and Adams, 1983; Clairemidi et al., 1985; Jacob and Jacka, 1987; etc.), or the different radar systems (e.g. Manson and Meek, 1980; Manson et al., 1981; Smith and Fritts, 1983; Vincent and Reid, 1983; Meek et al., 1985). The small-scale fluctuations have sometimes been interpreted as instabilities (Hodges, 1967; Tuan et al. 1979; Schoeberl et al., 1983; Klostermeyer and Ruster, 1981, 1984).

In this paper, instead of searching for different possible mechanisms that produce these small-scale fluctuations, we shall make a systematic investigation of short-period gravity waves with periods in the range of the variation of the Brunt period with height, a variation which is in the approximate range of the typically observed periods just mentioned. We will focus our attention primarily on the small-period gravity waves with higher phase velocities.

The purpose for making a study of the short-period linear gravity waves are as follows:

- (1) Power spectrum analyses of simultaneous photometric observations

of mesospheric and lower thermospheric optical emissions such as the 557.7 nm OI, the 730 nm and 790 nm OH band as well as the 1.53 μ m OH radiometric data (taken by Peterson and Pendleton in the 1984 MAPSTAR Campaign) seems to show a surprisingly large number of power peaks with short periods. This would seem to suggest that the higher Fourier components as well as the short period gravity waves play an important role in small-scale atmospheric fluctuations.

(2) Simultaneous observations of 557.7 nm and 630 nm OI by Weinberg et al. (1973) would seem to show that considerably more short period structures occur in the 557.7 nm at lower altitudes rather than the 630 nm in the ionospheric altitudes. Whilst other explanations are possible, we will show that this is consistent with the behavior of the simple short-period linear gravity wave theory.

(3) The theoretical justification for our investigations is based on the fact that so far the treatment of gravity wave ducting has been confined to three particular mechanisms: the variation in atmospheric structure (e.g. Francis, 1975 etc.); the variation in dissipation (Richmond, 1978; Yu et al., 1980; Tuan and Tadic, 1982); and the variation in background winds (Chimonas and Hines, 1986). We have found that there exists another type of ducting mechanism valid only for gravity waves, or higher Fourier components of gravity waves with periods in the range of the Brunt period (about 4.5 min at low altitudes to 15 min at higher altitudes). This variation in the Brunt period with height allows a low altitude gravity wave with initial Fourier period component greater than its local Brunt period to propagate upwards to some height level, z_0 , where it becomes equal to the local Brunt period (Fig. 1). The resulting

downward reflection together with the upward reflection from the rigid ground would produce a series of guided modes for each such Fourier frequency component, leaving only the much lower frequency components to continue their upward propagation. Thus, the variation in the Brunt frequency curve could serve as a ducting-filtering mechanism (Wang and Tuan, 1985, 1986) which filters out and restricts the higher frequency components to only the lower altitudes (from now on to be referred to as Brunt ducting).

Whilst the acoustic wave branch can readily propagate at higher frequencies above $z = z_0$, there is no way, of course, that a gravity wave can turn into an acoustic wave, since the latter requires a horizontal phase velocity greater than the local speed of sound. In a horizontally stratified atmosphere, the horizontal phase velocity can not vary with height. Thus, for $z > z_0$ the short-period gravity waves become evanescent. The further requirement of finite energy source would limit the high altitude solutions to those which are "exponentially decaying" and which in turn limit the propagation modes to only the fully guided modes.

Because the horizontal winds will always have an important effect above 80 km, we will in this paper combine the Doppler ducting of Chimonas and Hines (1986) and the Brunt ducting (Wang and Tuan, 1985 and 1986) to produce a simultaneous ducting mechanism which can produce both the fully and the partially guided modes and which will be referred to as the Brunt-Doppler ducting mechanism for short (see also Wang and Tuan, 1987). The zonal and meridional wind profiles of Forbes and Gillette (1982) based on the background mean circulation wind profiles of Lindzen and Hong (1974), and Roble et al. (1977) will be used for the horizontal wind profiles. The

COSPAR model will be used for general background atmosphere.

In Section 2 we shall develop and describe the fundamental equations, the boundary conditions and the methods of solution. In Section 3 we shall present the solutions for the case when the wind is absent and the guidance is provided by Brunt ducting alone. The dispersion curves for the fully guided modes at different gravity wave periods and the kinetic energy density will be given as functions of z , the altitude, (Fig. 4-a and b) for the various discrete fully guided modes.

In Section 4, we include the wind profiles (Fig. 5-a and b) and will discuss the effects of the zonal and meridional winds on the different directions of wave propagation. Dispersion curves as a function of periods for different propagation directions will be given and compared with the dispersion curves for the windless case (Fig. 8-a,b and Fig. 9-a,b). We also show the dispersion curves as a function of propagation direction at fixed period (Fig. 10-a,b).

In Section 5, we consider the effects of stability and dissipation of the different propagation modes, the range of vertical and horizontal wave lengths for which neither effect is significant. In Section 6 we present the conclusion.

2. FUNDAMENTAL EQUATIONS

The differential equations governing the propagation of gravity waves in a horizontally stratified atmosphere whose temperature and horizontal wind velocity vary in an arbitrary manner with height have been derived by Pitteway and Hines (1965). Choosing the pressure perturbation Δp and the vertical velocity perturbation Δw as dependent variables, the system of equations can be transformed into two coupled first-order equations given by

$$\begin{aligned} \frac{\partial \psi}{\partial z} - \eta \psi &= i \frac{\omega}{\Omega} (\omega_b^2 - \Omega^2) (\Delta \bar{w}) \\ \frac{\partial (\Delta \bar{w})}{\partial z} + \left[\eta + \frac{k_x}{\Omega} \frac{\partial V_{0x}}{\partial z} \right] (\Delta \bar{w}) &= i \frac{\Omega}{\omega} \left(\frac{k_x^2}{\Omega^2} - \frac{1}{c_0^2} \right) \psi \end{aligned} \quad (1)$$

where Ω is the Doppler-shifted frequency that would be measured in a coordinate system moving with the atmosphere. It is a function of height through the presence of horizontal wind component, $V_{0x}(z)$. ω is the wave frequency in a fixed coordinate system. They are related by

$$\Omega = \omega - k_x V_{0x} \quad (2)$$

The variables ψ , $\Delta\bar{w}$ and η defined by

$$\psi = \frac{\omega}{\rho_0^{1/2}} \Delta p \quad (3)$$

$$\Delta\bar{w} = \rho_0^{1/2} (\Delta w) \quad (4)$$

$$\eta = - \frac{1}{2} \left(\frac{g}{c_0^2} - \frac{\omega_b^2}{g} \right) \quad (5)$$

and the Brunt frequency ω_b given by

$$\omega_b^2 = - g \left(\frac{1}{\rho_0} \frac{\partial \rho_0}{\partial z} + \frac{g}{c_0^2} \right) \quad (6)$$

The other quantities have their usual meaning.

Eq. (1) is subject to the following assumptions and limitations: (1) the effects of viscosity, thermal conduction and source terms are neglected; (2) the ambient atmosphere is horizontally stratified, all unperturbed quantities have z -dependence only; and (3) the perturbations are small so that the nonlinear terms can be omitted, and all perturbation quantities can be Fourier-decomposed into monochromatic plane waves given by

$$f(x, z, t) \propto f(z) \exp [i (\omega t - k_x x)] \quad (7)$$

The height-varying background winds are assumed to be horizontal, including zonal and meridional components, V_{0z} and V_{0m} , respectively. Since the vertical wind is generally much less than the horizontal winds, it would seem reasonable to simplify the discussion by neglecting the

vertical wind. The fact that the wind perpendicular to the wave vector has no effects at all on the wave propagation allows us to consider only the wind along k_x , the direction of wave propagation. Thus, from Fig. 2, we may write

$$V_{0x} = V_{0z} \cos \alpha + V_{0m} \sin \alpha \quad (8)$$

where α is the angle between k_x and the East direction.

There may be a critical height level where the horizontal phase speed equals the wind speed, and $n = 0$. The solutions of the Eq. (1) are singular (Lin, 1955) due to the fact that, for harmonic wave trains, the inviscid equations introduce infinite shears at the critical level. This implies that in the neighborhood of such a level viscous force cannot be ignored. The singularity may also be circumvented by dealing with transient wave packets (Tolstoy, 1973). Such a theory remains to be fully developed, and attention at the present time is confined to those modes which do not encounter a singular level at any height.

To solve the equations appropriate boundary conditions are required. At the rigid ground boundary the vertical velocity must vanish. In the upper half space temperature and wind can be viewed as constant (Fig. 1 and 5-a,b), the energy propagation has to be only upward at $z \rightarrow \infty$. Thus, the radiation condition must be satisfied at infinity (Reddy, 1969; Francis, 1974). With the help of Eq. (1) these conditions can be expressed as

$$\left[\frac{\partial \psi}{\partial z} - \eta \psi \right]_{z=0} = 0 \quad (9)$$

and

$$\psi(z \rightarrow \infty) \propto \exp(ik_m z) \quad (10)$$

where k_m is the vertical wave number for the upper half space with constant temperature and wind.

For a given atmospheric model Eq. (1) can be numerically solved by full wave computations under the boundary conditions of Eqs. (9) and (10) for the range of horizontal phase velocities we consider in this paper.

3. WINDLESS MODES IN THE COSPAR ATMOSPHERE

In order to understand the Brunt ducting mechanism for small-period gravity waves in a realistic atmosphere, we first consider an atmospheric model without wind. The 1972 COSPAR temperature profile with an exospheric temperature of 1000 °K is used in the present calculation. The upper boundary, above which the atmosphere is assumed to be uniform, is fixed at 400 km.

The phase velocity dispersion curves for the atmosphere are shown in Fig. 3. Each curve represents a mode labelled by the node number in parenthesis on the right-hand side of Fig. 3. The discrete modes indicated by short dash lines can be viewed as bound states. Since, in general, the eigenvalues are proportional to inverse horizontal phase velocity (Yu et al., 1980), we plot these discrete modes against decreasing velocity. The modes with the same nodes are connected by solid lines, and the Lamb modes as pseudomodes (Press and Harkrider, 1962; and Pfeffer and Zarichny, 1963) are connected by dotted lines. The Lamb modes have horizontal phase velocity of about 316 m/sec, and are nearly non-dispersive. The modes with lower phase velocities are ducted between the ground and the lower thermosphere, and can become highly dispersive at the low velocity end.

Fig. 4-a gives the first few solutions of wave function, ψ , for wave period $T = 6$ min. The mode number assigned to each mode is equal to node number of the mode, including the infinity as a node. It can be seen that ψ decays to zero very quickly above 160 km, and the waves are guided by the ground and the thermospheric temperature gradient.

The time-averaged kinetic energy per unit volume, associated with the wave perturbation, is given by

$$E = \frac{1}{4} \rho_0 [|\Delta u|^2 + |\Delta w|^2] \quad (11)$$

where Δu is the horizontal velocity perturbation. The energy densities for all ducted modes with periods of 4.5 - 14 min are concentrated at low altitudes either near the ground or near the lower thermosphere. Fig. 4-b shows the results for $T = 6$ min.

4. PROPAGATION MODES IN WINDY ATMOSPHERE

The zonal and meridional wind profiles used in the present study are shown by the bold lines in Fig. 5-a and b. They are given for the winter solstice at mid-latitude (42° N) and at local midnight. The East is taken as positive for the zonal wind component, while the North is taken as positive for the meridional wind component. These wind components are taken from Forbers and Gillette (1982) whose calculations are in turn based on the mean circulation components (given by the thin line in Fig. 5-a and b) provided by Lindzen and Hong (1974) and Roble et al. (1977). These wind components may be taken as time-independent due to the rather short-period waves we consider in comparison with the tidal periods. It is somewhat unfortunate that the region of greatest importance (80 - 120 km) in the present paper is also a region of some uncertainty in the wind profiles due to boundary effects. Some modification of the winds was performed to allow for a smooth merging with profile below 100 km. The new "CIRA" model (MAP Handbook (1985)) would help. The temperature profile is the same as that described in Section 3.

For the windy atmosphere, model solutions have been computed for wave periods at $T = 4.5, 5.5, 6, 8, 10, 12, 14$ min at propagation direction angle $\alpha = 0^\circ, 30^\circ, 45^\circ, 60^\circ, 90^\circ, 120^\circ, 135^\circ, 150^\circ, 180^\circ, 210^\circ, 225^\circ, 240^\circ, 270^\circ, 300^\circ, 315^\circ$ and 330° . The presence of wind and the resulting Doppler frequency shift (Eq. 2) can sufficiently alter the background atmosphere to allow some fully guided modes to change into partially guided modes. We will specifically consider two cases to show how the effect of the winds can change fully ducted into partially ducted modes. The maximum wind

speeds in the wind profiles of Fig. 5-a and b would restrict our present treatment to gravity waves with horizontal phase velocity greater than 150 m/sec to avoid the singularities generated by critical layers already mentioned in Section 2.

Fig. 6-a,b and Fig. 7-a,b show the wave function ψ and the kinetic energy density for the 6 min modes at $\alpha = 0^\circ$ (Eastward propagation) and 90° (Northward propagation), respectively. As can be seen, the presence of the wind system greatly modifies the properties of wave guidance. Some modes with lower horizontal phase velocities become partially ducted (Figs. 6-a and b). The energy densities of the fully ducted modes are concentrated in the region below 120 km, much lower than that for the windless modes. This is caused by the rapid increase in the wind system with height which can substantially reflect wave energy downwards to lower altitudes. The horizontal phase speeds of the wave modes (as measured in a fixed coordinate system) are also much altered by the presence of the wind profiles. The effect of wind structure is quite significant even for the non-dispersive Lamb modes with a high horizontal phase velocity V_{phx} .

The dispersion curves for the variation in the modal horizontal phase velocity with different wave periods at each propagation direction, and the curves for the variation in modal phase velocity with different propagation directions at each fixed period are compiled but will not all be shown due to lack of space. Here we show the dispersion curves for $\alpha = 0^\circ, 180^\circ$ (Figs. 8-a,b), $90^\circ, 270^\circ$ (Figs. 9-a,b), and the directional variation curves of phase velocities for $T = 6$ and 14 min (Figs. 10-a,b). The other curves have characteristics similar to these more extreme cases. In addition to the notations and symbols defined for Fig. 3 in Section 3, a

"+" sign is used to indicate partially ducted modes.

The dispersion curves in Fig. 8-a and b show the ducted modes when the propagation direction is along the direction of the zonal wind ($\alpha=0^\circ$), and against the zonal wind ($\alpha = 180^\circ$). Compared to Fig. 3, the only possible similarity is the behavior of the Lamb mode which continues to be relatively non-dispersive, although the phase speed is shifted from 316 m/sec to 337 m/sec for $\alpha = 0^\circ$ and 296 m/sec for $\alpha = 180^\circ$. This is to be expected, since the zonal wind has a more or less constant magnitude of about 20 m/sec from the ground up to about 30 km, a height range where a significant portion of the Lamb mode energy is located. In other respects, Fig. 8-a looks quite different from Fig. 3. Owing to Doppler wind shift, no fully ducted modes can be found for waves with periods greater than 8 min. Fig. 8-b bears some resemblance to Fig. 3, and shows the existence of fully ducted modes for waves with periods up to 14 min. The physics behind it is that for $\alpha = 0^\circ$ the waves, propagating always in the direction of the background wind, can be Doppler shifted by the wind to longer periods which leads to reducing the reflection, and allowing greater energy leakage upwards into higher altitudes. Thus, the waves with periods greater than 8 min are no longer fully ducted. At the short period end of wave spectrum, however, some waves with periods less than 4.5 min (the lower limit of the Brunt period) may be shifted to form fully ducted gravity wave modes. For $\alpha = 180^\circ$ the wave propagation is opposite to the wind. The wave period is shifted to the shorter end, and the wave reflection and ducting become enhanced. In this case, even waves with period greater than 14 min (the upper limit of the Brunt period) can be turned into fully guided modes.

The dispersion curves in Fig. 9-a and b are due to purely meridional

wind. They bear more similarity to Fig. 3. The phase speeds for the Lamb modes are nearly the same as that in the windless atmosphere, although quite significant differences can appear for other modes with lower phase velocities. We point out that while the meridional wind in the region around 100 km has amplitudes as large as zonal wind (Fig. 5-a,b), its effect on the wave guidance are much weaker. This can be understood in terms of the general pattern of meridional wind which reverses itself at different height levels in a symmetric way. The wind reversals cancel out much of the effects of Doppler shifting that the more mono-directional zonal wind can produce. Nevertheless, the cancellation is not complete, and the effects of meridional wind can not be ignored at all, particularly where lower phase-velocity waves are concerned.

Fig. 10-a and b show the directional dispersion of the guided modes at fixed periods (6 min and 14 min, respectively). The relative symmetry of the modes about $\alpha = 180^\circ$ is due again to the meridional wind pattern. The rise of the modes and hence a lowering of the phase velocity as α increases from zero in Fig. 10-a can again be understood in terms of the dispersion relation which provides for lower horizontal phase velocity as α increases through Doppler shift. Once again, the change in phase velocity is the least for the Lamb mode which is sufficiently concentrated at lower altitudes where the variation with height of either the zonal or the meridional wind is relatively small. The preponderance of modes near $\alpha = 180^\circ$ for the 14 min wave (Fig. 10-b) and near $\alpha = 0^\circ$ or 360° for the 6 min wave can again be understood in terms of Doppler wind shift. The longer period modes can only be Doppler wind shift. The longer period modes can only be Doppler-shifted to the higher frequency end and hence require winds

at $\alpha = 180^\circ$, whilst the shorter-period modes can be more readily Doppler-shifted to the lower frequency end and hence require $\alpha = 0^\circ$ or 360° .

5. STABILITY OF THE WAVE MODES

All dissipations and nonlinear effects have been ignored so far. To determine the conditions for which a linear, inviscid wave is a good approximation, and the conditions for which nonlinearity and dissipations would have to be included, the inertial, nonlinear, and viscous terms have been calculated in terms of the linear, inviscid modal solutions. The data of viscosity coefficient are taken from the model used by Midgley and Liemohn (1966). The Richardson's number given by

$$R_i = \frac{\omega_b^2}{\left| \frac{\partial (\Delta u + V_{0x})}{\partial z} \right|^2} \quad (12)$$

has been computed to investigate the possibility for instabilities to occur. In all our calculations the gravity waves have been normalized to density fluctuation of 20%, 15%, and 10% at a height of 100 km.

In the windless atmosphere for guided modes with period less than 9 min the nonlinear term is much less than the inertial term at lower altitudes as expected. The same is true at higher altitudes, where the waves have purely imaginary vertical wave numbers with values greater than $1/2H$ (H is scale height), and decay very quickly so that their amplitudes are limited to small values. The nonlinear term, however, can be comparable to the inertial term around 120 - 140 km. The viscous term below 240 km is much less than the nonlinear term, and can be neglected. Viscosity becomes important at very high altitudes, but does not affect the guided modes too much, since their wave energy is confined to lower

altitudes. The Richardson's numbers of these wave modes are always much greater than one quarter at all altitudes. Thus there is no chance for instability to occur. Fig. 11-a and b show the three terms and the Richardson's number for the 5.5 min windless mode with phase velocity of 72 m/sec at density variation of 20%.

For the modes with periods greater than 9 min in the windfree case, the nonlinear term becomes much larger than inertial term above 100 km, quite different from the previous case, since the wave may not decay fast enough to balance the exponential growth due to the decrease of the background density. The viscous term which is always less than the nonlinear term can still be ignored, but becomes comparable to the inertial term at higher altitudes. The Richardson's numbers at some height levels are less than one quarter, and instability can arise at these levels.

The presence of wind will change the phase velocity of the modes and, in consequence, greatly affect the stability of such modes. Calculations show that only the Lamb modes of 4.5 - 14 min period propagating in any direction can still be viewed as stable in the presence of winds. Stability of other modes with lower phase speeds strongly depends on wave period, horizontal phase velocity, and propagation direction. For $\alpha = 0^\circ$ only waves with periods less than 6 min can have one or more other stable modes with lower phase speed. The numbers of stable modes increase as wave period decreases. The same thing happens at periods less than 12 min for $\alpha = 180^\circ$. In the case of purely meridional wind, each period within 4.5 - 14 min can have one or more stable modes other than the Lamb mode. The lower limit of the horizontal phase velocity for stable modes, roughly speaking, is around 180 - 200 m/sec. Figs. 12-a,b and 13-a,b display the

three terms and the Richardson's numbers for 5.5 min wave with phase speed of 260 m/sec ($\alpha = 0^\circ$), and 12 min wave with phase speed 210 m/sec ($\alpha = 180^\circ$) respectively. Those modes are stable even for the relative density fluctuation of 20% at 100 km.

In conclusion, in the real atmosphere with arbitrarily varying wind system, one would expect that only waves with periods less than 6 min and horizontal phase velocity greater than 200 m/sec can occur more frequently as stable, fully ducted modes. These are consistent with the experimental results mentioned in Introduction of this paper. More detailed discussion about implication of the theory to experiments will be presented in other papers.

6. CONCLUSION

We have found and investigated a ducting mechanism, the Brunt Ducting, valid only for gravity waves with periods in the range of the Brunt period. Unlike structural ducting or dissipative ducting, the Brunt ducting can by itself produce fully guided modes. The only other mechanism that can do so is the Doppler ducting when the wind velocity along the direction of wave propagation exceeds the phase velocity. The combined Brunt-Doppler ducting can produce both the fully and the partially guided modes. We have numerically computed both these modes with a COSPAR atmospheric model and the horizontal wind profiles of Forbes and Gillette (1982), Lindzen and Hong (1974), and Roble et al. (1977). The dispersion of these modes with wave period at fixed propagation direction and with propagation direction at fixed period have both been investigated. We have also investigated the effects of viscosity, non-linearity and dissipation for all the guided modes. In general, we have found the following results:

- (1) In the absence of horizontal winds the guided modes with periods shorter than 8 min are confined to the lower atmosphere below 160 km.
- (2) In the presence of winds everything depends on the direction of horizontal wave propagation. If the wave propagates along the direction of the zonal wind (due East), then the wave period is Doppler-shifted towards the longer periods and many of the higher modes (small horizontal phase velocity) would have their wave energy spread over a much greater height range. If the wave propagates along the direction of the meridional wind (due North), then the North-South symmetry of the meridional wind pattern has considerably less effect on the guided modes whose wave energy remains

in more or less the same location as the windless case (i.e. below 160 km for periods less than 8 min). If the wave propagates against the direction of the zonal wind (due West), then the wave periods are shifted to the shorter period end and only one or two lower modes (high horizontal phase velocity) can exist with most of their energy located below 80 km. Thus, the net effect of the winds is to increase the spread of the wave energy over a greater height range when the propagation is along the wind and decrease it when the propagation is against the wind.

(3) The winds also have an effect on the frequency dispersion of the guided modes. If the wave propagates due East, only the short-period modes survive; the longer period ones have been Doppler-shifted out of existence. If it is due North, then the dispersion curves would resemble the windless case due again to the symmetry of the meridional wind. The dispersion with respect to propagation direction at a fixed but short period (6 min, Fig. 10-a) shows that a number of modes vanishes if the propagation is due West when most of the higher modes are again Doppler-shifted out of existence. The opposite is true for the dispersion curve at a fixed, but relatively long period (14 min, Fig. 10-b). In this case the higher modes tend to survive only if the propagation is due West when there is room for Doppler-shifting to shorter periods.

(4) The computations for the effects of viscosity, non-linearity and instability seem to show that the viscosity is unimportant for most height ranges of interest. In general, within a height range between 110 km and 180 km, the non-linearity and instability can be important for many of the higher modes. The importance decreases with small wave amplitudes as expected. For reasonable wave amplitudes (say waves which produce 15-20%

fluctuations in the major species at 100 km) the non-linearity and instability can be totally neglected only for the Lamb mode with a horizontal phase velocity of almost 315 m sec^{-1} . For other modes they can be neglected for some horizontal phase velocities when the wave amplitudes happen to be moderate in the height ranges mentioned. So far as experimental observations are concerned, for most of our calculations we have found that the mesospheric airglow peaks at height levels well below the region where viscosity, wave instability and non-linearity become important for gravity waves, (we deal with horizontal phase velocity higher than 100 m/sec in this paper to avoid the singular solutions produced by critical layers mentioned earlier in the paper).

We would like to suggest doing simultaneous airglow observations at mesospheric and lower thermospheric height levels (e.g. 557.7 nm OI, the OH emission bands, etc.) and the ionospheric height level (e.g. the 630 nm OI). The data should be taken at short time intervals ($< \text{min}$) to accommodate the short-period structure. This can provide us with information on the energy distribution of the short-period ducted waves which, as we have shown, would concentrate at lower altitudes. They can also provide verification on the long-period and large-scale TID's produced by waves whose energy distribution is concentrated well above 100 km (Thorne, 1968; Yu et al., 1980). So far as we know Thorne's (1968) radar observation at Arecibo was the only confirmation of such an energy distribution for large-scale TID's and that no airglow observations have ever provided such evidence.

ACKNOWLEDGEMENT

We would like to thank Drs. R. Picard, E. Dewan, and J. Winick for some helpful discussions. One of us, (D. Y. Wang) was partially supported by N.S.F. (INT-8412200). The other (T. F. Tuan) was partially supported by a grant from AFGL (F19628-87K-0026). We would also like to thank Drs. R. G. Roble and J. M. Forbes for help in the construction of our wind profiles.

REFERENCES

- Chimonas, G., and C. O. Hines, Doppler ducting of atmospheric gravity waves, *J. Geophys. Res.*, 91, 1219, 1986.
- Clairemidi, J., M. Herse, and G. Moreels, Bi-dimensional observation of waves near the mesopause at auroral latitudes, *Planet. Space Sci.*, 33, 1013-1022, 1985.
- Forbes, J. M., and D. F. Gillette, A Compendium of Theoretical Atmospheric Tidal Structures, Part 1: Model Description and Explicit Structures Due to Realistic Thermal and Gravitational Excitation, AFGL-TR-82-0173 1982. ADA125720
- Francis, S. H., Global propagation of atmospheric gravity waves: A review, *J. Atmos. Terr. Phys.*, 37, 1011, 1975.
- Francis, S. H., A theory of medium-scale traveling ionospheric disturbances, *J. Geophys. Res.*, 79, 5245, 1974.
- Freund, J. T., and F. Jacka, Structure in the 557.7 nm [OI] airglow. *J. Atmos. Terr. Phys.*, 41, 25, 1979.
- Hapgood, M. A., and M. J. Taylor, Analysis of airglow image data, *Ann. Geophys.*, 38, 805, 1982.

- Hodges, R. R., Generation of turbulence in the upper atmosphere by internal gravity waves, *J. Geophys. Res.*, 72, 3455, 1967.
- Jacob, P. G., and F. Jacka, Manifestation of atmospheric gravity waves in the airglow at 95 km, in press, 1987.
- Klostermeyer, J., and R. Ruster, *Adv. Space Res.*, 4, 79, 1984.
- Klostermeyer, J., and R. Ruster, *J. Geophys. Res.*, 86, 6631, 1981.
- Krassovsky, V. I., and M. V. Shagaev, Optical method of recording acoustic or gravity waves in the upper atmosphere, *J. Atmos. Terr. Phys.*, 36, 373, 1974a.
- Krassovsky, V. I., and M. V. Shagaev, *Planet. Space Sci.*, 22, 1334, 1974b.
- Krassovsky, V. I., and M. V. Shagaev, On the nature of internal gravitational waves observed from hydroxyl emissions, *Planet. Space Sci.*, 25, 200, 1977.
- Lin, C. C., *The Theory of Hydrodynamic Stability*, Cambridge Univ. Press, London, 1955.
- Lindzen, R. S., and S. Hong, Effects of mean winds and horizontal temperature gradients on solar and lunar semidiurnal tides in the

atmosphere, J. Atmos. Sci., 31, 1421, 1974.

MAP, (Middle Atmospheres Program Handbook, Vol. 16, Ed. K. Labitzke,
J. J. Barnett and B. Edwards.

Manson, A. H., C. E. Meek, Gravity waves of short period (5 - 90 min)
in the lower thermosphere at 52° N (Saskatoon, Canada) 1978/1979, J.
Atmos. Terr. Phys., 43, 35-44, 1981.

Meek, C. E., I. M. Reid, and A. H. Manson, Observations of mesospheric
wind velocities, 1, Gravity wave horizontal scales and phase
velocities determined from spaced wind observations, Radio Sci., 20,
1363, 1985.

Midgley, J. E., and H. B. Liemohn, Gravity waves in a realistic
atmosphere, J. Geophys. Res., 71, 3729-3748, 1966.

Myrabo, H. K., C. S. Deehr, and G. G. Sivjee, Large amplitude nightglow
OH (8-3) band intensity and rotational temperature variation during a
24 hour period at 78°N, J. Geophys. Res., 88, 9255-9259, 1983.

Myrabo, H. K., and C. S. Deehr, Mid-winter hydroxyl night airglow
emission intensities in the northern polar region, Planet. Space Sci.,
22, 263-271, 1984.

Okuda, M., A study of excitation processes in night airglow, Sci., Rep.,

Tohoko Univ., 15, 9, 1962.

Peterson, A. W., Airglow events visible to the naked eye, Appl. Opt.,
18, 3390-3393, 1979.

Peterson, A. W., and G. W. Adams, OH airglow phenomena during 5-6 July
1982 total lunar eclipse, Appl. Opt., 22, 2682, 1983.

Peterson, A. W., W. Pendelton, J. J. Lin, and T. F. Tuan, Analysis of
simultaneous photometric observation of 6900 A and 7900 A OH bands and
5577 A OI together with radiometric observations, Transl. Amer.
Geophys., 66, 324, 1985.

Pfeffer, R. L., and J. Zarichny, Acoustic-gravity wave propagation in
an atmosphere with two sound channels, Pure Appl. Geophys., 55, 175,
1963.

Pitteway, M. L. Y., and C. O. Hines, The reflection and ducting of
atmospheric acoustic-gravity waves, Can. J. Phys., 43, 2222, 1965.

Press, F., and D. G. Harkrider, Propagation of acoustic-gravity waves
in the atmosphere, J. Geophys. Res., 67, 3889-3908, 1962.

Reddy, C. A., Ducting of internal gravity waves in a temperature- and
wind-stratified atmosphere, Internal Gravity and Acoustic Waves, A

Colloquium, Tech. Notes TN-43, 229-256, NCAR, Boulder, Colo, 1969.

Richmond, A. D., The nature of gravity wave ducting in the thermosphere,
J. Geophys. Res., 83, 1385-1389, 1978.

Roble, R. G., R. E. Dickinson, and E. C. Ridley, Seasonal and solar cycle
variations of the zonal mean circulation in the thermosphere, J.
Geophys. Res., 82, 5493-5504, 1977.

Schoeberl, M. R., D. F. Strobel, and J. P. Apruzese, A numerical model of
gravity wave breaking and stress in the mesosphere, J. Geophys. Res.,
88, 5249, 1983.

Silverman, S. M., Unusual fluctuations of 5577 A OI airglow emission
intensity on October 28/29, 1961, Nature, 195, 481, 1962.

Smith, S. A., and D. C. Fritts, Estimation of gravity wave motions,
momentum fluxes and induced mean flow acceleration in the winter
mesosphere over Poker Flat, Alaska, Proc. 21st Conf. Radar Meteorol.,
Edmonton, Canada, 104-110, 1983.

Thorne, G. D., Long-period waves generated in the polar ionosphere
during the onset of magnetic storms, J. Geophys. Res., 73, 6319, 1968.

Tolstoy, I., Wave Propagation, McGraw-Hill, Inc., New York, 1973.

- Tuan, T. F., R. Hedinger, S. M. Silverman, and M. Okada, On gravity wave induced Brunt-Vaisalla oscillations, J. Geophys. Res., 84, 393, 1979.
- Vincent, R. A., and I. M. Reid, HF Doppler measurement of mesospheric gravity wave momentum fluxes, J. Atmos. Sci., 40, 1321, 1983.
- Wang, D. Y., and T. F. Tuan, Propagation of short period gravity waves, Trans. Amer. Geophys., 66, 997, 1985.
- Wang, D. Y., and T. F. Tuan, Effects of dissipation and instability on guided short period gravity waves, Trans. Amer. Geophys., 67, 319, 1986.
- Wang, D. Y., and T. F. Tuan, Effects of the variation of Brunt period with height on gravity waves, Abstract, 3, 789, IUGG Meeting, Vancouver, Canada, 1987.
- Weinberg, J. L., H. M. Mann, N. Y. Misconi, D. E. Beeson, A pictorial atlas of low latitude 5577A and 6300A airglow line emissions, Dudley Observatory Reports, Rept. No. 5, July, 1973.
- Yu, L., T. F. Tuan, and H. Tai, On 'potential' well treatment for atmospheric gravity waves, J. Geophys. Res., 85, 1297-1305, 1980.

FIGURE CAPTIONS

FIGURE

1. Brunt period curve for the COSPAR atmosphere
2. Coordinate system in the horizontal plane
3. Dispersion curves in the COSPAR model
4. The windless modes at $T = 6$ min
 - a Wave Functions
 - b Kinetic Energy Densities
5. Wind Profiles
 - a Zonal Components
 - b Meridional ComponentsThin line for mean circulation
Bold line for mean plus tidal components
6. The windy modes at $T = 6$ min, and $\alpha = 0^\circ$
 - a Wave Functions
 - b Kinetic Energy Densities
7. The windy modes at $T = 6$ min, and $\alpha = 90^\circ$
 - a Wave Functions

- b Kinetic Energy Densities
- 8. Dispersion curves in the zonal wind
 - a $\alpha = 0^\circ$ (wave propagation towards the East)
 - b $\alpha = 180^\circ$ (wave propagation towards the West)
- 9. Dispersion curves in the meridional wind
 - a $\alpha = 90^\circ$ (wave propagation towards the North)
 - b $\alpha = 270^\circ$ (wave propagation towards the South)
- 10. Directional variation of V_{phx} in the winds
 - a for $T = 6$ min
 - b for $T = 14$ min
- 11. The three terms and the Richardson's numbers
 - Windless mode, $T = 5.5$ min, $V_{phx} = 72$ m/sec
 - a Inertial, viscous, nonlinear terms
 - Δ Inertial term
 - + Nonlinear term
 - * Viscous term
 - b Richardson's numbers

Bold line gives the wave function in arbitrary scale

Relative variation of density at 100 km is 20%

12. The three terms and the Richardson's numbers

Windy mode, $T = 5.5$ min, $V_{phx} = 260$ m/sec, $\alpha = 0^\circ$

-a Inertial, viscous, nonlinear terms

Δ Inertial term

+ Nonlinear term

* Viscous term

-b Richardson's numbers

13. The three terms and the Richardson's numbers

Windy mode, $T = 12$ min, $V_{phx} = 210$ m/sec, $\alpha = 180^\circ$

-a Inertial, viscous, nonlinear terms

Δ Inertial term

+ Nonlinear term

* Viscous term

-b Richardson's numbers

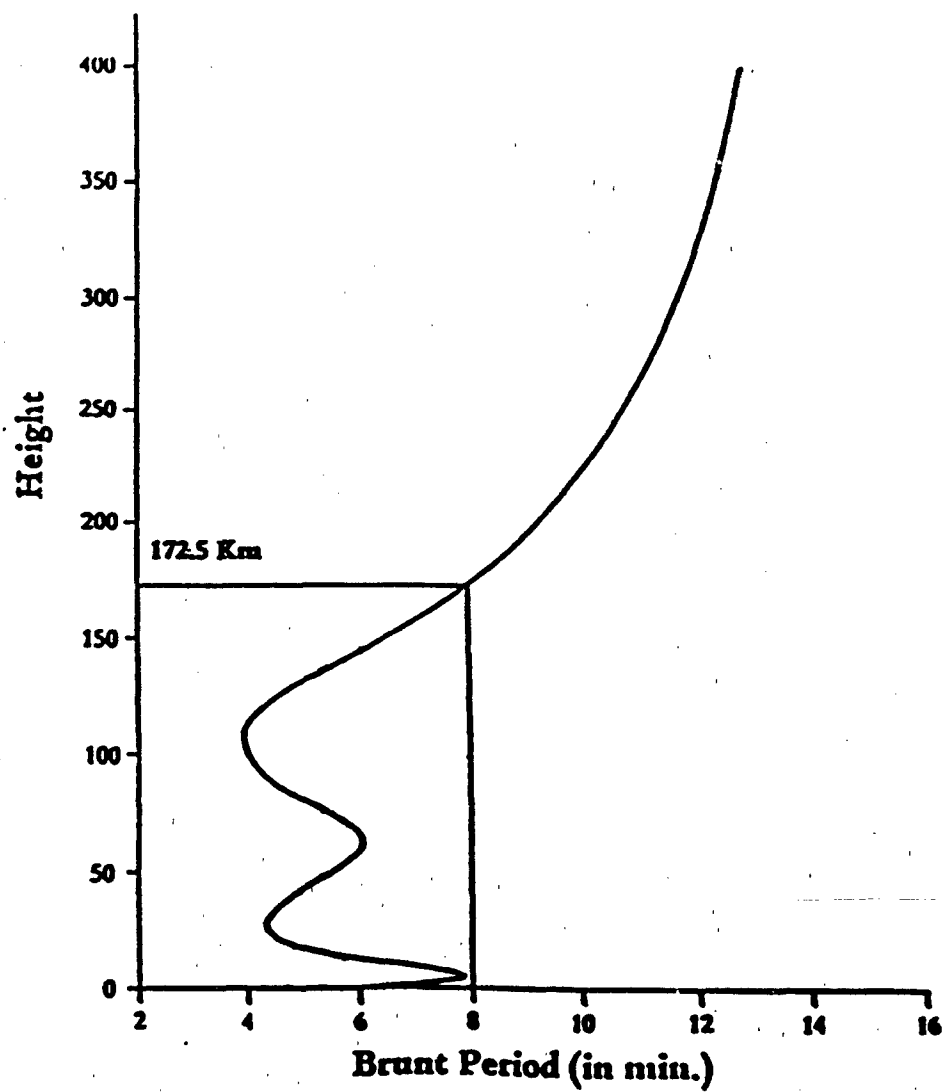


Figure 1. Brunt period curve for the COSPAR atmosphere

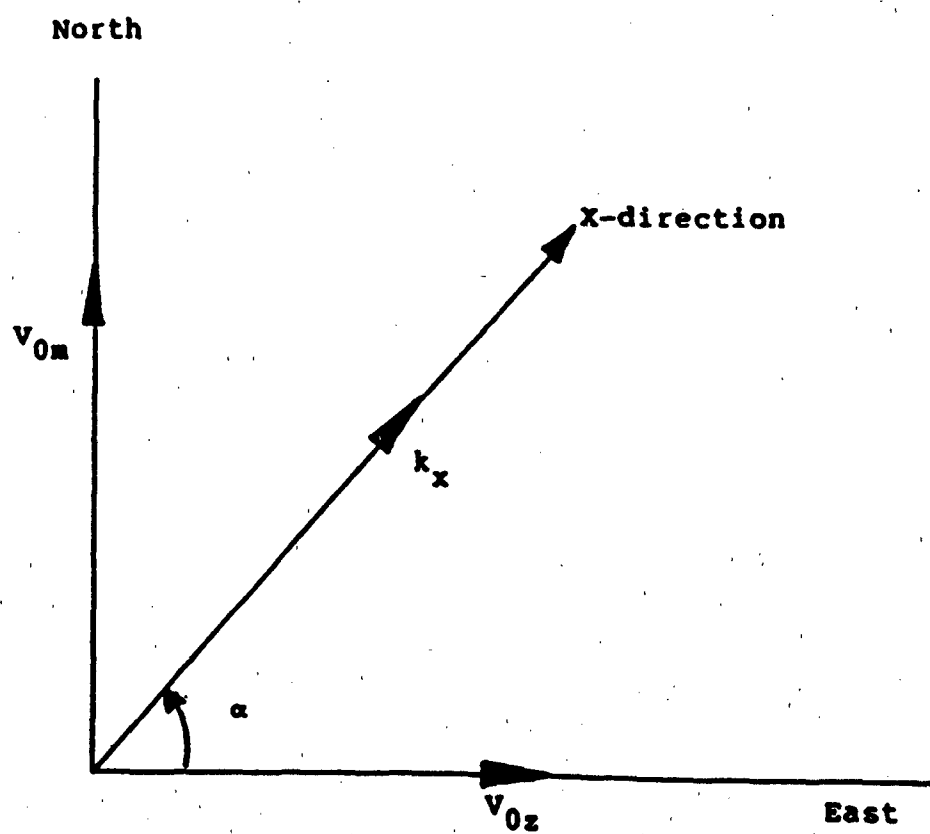


Figure 2. Coordinate system in the horizontal plane

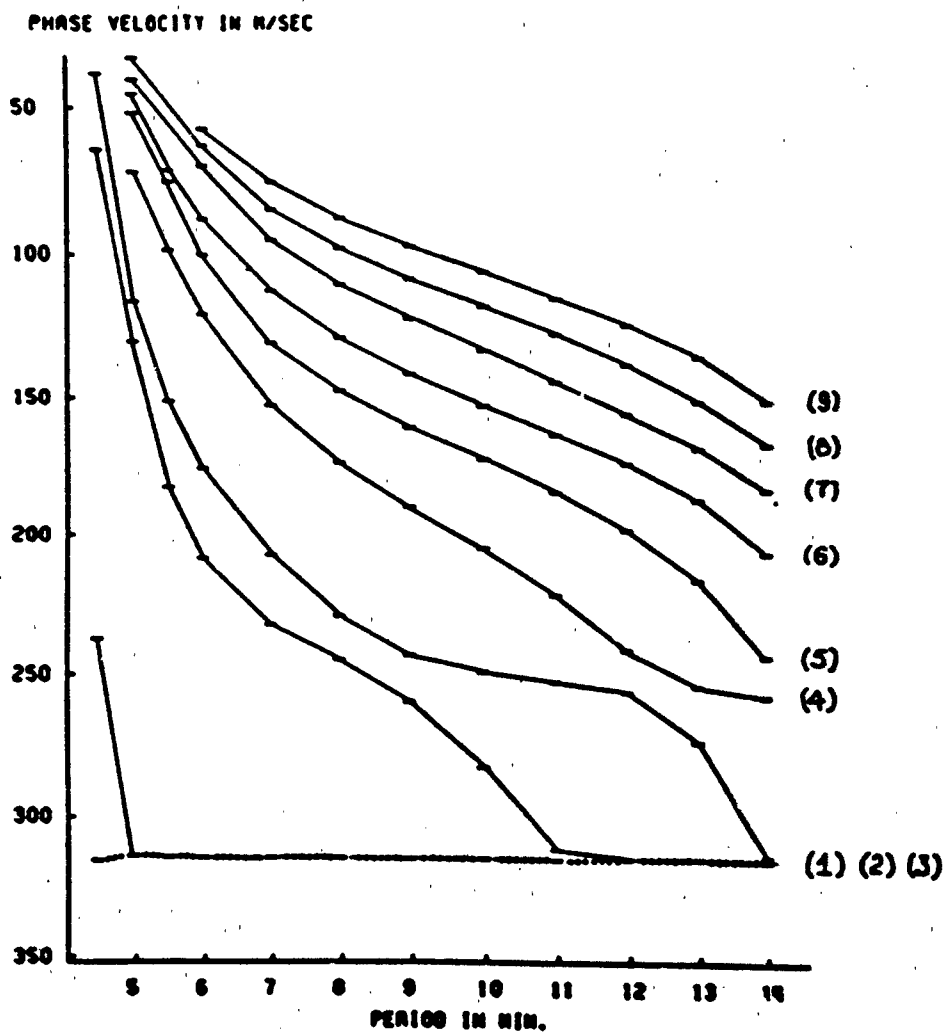


Figure 3. Dispersion curves in the COSPAR model

The Windless modes at T = 6 min

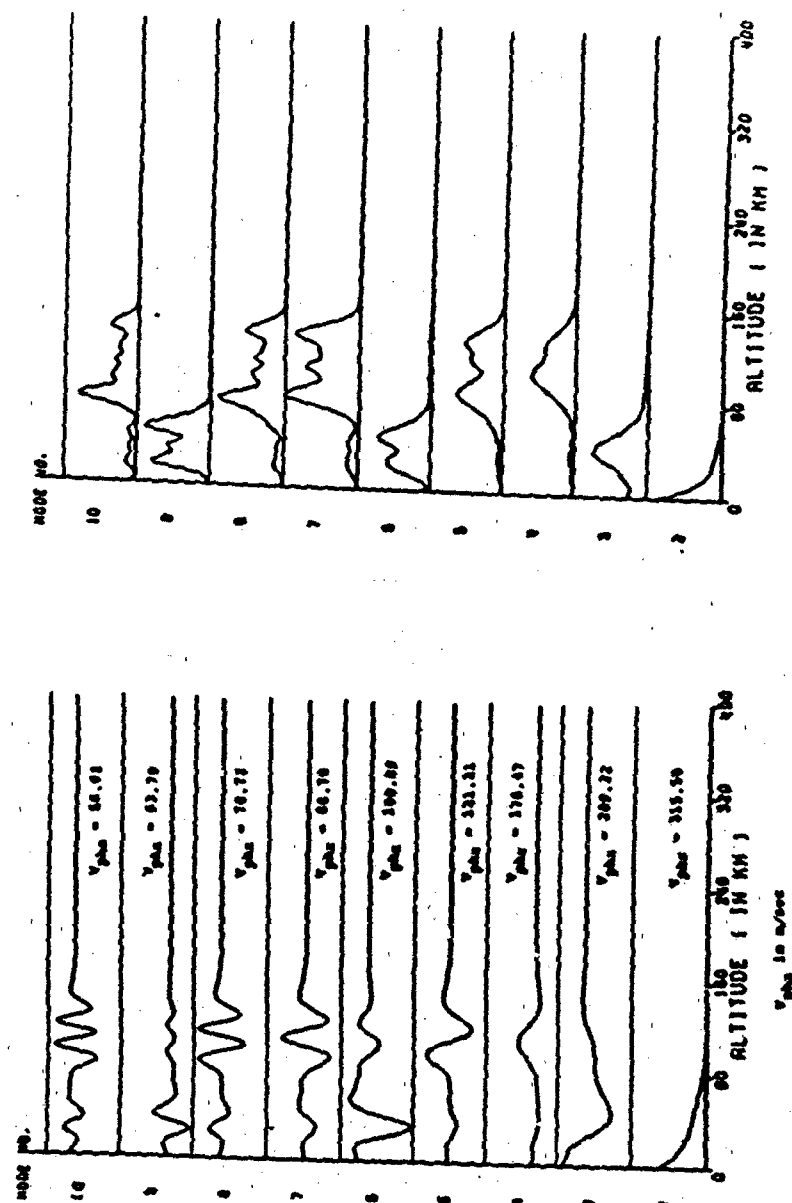


Figure 4-a. Wave Functions

Figure 4-b. Kinetic Energy Densities

Wind Profiles

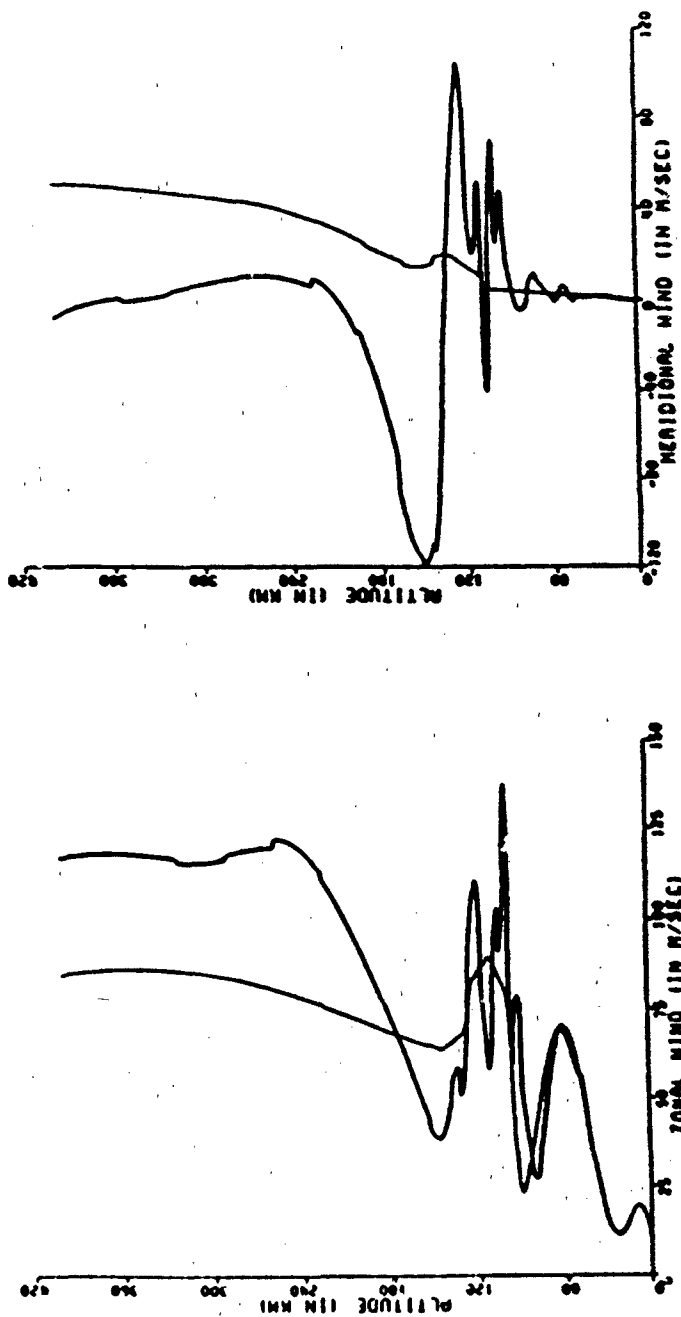


Figure 5-a. Zonal Components

Thin line for mean circulation
 Bold line for mean plus tidal components

Figure 5-b. Meridional Components

The windy modes at $T = 6$ min, and $\phi = 0^\circ$

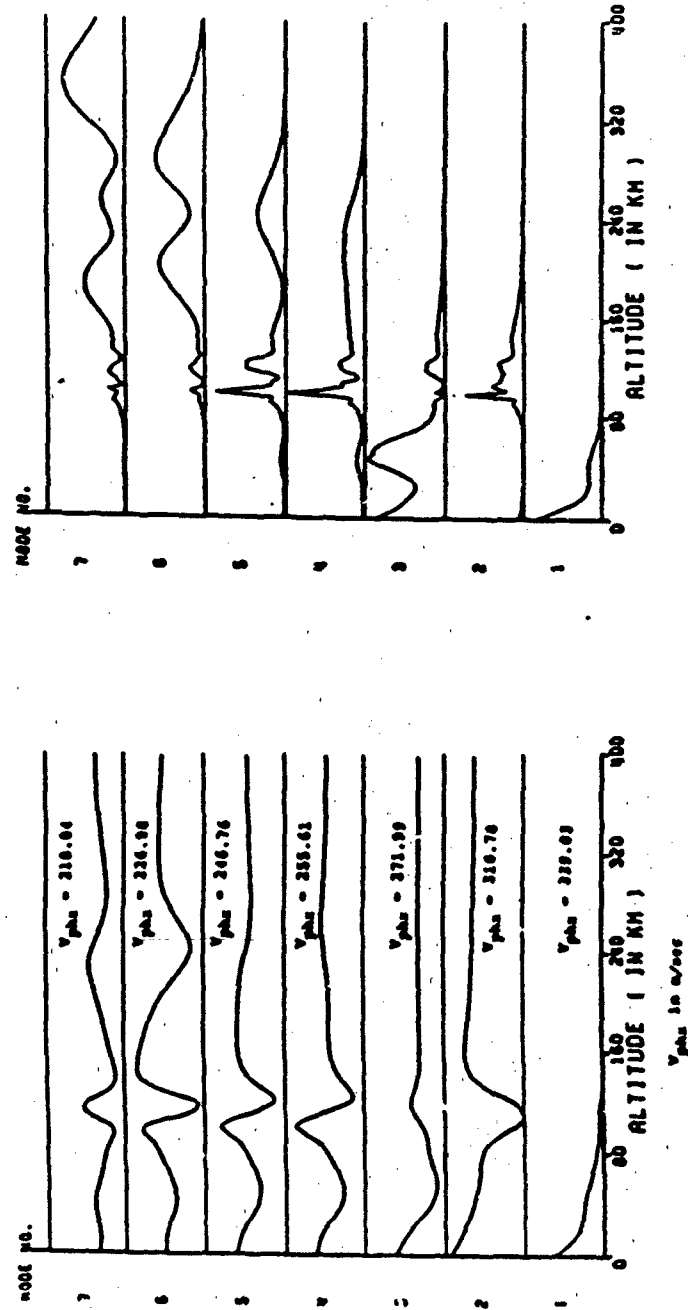


Figure 6-a. Wave Functions

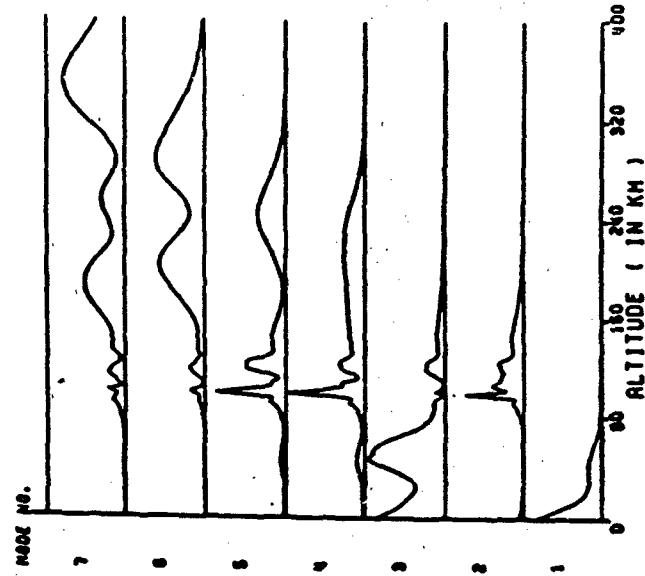


Figure 6-b. Kinetic Energy Densities

The windy modes at $T = 6$ min, and $\theta = 90^\circ$

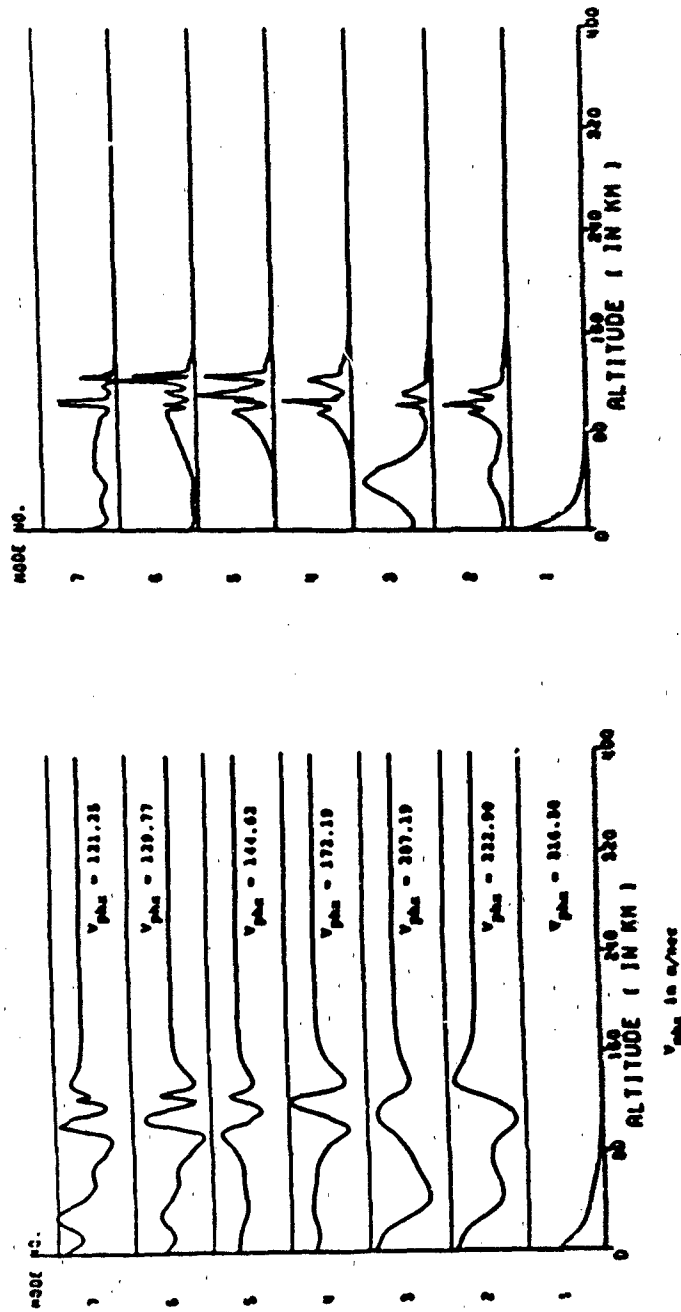


Figure 7-a. Wave Functions

Figure 7-b. Kinetic Energy Densities

Dispersion curves in the zonal wind

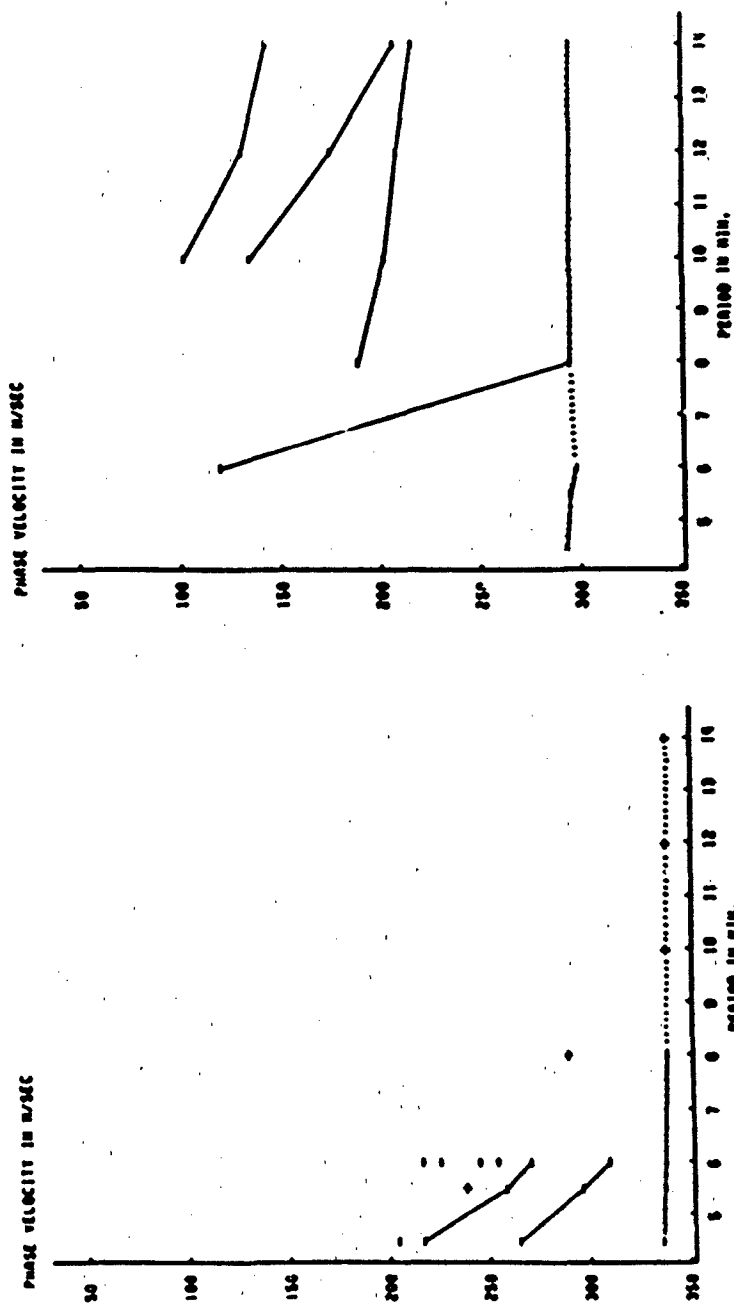


Figure 8-a. $\alpha = 0^\circ$ (wave propagation towards the East)

Figure 8-b. $\alpha = 180^\circ$ (wave propagation towards the West)

Dispersion curves in the meridional wind

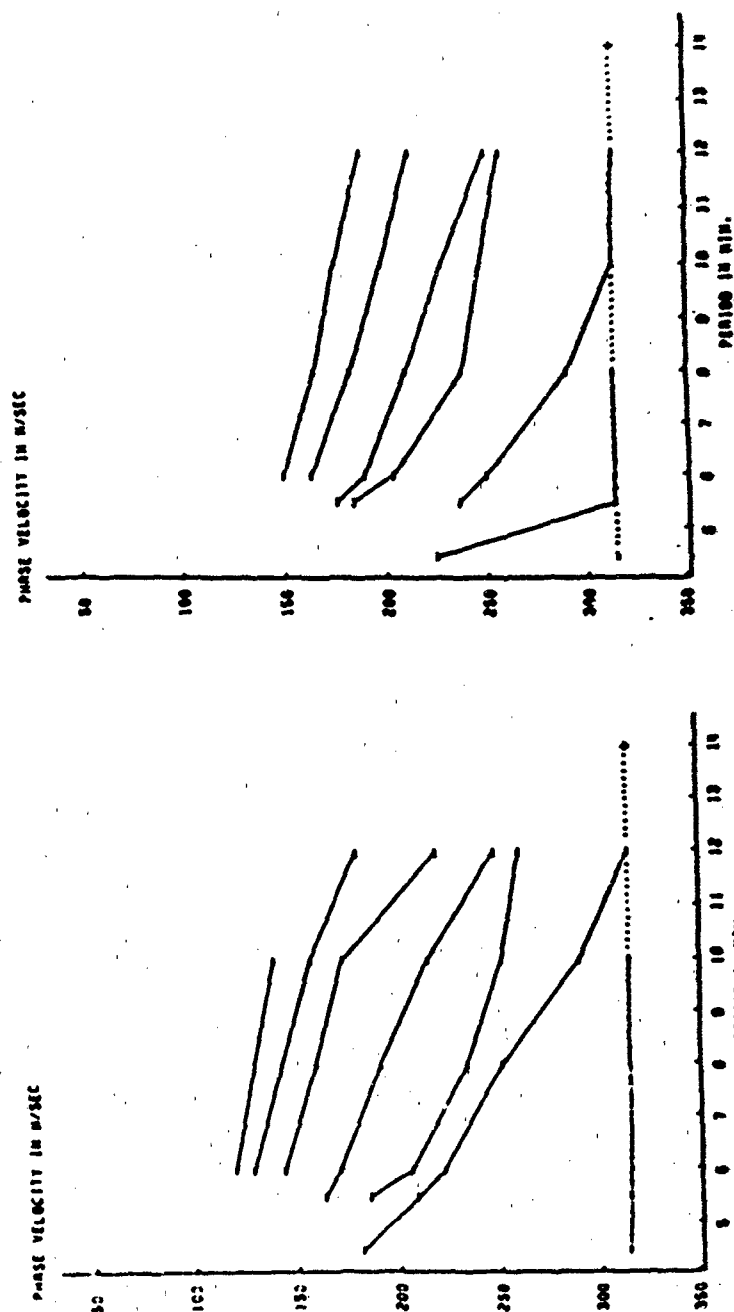


Figure 9-a. $\alpha = 90^\circ$ (wave propagation towards the North)

Figure 9-b. $\alpha = 270^\circ$ (wave propagation towards the South)

Directional variation of V_{phx} in the winds

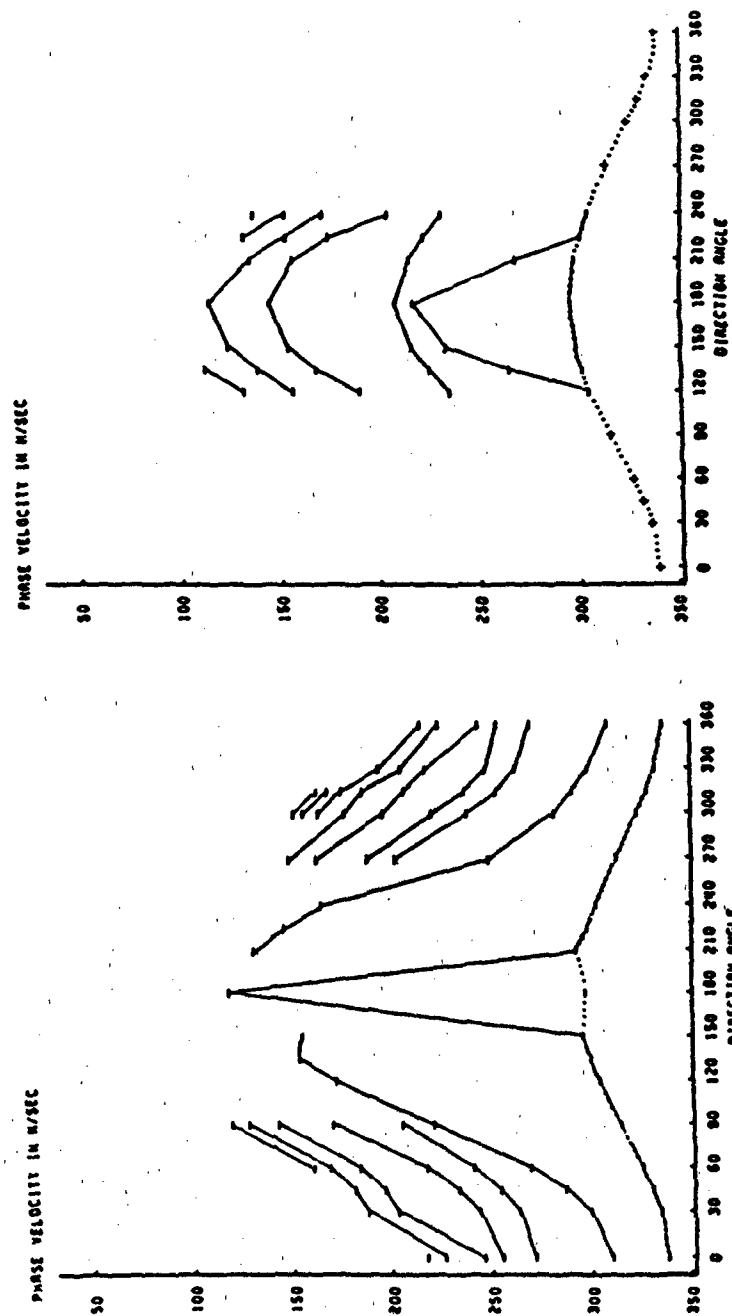


Figure 10-b. for $T = 14$ min.

Figure 10-a. for $T = 6$ min

The three terms and the Richardson's numbers
 Windless mode, $T = 5.5$ min, $V_{phx} = 72$ m/sec

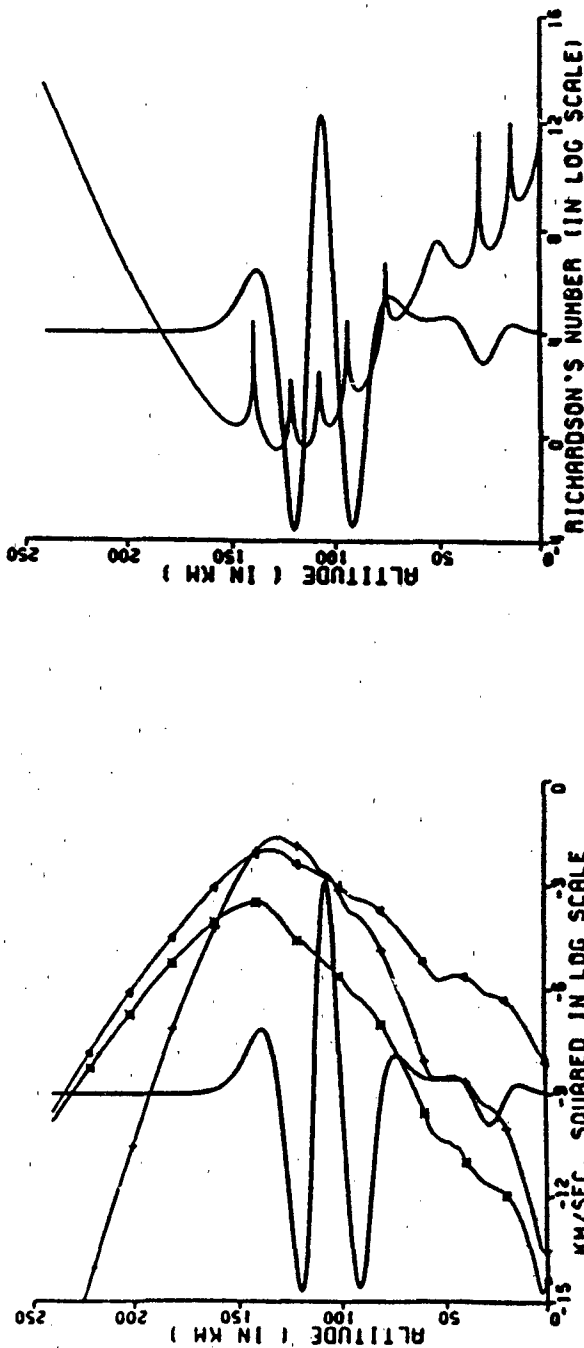


Figure 11-a. Inertial, viscous, nonlinear terms

Δ Inertial term
 $+$ Nonlinear term
 $*$ Viscous term

Bold line gives the wave function in arbitrary scale
 Relative variation of density at 100 km is 20%

The three terms and the Richardson's numbers
 Windy mode, $T = 5.5$ min., $V_{phx} = 260$ m/sec, $\approx 0^\circ$

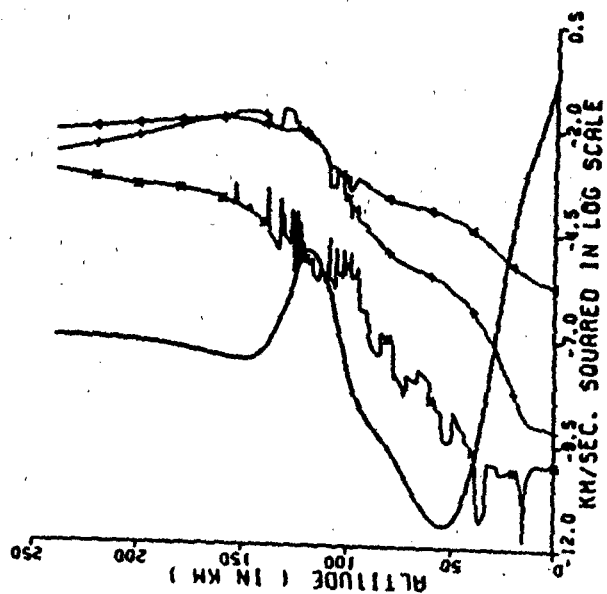


Figure 12-a. Inertial, viscous, nonlinear terms
 Δ Inertial term
 $*$ Nonlinear term
 $*$ Viscous term

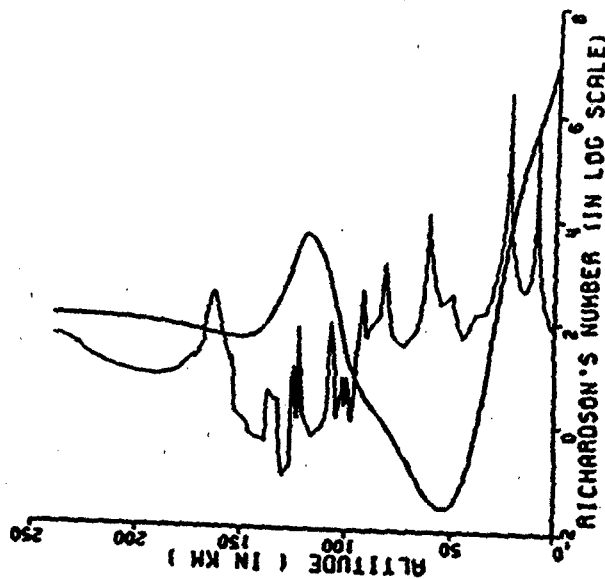


Figure 12-b. Richardson's numbers

The three terms and the Richardson's numbers
Windy mode, $T = 12$ min, $V_{phx} \approx 210$ m/sec, $\theta = 180^\circ$

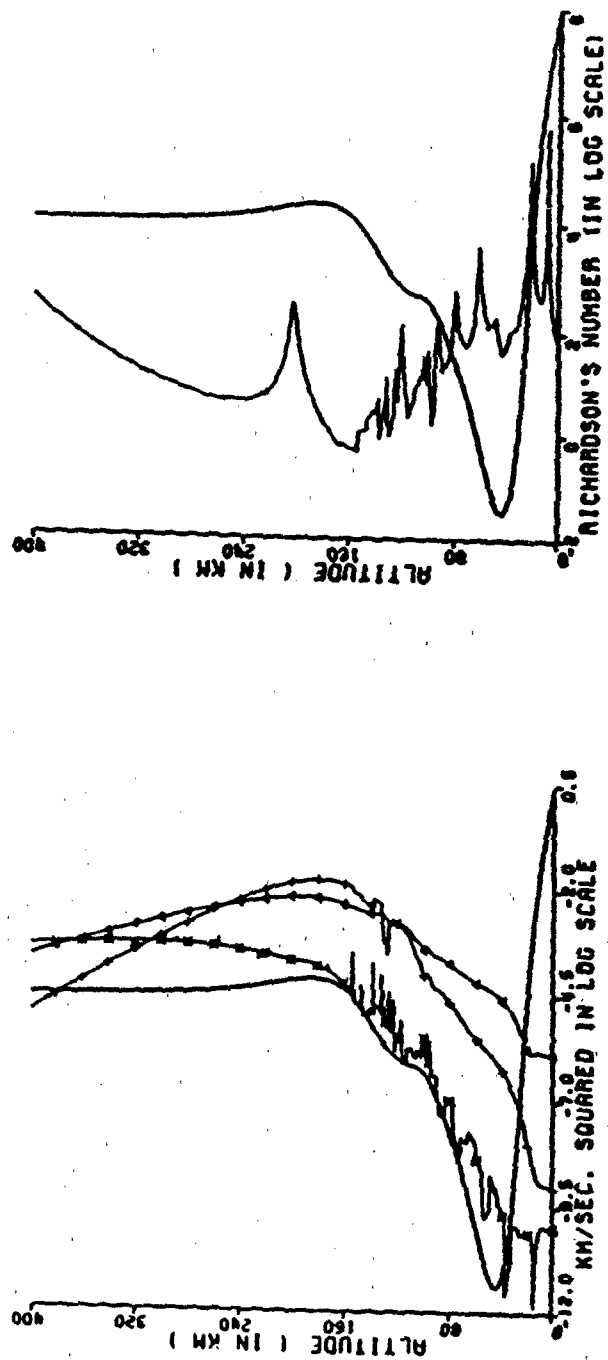


Figure 13-a. Inertial, viscous, nonlinear terms
+ Inertial term
+ Nonlinear term
* Viscous term

Figure 13-b. Richardson's numbers

PART B:

**ON THE IMPORTANCE OF THE PURELY GRAVITATIONALLY INDUCED
DENSITY, PRESSURE AND TEMPERATURE VARIATIONS IN GRAVITY
WAVES; THEIR APPLICATION TO AIRGLOW OBSERVATIONS.**

U. Makhlouf[#], E. Dewan^{*}, J. Isler[#] and T. F. Tuan[#]

[#]Physics Department

University of Cincinnati

Cincinnati, Ohio 45221

^{*}Optical Physics Division

Air Force Geophysics Laboratory

Hanscom AFB

Bedford, Massachusetts 01731

Abstract

A quantitative study is made on the relative importance of the purely gravitationally induced compression (G.I.C.) due to fluid particle altitude change and the actual "wave compression" which can occur at a fixed altitude in a gravity wave. The results for density, pressure and temperature variations show the following: (1) the G.I.C. effects predominate (>95%) for $v/c < 20\%$ where v is the horizontal phase velocity and very simple formulas can be obtained; (2) the relative importance depends strongly on frequency for wave periods less than 10 min., but becomes totally independent of frequency for periods greater than 20 min.; (3) the temperature measurements can be quickly converted to height variations wherever the G.I.C. effect predominates; in general the conversion is equivalent to the adiabatic lapse rate, i.e. a 10° temperature variation corresponds to a height change of 1 km.

In addition, the total kinetic energy density can be simply expressed in terms of height variation and, whenever the G.I.C. effects predominate, can be very easily obtained from temperature measurements. An interesting by-product has been that for waves of small horizontal phase speed, the total wave kinetic energy at any frequency is equal to the kinetic energy of the natural (Brunt) oscillation of an air parcel with the same vertical displacement.

On Gravitational and Acoustic Effects in Gravity Waves

(I) Introduction

The purpose of the present note is to determine the degree to which Gravity Waves (to be abbreviated G.W.) are subject to purely Gravitationally Induced expansions and compressions (G.I.C.) from altitude changes of a given parcel of air and the degree to which they are caused by purely "wave compression". If, for certain types of G.W., the G.I.C. effects can cause most (say 90%) of the G.W. variations so that we can neglect "wave compression", then the resulting simplification (Dewan et al (1988)) can allow us to use very simple formulas for the G.W. parameters, (density, pressure and temperature fluctuations) as well as to make quick estimates of other different G.W. parameters. For instance, a quick conversion from temperature fluctuations to height fluctuations can be readily affected and the latter can be used for a quick estimate of the kinetic energy density. This is also very useful in airglow measurements where interferometer measurements give temperature directly and hence airglow height changes can be estimated. While some of our results are known qualitatively to G. W. specialists, to our knowledge there has never been a systematic quantitative treatment of the subject.

We will begin by showing that the density, pressure and temperature fluctuations can be explicitly expressed as a sum of two terms; one describing the G.I.C. compression, while the other the "wave motion". The former vanishes in the absence of gravity ($g=0$) while the latter remains in

altered form and provides for purely longitudinal acoustic "wave compression".

For $g \neq 0$, the relative importance of these two effects depends on the magnitude of the horizontal phase velocity of the G.W. as compared to the speed of sound. For small scale G.W., where by definition we mean the phase velocity is much less than the speed of sound and the wavelength is also small, we have found that indeed the G.I.C. effects predominate. Since much of the observed mid-latitude airglow fluctuations (including OH) involve relatively small-scale G.W. (Witt (1962), Clairemidi et al (1985), Taylor & Hapgood (1988) with low horizontal phase velocity $v < 70 \text{ m sec}^{-1}$, we may, for most cases, assume that the density, pressure and temperature variations are G.I.C. and a quick conversion to height variations may be made. Very simple formulas for the kinetic energy density can be derived, where $k_z^2 > 0$, both for the general case and even more so in the G.I.C. approximation.

We should point out that there is considerable interference between the two effects and that only if either is greater in magnitude than the other by a large factor can we comfortably neglect the smaller terms. To test the limits of this criterion we will consider three specific experimental observations; the first being the airglow observation made by Taylor and Hapgood (1988) (in association with the MAPSTAR program) which easily meets our criterion; the second being the wave observations by Clairemidi et al (1985) which also meets our criterion; the third being observations on noctilucent clouds made by Witt (1962) and is marginally above the limits of our criterion. The results show that for all three

sets of observations, the simple G.I.C. model is surprisingly accurate and that one may safely assume that much of mid-altitude density, pressure and temperature fluctuations is governed by G.I.C.s. In general, we have proved that in the region $v \ll c$ where the G.I.C. expansion or contraction effects dominate, a 10°K variation in temperature would indicate an altitude change of 1 km of a parcel of air. We have also found that in the same region the kinetic energy density is equivalent to that of the free vertical oscillation of an air parcel with the same vertical displaced amplitude and is independent of the wave frequency. Thus, the above conversion can be immediately used to calculate the kinetic energy density.

II. G.I.C. Expansion & Contraction

When a fluid element is displaced by a vertical distance, h , in a hydrostatic fluid, its density is compressed by an amount $\Delta\rho_a$. This density change, $\Delta\rho_a$, is produced by a change in background pressure, Δp , (where $\Delta p = (\partial p / \partial z) h = c^2 \Delta\rho_s$ and $\Delta\rho_s$ is the density variation due purely to adiabatic compression) minus the change in background density, $\Delta\rho_o = (\partial\rho_o / \partial z)h$. One can show that in an uniform isothermal background atmosphere with scale height H ,

$$\begin{aligned} \frac{\Delta\rho_a}{\rho_o} &= \frac{\Delta\rho_s}{\rho_o} - \frac{\Delta\rho_o}{\rho_o} \\ &= \left(\frac{\gamma - 1}{\gamma} \right) \frac{h}{H} \end{aligned} \quad (1)$$

where we have used the fact that $c^2 \rho_0 = \gamma p_0$

and

$$\frac{1}{\rho_0} \frac{\partial \rho_0}{\partial z} = -H^{-1} = \frac{1}{p_0} \frac{\partial p_0}{\partial z}$$

III. A comparison of the G.I.C. and wave compression

In a G.W. with frequency ω , $h = w/\omega$ (to first order) where h and w are the vertical displacement and velocity fields respectively. At the Brunt frequency, $\omega = \omega_b$, the atmosphere would just oscillate vertically at its natural frequency with the density fluctuations given by (1). In general, by using the Hines' (1960) formula for $\Delta \rho / \rho_0$, $h = w/\omega$ and horizontal velocity field u we can show that to the first order (see Appendix (I)):

$$\begin{aligned} \frac{\Delta \rho}{\rho_0} &= \left(\frac{\gamma - 1}{\gamma} \right) \frac{h}{H} + \left(\frac{v}{c} \right)^2 \left(\frac{u}{v} \right) \\ &= \frac{\Delta \rho_a}{\rho_0} + \frac{\Delta \rho_c}{\rho_0} \end{aligned} \quad (2)$$

where u = horizontal particle velocity

$v = v_x$ = horizontal phase velocity

$\Delta \rho_c / \rho_0 = (v/c)^2 (u/v)$ = density fluctuation due to wave compression

From (2) it is clear that $\Delta\rho_a/\rho_0 \rightarrow 0$ as $g \rightarrow 0$ since $H = c^2/\gamma g$, and the terms $\Delta\rho_c/\rho_0$ will be appropriately changed to provide for the purely longitudinal "wave compression" at all frequencies for sound wave propagation in the absence of gravity. As $g \rightarrow 0$, $H \rightarrow \infty$ and using (A22) we obtain

$$\frac{|\Delta\rho|}{\rho_0} \xrightarrow{g \rightarrow 0} \frac{|\Delta\rho_c|}{\rho_0} = \frac{|uv|}{c^2} = \frac{(|u|^2 + |w|^2)^{1/2}}{c} \quad (2a)$$

and

$$\frac{|u|}{|w|} \xrightarrow{g \rightarrow 0} \frac{k_x}{k_z}$$

where k_x is the horizontal wave vector. (2a) clearly shows a purely longitudinal wave compression when $g = 0$. From now on we shall only be concerned with $g=0$. In that case, from (2) the relative importance of $\Delta\rho_a/\rho_0$ and $\Delta\rho_c/\rho_0$ depends on (v/c) and, in order to remain well below the Lindzen (1981) limit for G.W. saturation, $|u| < v$ (see Fritts, 1984). Clearly for small-scale G.W. where $v \ll c$, the density variation comes mainly from G.I.C. compression, $\Delta\rho_a/\rho_0$. On the other hand for $v \rightarrow c$ and close to the limit for G. W. saturation the wave compression $\Delta\rho_c/\rho_0$ is large and we need to include both effects.

In general, since both $\Delta\rho_a/\rho_0$ and $\Delta\rho_c/\rho_0$ are complex quantities with different phases, considerable interference occurs between the two terms and only if one has a magnitude of at least 4 to 5 times greater than the other can we neglect the other term.

To make a quantitative comparison between $\Delta\rho_a$ and $\Delta\rho_c$, we plot

$|\Delta\rho_A|/|\Delta\rho|$ and $|\Delta\rho_C|/|\Delta\rho|$ as a function of v/c . It can be shown for $k_z^2 > 0$, (see Appendix II),

$$\frac{|\Delta\rho_A|}{|\Delta\rho|} = \left[\frac{(\gamma-1)(1-(v/c)^2)}{(\gamma-1) - (\omega/\omega_b)^2(v/c)^2} \right]^{1/2} \quad (3)$$

and

$$\frac{|\Delta\rho_C|}{|\Delta\rho|} = \left[\frac{1 - (\omega/\omega_b)^2}{(\gamma-1) - (\omega/\omega_b)^2(v/c)^2} \right]^{1/2} \left(\frac{v}{c} \right) \quad (4)$$

Thus, in general $|\Delta\rho_A|/|\Delta\rho|$ begins with the value unity (i.e. density variations are due entirely to G.I.C. compression) at $v/c = 0$, while $|\Delta\rho_C|/|\Delta\rho|$ begins at zero (i.e. no "wave compression"). As can be seen from (3) and (4), when v/c increases, the behavior of $|\Delta\rho_A|/|\Delta\rho|$ and $|\Delta\rho_C|/|\Delta\rho|$ depend entirely on ω/ω_b for any value of v/c .

For long period gravity waves where $\omega \ll \omega_b$, we may neglect the terms involving ω/ω_b in the denominator for both $|\Delta\rho_A|/|\Delta\rho|$ and $|\Delta\rho_C|/|\Delta\rho|$. For such cases

$$\frac{|\Delta\rho_A|}{|\Delta\rho|} = 1 - \left(\frac{v}{c} \right)^2 \quad (5)$$

and

$$\frac{|\Delta\rho_C|}{|\Delta\rho|} = \left(\frac{1}{\gamma-1} \right)^{1/2} \left(\frac{v}{c} \right) \quad (6)$$

and $|\Delta\rho_A|/|\Delta\rho|$ drops from unity as v/c increases while $|\Delta\rho_C|/|\Delta\rho|$ increases linearly with v/c .

Fig. 1 shows this behavior for gravity waves with periods greater than

20 min. Actually, there is little variation with period from 20 min. on up and a plot at $\tau = 120$ min. falls exactly on top of the corresponding curves at 20 minutes. Both curves are plotted from (3) and (4), but there would have been no difference if we had used (5) and (6). At $\tau = 10$ min., (Fig. 2), $|\Delta\rho_C|/|\Delta\rho|$ begins to deviate from a straight line but only slightly. $|\Delta\rho_A|/|\Delta\rho|$ drops somewhat less as v/c increases showing an increase in importance relative to "wave compression" for a given phase velocity. Furthermore, the cross over between the G.I.C. compression and the "wave compression" remains fairly constant at between $v/c = 55$ to 60% . In general, for G.W. with frequencies in this range (i.e. $\tau > 10$ min.), if we use the approximate criteria that $|\Delta\rho_A|/|\Delta\rho_C|$ has to be greater than a factor of 5, then v/c has to be less than 15% or the horizontal phase velocity has to be less than 45 m sec^{-1} . This covers a fairly large range and include most of the observed mid-altitude small scale G.W. from airglow data.

The vertical green line indicates the position where $k_z^2 = 0$. It is easy to show from the Hines' dispersion formula that $k_z^2 = 0$ corresponds to

$$\frac{v}{c} = \left(\frac{\omega_p^2 - \omega^2}{\omega_g^2 - \omega^2} \right)^{1/2} \quad (7)$$

to the left of the green line $k_z^2 > 0$ and G.W. may propagate freely. To its right $k_z^2 < 0$ and the G.W. is evanescent in the vertical direction, although it still propagates along k_x . The dotted lines represent the evanescent

region. At $v/c = 1$ we have the Lamb mode for which there is no G.I.C. compression since there is no vertical motion and variations in density are caused entirely by "wave compression", an exact reversal of what happens at $v/c = 0$. The same reversal occurs in all the Figures.

As $\tau \rightarrow \tau_D$, the Brunt period, both $|\Delta\rho_A|/|\Delta\rho|$ and $|\Delta\rho_C|/|\Delta\rho|$ increase with v/c , (see Fig. 3 & 4) in such a way that the G.I.C. compression continues to predominate over a much greater range of horizontal phase velocity. In fact, in Fig. 4 where $\tau = 5.2$ min., the G.I.C. compression continues to dominate all the way to the green line where $v/c = 42\%$ corresponding to a horizontal phase velocity of well over 120 m sec.^{-1} ; a strictly medium-scale G.W. (Francis 1975). Thus, as the G.W. period approaches the Brunt period, the G.I.C. compression dominates over a larger range of v and hence a larger range of wavelengths.

The pressure variation can be easily shown to be the same as $\Delta\rho_C$. Using the linearized horizontal momentum conservation equation, it can be shown that for monochromatic waves,

$$\begin{aligned} \Delta p &= \rho_0 u \\ \text{or} \quad \frac{\Delta p}{\rho_0} &= \frac{1}{c^2} \frac{v u}{\tau} \\ \text{so} \quad \frac{|\Delta p|}{c^2 |\Delta\rho|} &= \frac{|\Delta\rho_C|}{|\Delta\rho|} \end{aligned} \quad (8)$$

From Fig. 1-4 we see that there is little pressure variation produced by "wave compression" for small-scale G.W. Only as the scale-size of the

G.W. increases does it become important. Thus, for small-scale G.W. ($<45 \text{ m sec}^{-1}$), the pressure variations are relatively insignificant.

The temperature variations may be very easily obtained from the linearized perfect gas law given by

$$\frac{\Delta T}{T_0} = \frac{\Delta P}{P_0} - \frac{\Delta \rho}{\rho_0} \quad (9)$$

From (7), (9) and (2), we obtain,

$$\frac{\Delta T}{T_0} = (\gamma - 1) \left(\frac{v u}{c^2} \right) - \frac{\Delta \rho_a}{\rho_0} \quad (10)$$

Thus, for $v \ll c$ (small-scale G.W.),

$$\frac{\Delta T}{T_0} = - \frac{\Delta \rho_a}{\rho_0} = - \frac{(\gamma - 1) h}{\gamma H} \quad (11)$$

and the temp. variation is opposite in phase to the G.I.C. density compression. We will define

$$\frac{\Delta T}{T_0} = \frac{\Delta T_a}{T_0} + \frac{\Delta T_c}{T_0} \quad (12)$$

where

$$\frac{\Delta T_a}{T_0} = - \frac{\Delta \rho_a}{\rho_0} ; \quad \frac{\Delta T_c}{T_0} = (\gamma - 1) \frac{v u}{c^2}$$

Again, as in (3) & (4) it is possible to show that for $k_z^2 > 0$, (see Appendix III),

$$\frac{|\Delta T_a|}{|\Delta T|} = \left[\frac{1 - (v/c)^2}{1 - (\gamma - 1) (\omega/\omega_b)^2 (v/c)^2} \right]^{1/2} \quad (13)$$

$$\frac{|\Delta T_c|}{|\Delta T|} = \left[\frac{(\gamma - 1) (1 - (\omega/\omega_b)^2)}{1 - (\gamma - 1) (\omega/\omega_b)^2 (v/c)^2} \right]^{1/2} \left(\frac{v}{c} \right) \quad (14)$$

Thus, once again, for $v/c = 0$ $|\Delta T_a|/|\Delta T| = 1$ and $|\Delta T_c|/|\Delta T| = 0$ and we see

that in the low phase velocity limit (very small-scale G.W.) the temperature variation is caused entirely by the adiabatic expansion and compression of an air parcel oscillating in the vertical direction. For long period G.W. ($\omega \ll \omega_b$), (13) & (14) simplify to;

$$\frac{|\Delta T_a|}{|\Delta T|} = [1 - (\frac{V}{C})^2]^{1/2} \quad (15)$$

$$\frac{|\Delta T_c|}{|\Delta T|} = (\gamma - 1)^{1/2} (\frac{V}{C}) \quad (16)$$

Comparing (15) and (16) with (5) and (6) we see that for long period G.W. $|\Delta T_a|/|\Delta T|$ behaves the same way as $|\Delta \rho_a|/|\Delta \rho|$ in (5) whilst $|\Delta T_c|/|\Delta T|$ has a far more gradual slope than $|\Delta \rho_c|/|\Delta \rho|$. Thus, for temperature variations, the G.I.C. effect predominates over the "wave effect" through a greater range of phase velocities.

All this can be seen from Fig. 5 which shows the behavior of $|\Delta T_a|/|\Delta T|$ and $|\Delta T_c|/|\Delta T|$ for G.W. with periods from 30 min. on up. Again, a plot of both curves at $\tau = 120$ min. can be exactly superimposed over the two curves for $\tau = 30$ min. This is similar to the curve of the density variations (Fig. 1) which has a lower limit at $\tau = 20$ min. Again, for $\tau > 30$ min. there is no significant difference between (13) and (15) or (14) and (16).

Fig. 6, 7 and 8 show the behavior of temperature variations for $\tau = 10, 6.4$ and 5.2 min. respectively. The big difference between these temperature variations and the density variations given by Fig. 2, 3 and 4

is that for the former the effect of G.I.C. compression is even much more important than the "wave compression". For instance, at $r = 6.4$ min., the wave compression effect overtakes the G.I.C. effect at $v/c = 0.72$, whereas the G.I.C. effect remains predominant in the corresponding temperature variation all the way to the green line. For both, however, the G.I.C. effect predominates all the way to the green line when $r = 5.2$ min., approaching the Brunt period.

The dotted curves in all the Figures on the right-hand side of the green line correspond to evanescent waves with $k_z^2 < 0$ and thus a purely imaginary k_z . In this region one can no longer use the relatively simple expressions given by (3), (4), (13) and (14), which were derived for $k_z^2 > 0$ and real k_z . Instead one has to work with the general polarization relations given by Hines (1960).

From the above discussions, it is clear that comparatively small-scale G.W. with horizontal phase velocities less than $40\text{--}50 \text{ m sec}^{-1}$ may be considered to be purely under the influence of G.I.C. expansion and compression (> 90%). This will allow us to make simple conversions from the measurement of temperature fluctuations to height fluctuations. Thus,

$$\frac{|\Delta T|}{T_0} = \frac{|\Delta T_a|}{T_0} = \frac{(\gamma-1)}{\gamma} \frac{|h|}{H} \quad (17)$$

and using the usual values for γ , H and T_0 , we obtain the approximate conversion that a 10° variation in temperature corresponds approximately to a height variation of 1 km. at 90-100 km altitude.

This can be immediately used for computing the time averaged kinetic energy density, K.E., given by

$$\text{K.E.} = 1/4 \rho_0 (|u|^2 + |w|^2) \quad (18)$$

where w = vertical particle velocity. Using the continuity equation and the Hines' dispersion relations one can show that (Appendix IV),

$$\text{K.E.} = \frac{1}{4} \rho_0 \omega_B^2 |h|^2 \left[\frac{1 - (\omega/\omega_B)^2 (v/c)^2}{1 - (v/c)^2} \right] \quad (19)$$

For large-scale G.W. where $v \rightarrow c$, the denominator can be much less than the numerator. This is especially true for long period G.W. Thus, the K.E. can then be much greater than $1/4 \rho_0 \omega_B^2 |h|^2$. For small-scale G.W. ($v \ll c$), on the other hand, the K.E. is very accurately given by:

$$\text{K.E.} = 1/4 \rho_0 \omega_B^2 |h|^2 \quad (20)$$

It is interesting to note that (20) is true irrespective of the frequency of the small-scale G.W. Since (20) is also the K.E. for the natural Brunt oscillation of a parcel of air, we may conclude that the total K.E. of small-scale G.W. at any frequency is equivalent to natural vertical atmospheric oscillations with the same vertical displacement. Here, the G.I.C. approximation for the density, pressure and temperature variations are also good. Using (17), (20) acquires the form

$$\frac{\text{K.E.}}{p_0} = \frac{1}{4} \left(\frac{\gamma}{\gamma-1} \right) \left| \frac{\Delta T_a}{T_0} \right|^2 - \frac{1}{4} \left(\frac{\gamma}{\gamma-1} \right) \left| \frac{\Delta T}{T_0} \right|^2 = 0.875 \left| \frac{\Delta T}{T_0} \right|^2 \quad (20a)$$

where p_0 = background pressure energy. Thus, a measurement of the rotational temperature variation can immediately yield the total kinetic energy density at any frequency for small-scale G.W. In fact, (19) shows that the K.E. depends strongly on frequency only for large-scale G.W. where $v \rightarrow c$.

To summarize: (1) for small-scale G.W. ($v < 45\text{--}50 \text{ m sec}^{-1}$), the K.E. density is the same as that for natural atmospheric oscillations and is independent of wave frequency; (2) for any G.W. (arbitrary v/c), the K.E. again becomes equal to natural atmospheric oscillations when $\omega \rightarrow \omega_D$ as expected; (3) for large-scale G.W. ($v/c \rightarrow 1$), the K.E. for the same vertical displacement become very large and, unlike the two previous cases, can also become very strongly frequency dependent.

(IV) Applications

To specifically apply the above analyses, we apply them to three specific sets of observed data: two sets involve G.W. parameters well within the above mentioned limits for the validity of the purely G.I.C. model; the other with parameters above the borderline. The first set were data taken by Taylor and Hapgood (1988). The observed data include a G.W. with a horizontal phase velocity of $v = 21.7 \text{ m sec}^{-1}$, a horizontal wave

length of $\lambda_x = 26$ km and a period $\tau = 20$ min. Using $g = 9.8 \text{ m sec}^{-2}$ $H = 6.56$ km, $\gamma = 1.4$, $\tau_D = 5.1$ min. (the Brunt period) and the speed of sound $c = 300 \text{ m/sec}^{-1}$, we find that if we employ the full expression given by (10) with help from the Hines' polarization and dispersion relations (Hines 1960) we obtain

$$\frac{|\Delta T|}{T_0} = 4.364 \times 10^{-2} |h| \quad (21)$$

where h is expressed in km. Using the G.I.C. approximation, we obtain

$$\frac{|\Delta T_a|}{T_0} = \frac{(\gamma-1)}{\gamma} \frac{|h|}{H} = 4.355 \times 10^{-2} |h| \quad (22)$$

The error from using (22) is only 0.2%.

The second set were taken by Clairemidi, Hersh and Moreels (Clairavidi et al (1985)). They have measured waves with velocity $v = 15.6 \text{ m sec}^{-1}$ and a period of 48 min. The full temperature fluctuation without approximation is given by

$$\frac{|\Delta T|}{T_0} = 4.36 \times 10^{-2} |h| \quad (23)$$

Compared with the G.I.C. approximation given by (22), we have an error of the order 0.1%.

The third set of data were taken by Witt (1962). The G.W. had $v = 75 \text{ m sec}^{-1}$, $\lambda_x = 50$ km and the rest of the parameters are the same as the first data set. We obtain

$$\frac{|\Delta T|}{T_0} = 4.5 \times 10^{-2} |h| \quad (24)$$

The G.I.C. approximation gives the same result as (22). Thus, the error for this example is 3%. The somewhat bigger error is understandable because at 75 m sec^{-1} the horizontal phase velocity is somewhat above the 45-50 m sec^{-1} upper limit that we mentioned earlier as the safe limit. (i.e. $v/c = 15-20\%$). Actually for this example there is considerable interference between the two terms on the R.H.S. of (10).

(V) Conclusion

The present note seems to show that for small-scale G.W. (say $v/c < 18\%$), the G.I.C. approximation is very good to above 95% in temperature and density fluctuations. The approximation appears to be applicable to much of the observed mid-altitude airglow data. Quick estimates of and simple formulas for G.W. parameters such as height variations and kinetic energy density may be immediately obtained from measurement of temperature variations.

Acknowledgement

We would like to thank Drs. R. Picard and J. Winick for helpful discussions. One of us (T.F. Tuan) would like to thank the National Science Council of the Republic of China for sponsoring his visit to the Atmospheric Physics Department of the National Central University of Chungli, Taiwan, where some of the work was done while the author was on sabbatical leave and where some helpful suggestions were made by several members of the department. The work was sponsored by AFOSR under the MAPSTAR and the Infrared Airglow modelling program. It is partially supported by a research contract with AFGL (AF19628-87K-0026).

Bibliography

- (1) Clairemidi, J., M. Hersh, and G. Moreels, "Bi-dimensional observation of waves near the mesopause at auroral latitudes", Planet. Space Sci., 33, 1013 (1985).
- (2) Dewan, E., T. P. Tuan and U. Makhoul, "On hydrostatic and non-hydrostatic changes of pressure caused by Atmospheric Gravity Waves", Trans. Amer. Geophys. Union, 69, 1342 (1988).
- (3) Francis, S.H., "Global Propagation of Atmospheric Gravity Waves: A Review", J. Atmos. Terr. Phys. 37, 1011-1054 (1975).
- (4) Hines, C. O. "Internal Atmospheric Gravity Waves at Ionospheric Heights", Can. J. Phys., 38, 1441-1481 (1960).
- (5) Taylor, M. J. and M. A. Hapgood, "Identification of a Thunderstorm as a source of short-period Gravity Waves in the Upper Atmospheric Nightglow Emission", Planet Space Sci., 36, 975-985, (1988).
- (6) Vincent, R. A. and I. M. Reid, "HF Doppler Measurements of Mesospheric Gravity Wave Momentum Fluxes", J. Atmos. Sci., 40, 1321-1333 (1983).

- (7) Witt, G., "Height structure and displacements of Noctilucent Clouds", *Tellus*, 14, 1-18 (1962).
- (8) Fritts, D. , "Gravity wave saturation in the middle atmosphere: A review of theory and observation", *Reviews of geophysics and space physics*, 22, 275-308 (1984)

Figure captions

Fig. 1 a plot of the induced density variation due to the gravitational (red) and the acoustic compressions (black) as a function of v/c for wave periods > 20 min.

Fig. 2,3,4 plots of the induced density variation due to the gravitational (red) and the acoustic compressions (black) as a function of v/c for wave periods ≈ 10 , 6.4 , 5.2 min. respectively.

Fig. 5 a plot of the induced temperature variation due to the gravitational (red) and the acoustic compressions (black) as a function of v/c for wave periods > 30 min.

Fig. 6,7,8 plots of the induced temperature variation due to the gravitational (red) and the acoustic compressions (black) as a function of v/c for wave periods ≈ 10 , 6.4 , 5.2 min. respectively.

Fig. 9 a plot of the ratio of the kinetic energy density to the background pressure as a function of v/c for wave periods of 20 , 10 , 6.4 & 5.2 min.

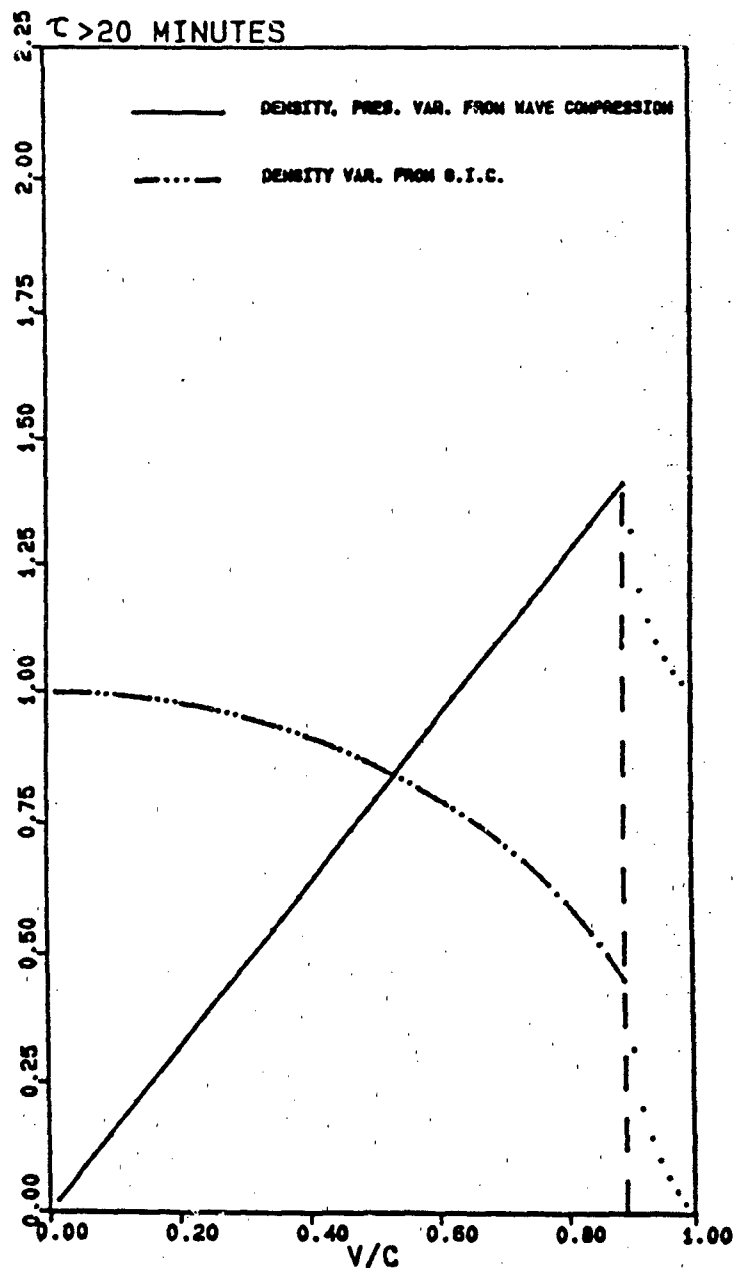
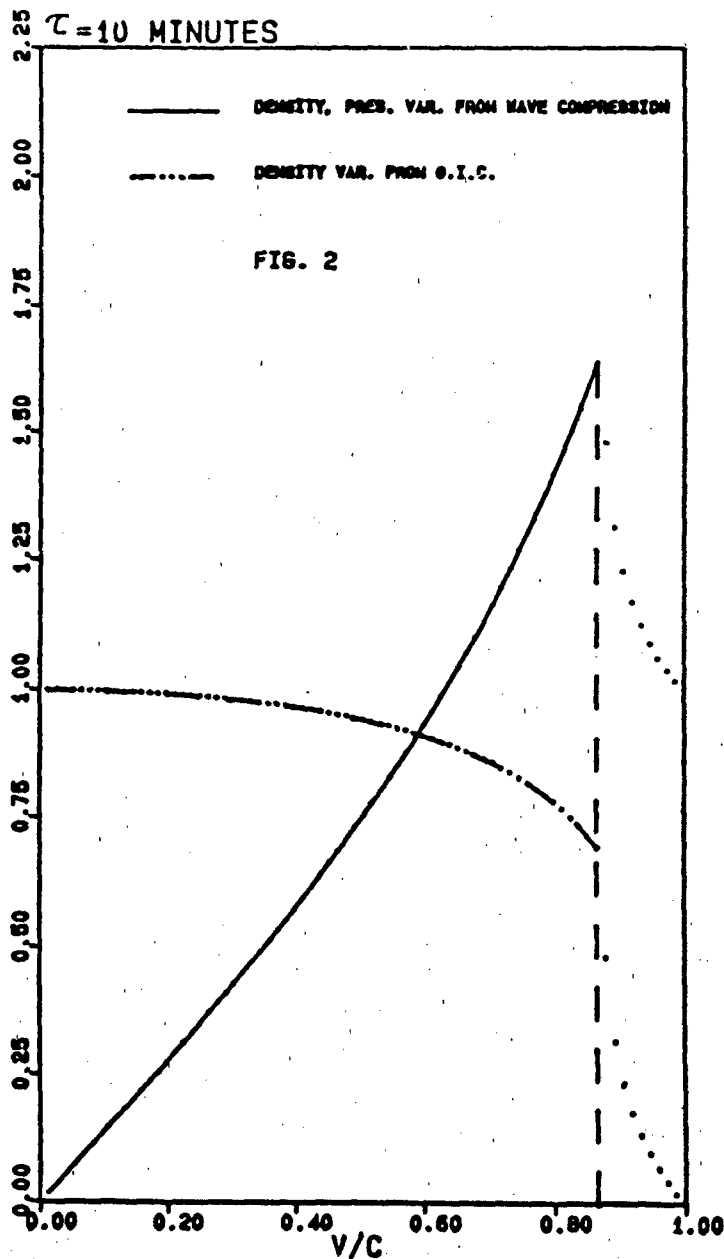
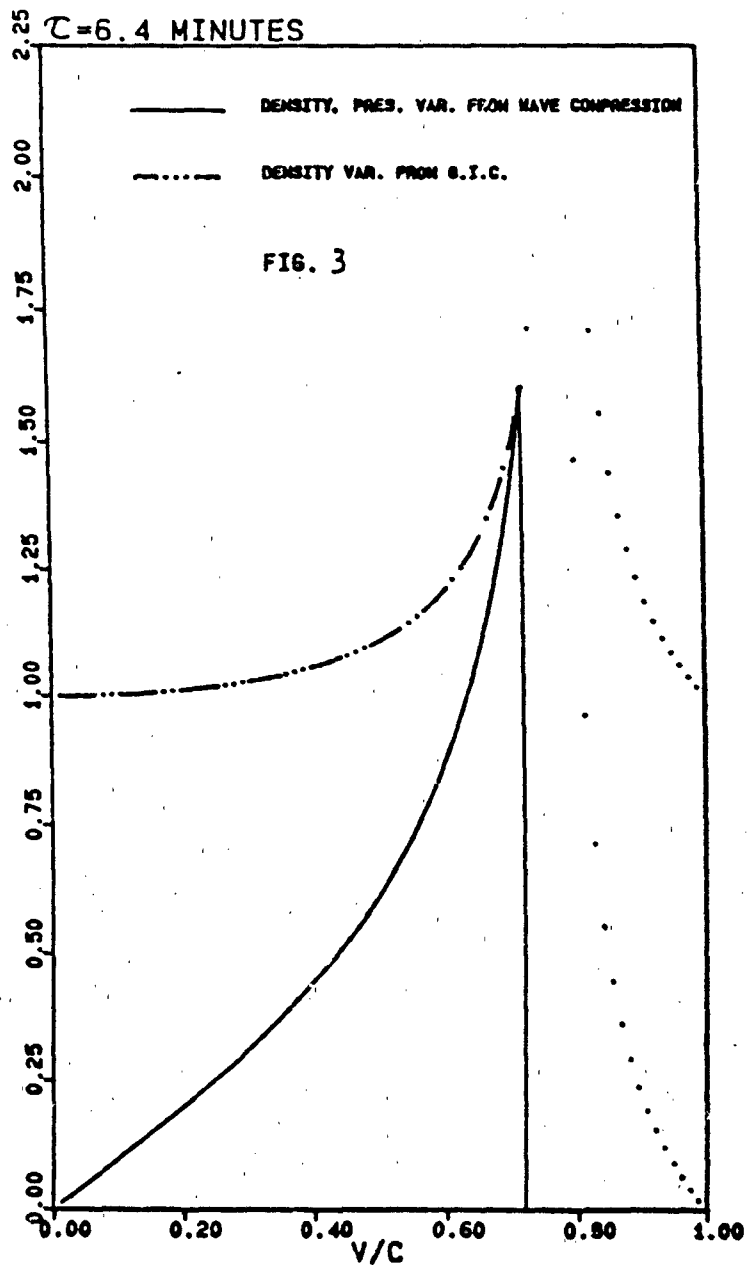


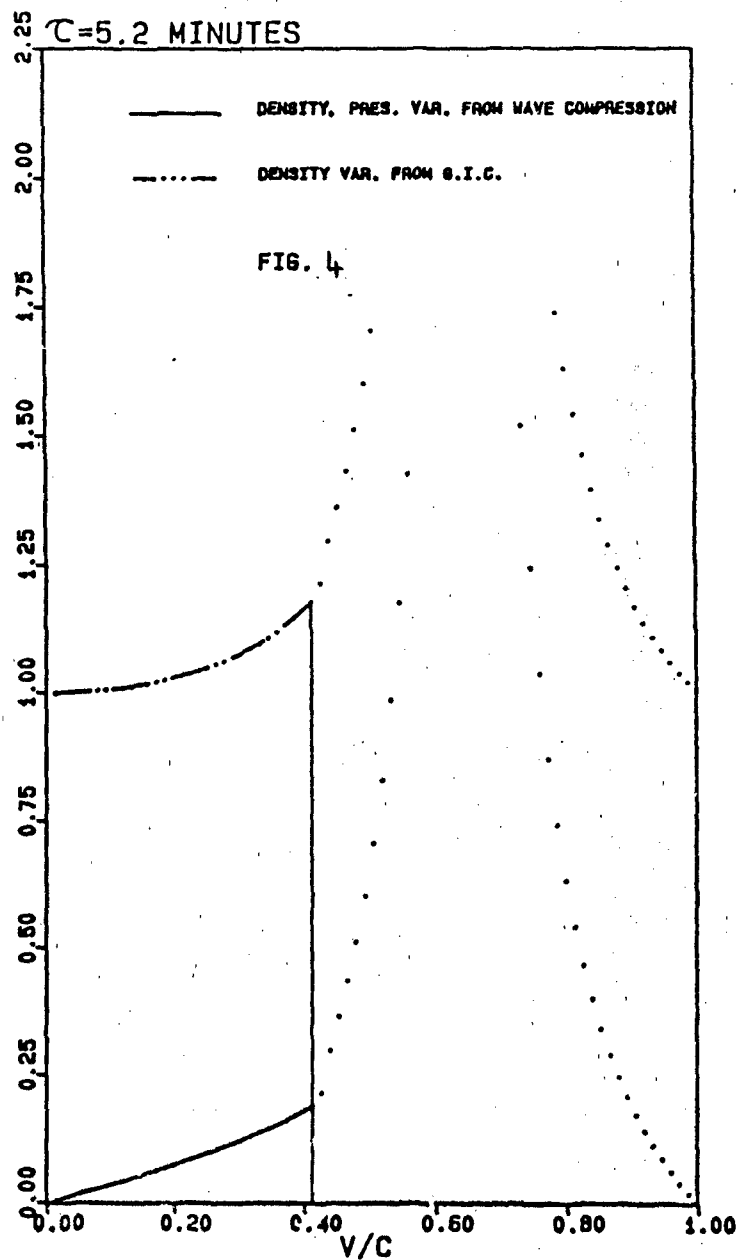
Figure 1 - a plot of the induced variation due to the gravitational (red) and the acoustic compressions (black) as a function of v/c for wave periods 20 min.



Figures 2, 3, 4 - plots of the induced density variation due to the gravitational (red) and the acoustic compressions (black) as a function of v/c for wave periods = 10, 6.4, 5.2 min. respectively.



Figures 2, 3, 4 - plots of the induced density variation due to the gravitational (red) and the acoustic compressions (black) as a function of v/c for wave periods = 10, 6.4, 5.2 min. respectively.



Figures 2, 3, 4 - plots of the induced density variation due to the gravitational (red) and the acoustic compressions (black) as a function of v/c for wave periods = 10, 6.4, 5.2 min respectively.

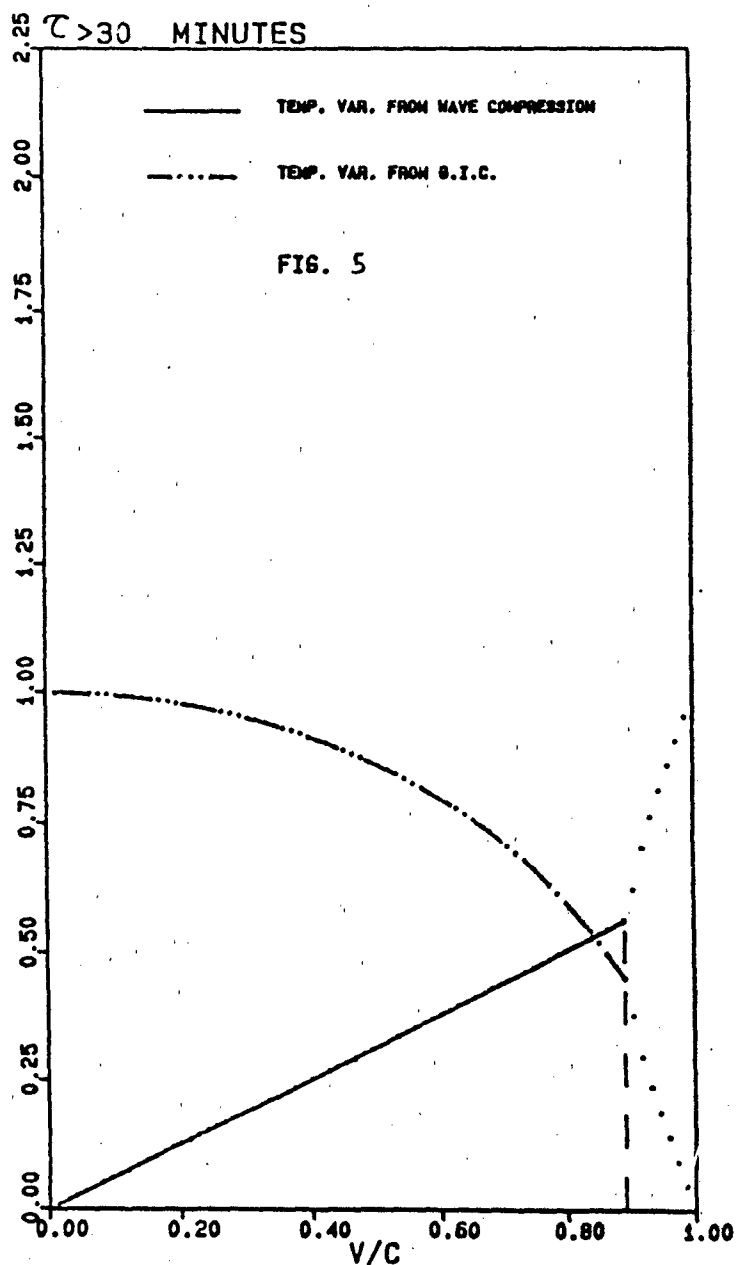
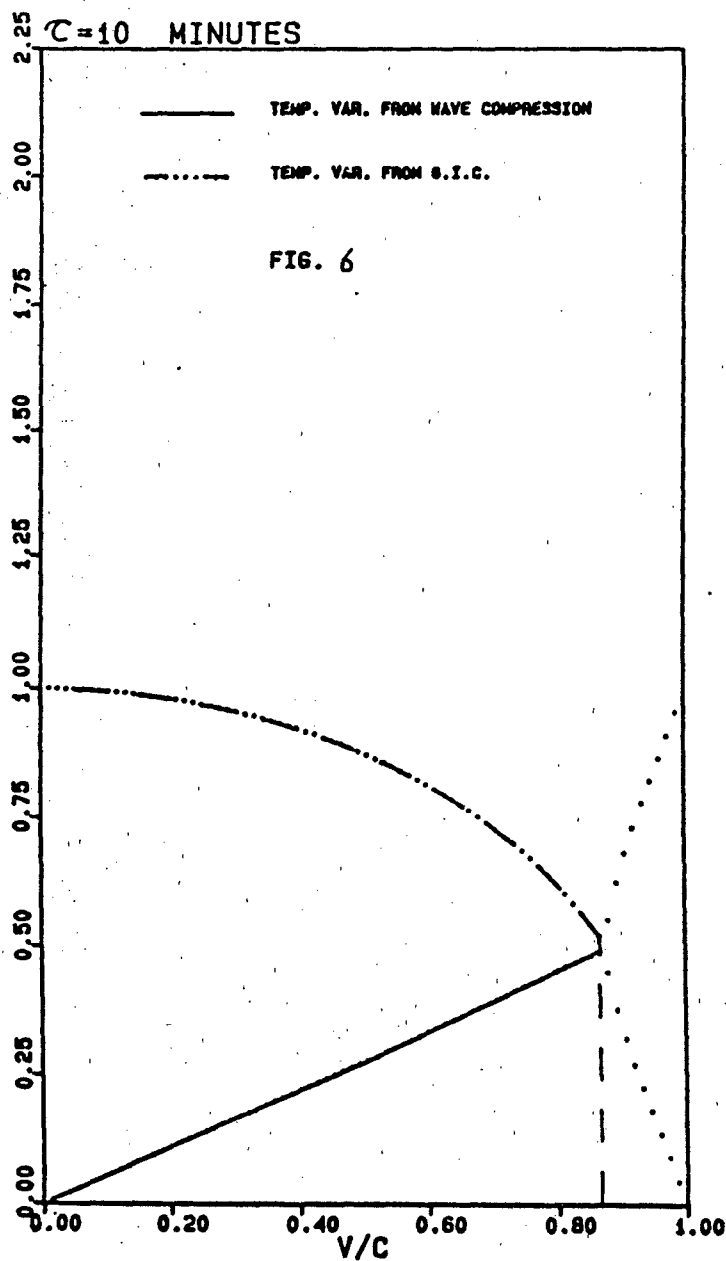
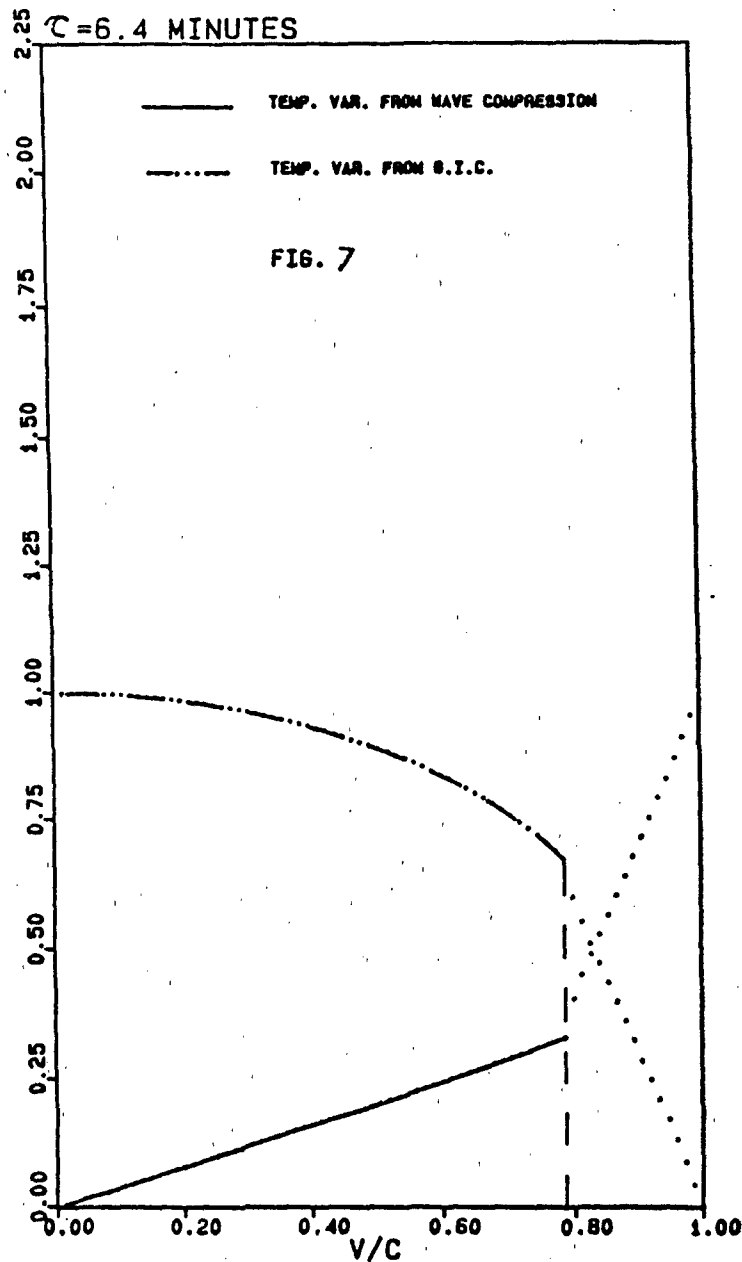


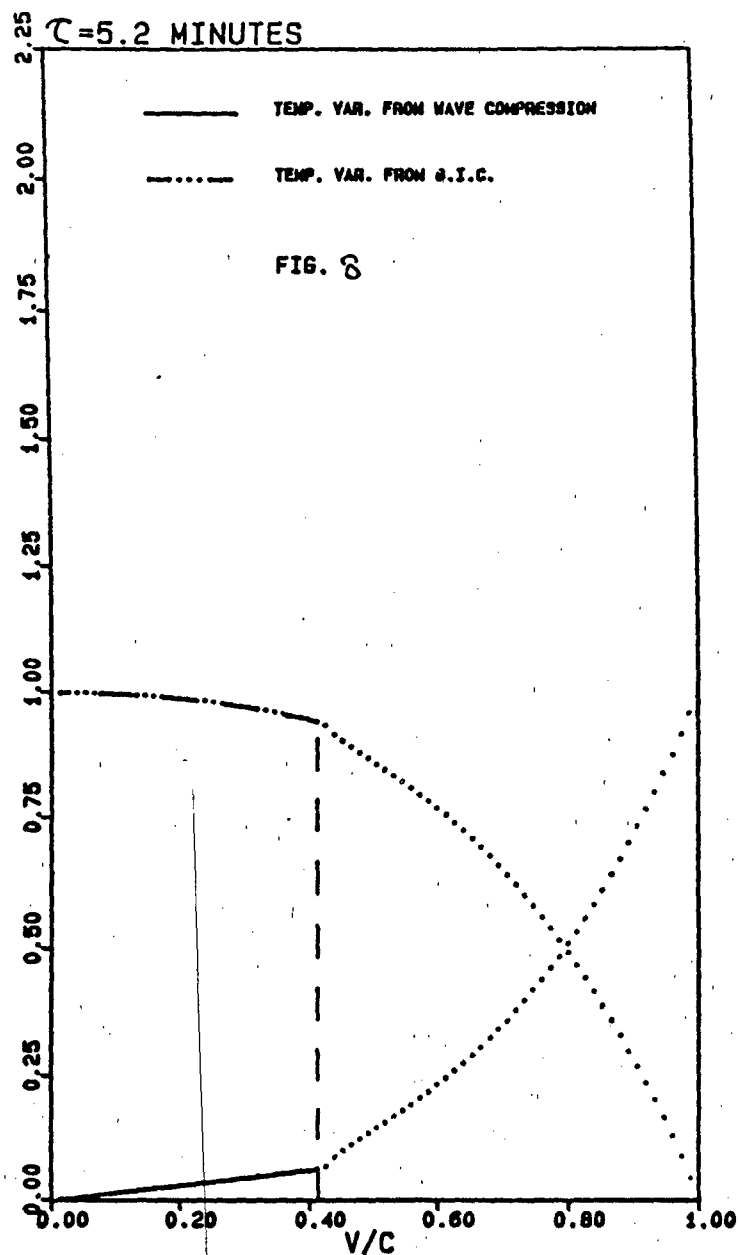
Figure 5 - a plot of the induced temperature variation due to the gravitational (red) and the acoustic compressions (black) as a function of v/c for wave periods 30 min.



Figures 6, 7, 8 - plots of the induced temperature variation due to the gravitational (red) and the acoustic compressions (black) as a function of v/c for wave periods = 10, 6.4, 5.2 min. respectively.



Figures 6, 7, 8 - plots of the induced temperature variation due to the gravitational (red) and the acoustic compressions (black) as a function of v/c for wave periods = 10, 6.4, 5.2 min. respectively.



Figures 6, 7, 8 - plots of the induced temperature variation due to the gravitational (red) and the acoustic compressions (black) as a function of v/c for wave periods = 10, 6.4, 5.2 min. respectively.

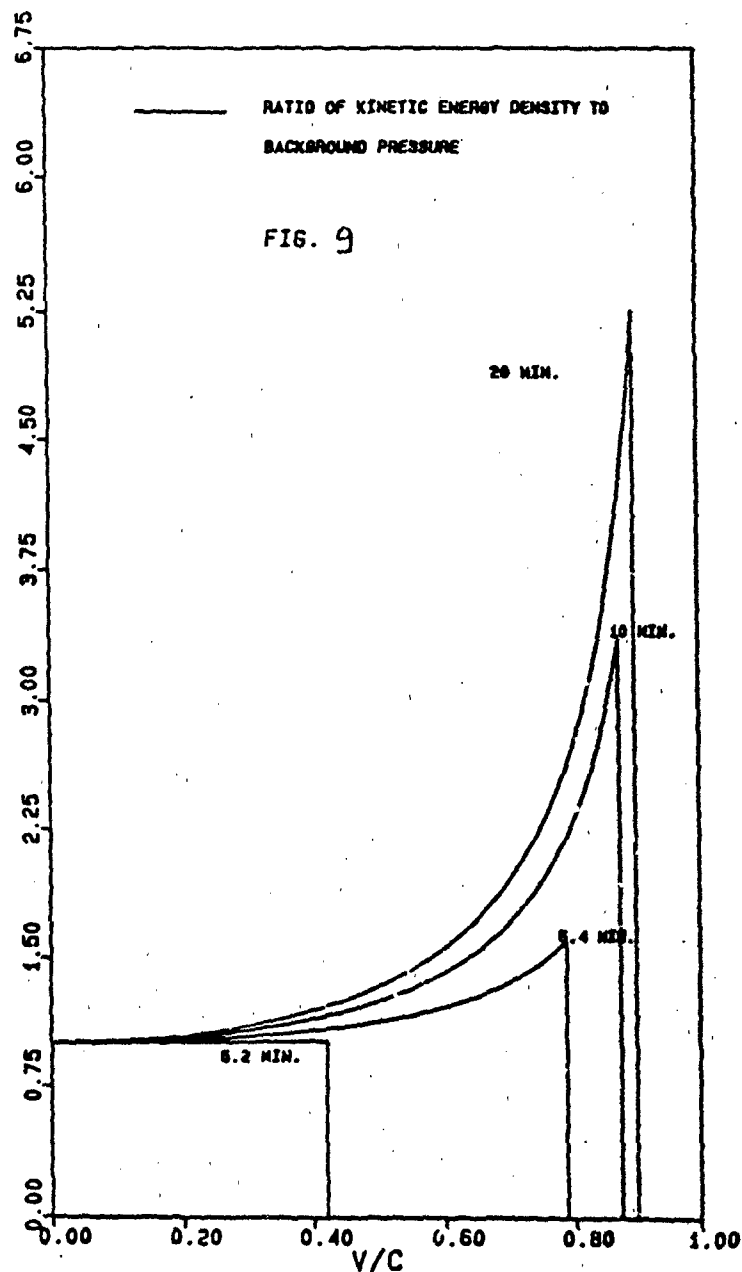


Figure 9 - a plot of the ratio of the kinetic energy density to the background pressure as a function of v/c for wave periods of 20, 10, 6.4 and 5.2 min.

Appendix I

We can derive equation (2) by using the usual expression for $\Delta\rho/\rho_0$, (Hines (1960)), given by

$$\frac{\Delta\rho}{\rho_0} = (\omega^2 k_z + i[(\gamma - 1)gk_x^2 - \frac{\gamma g \omega^2}{2c^2}])f \quad (A1)$$

$$\text{where } f = \alpha \frac{z}{2H} e^{i(\omega t - k \cdot r)}$$

We eliminate ω by using $\omega = k_x v$ and substitute in for the scale height $H = c^2/\gamma g$ to obtain,

$$\frac{\Delta\rho}{\rho_0} = (k_x^2 k_z v^2 + ik_x^2 c^2 [(\frac{\gamma-1}{\gamma})\frac{1}{H} - \frac{v^2}{2Hc^2}])f \quad (A2)$$

we obtain by adding and subtracting $(\frac{v}{c})^2 (\frac{\gamma-1}{\gamma H})$ in (A2)

$$\frac{\Delta\rho}{\rho_0} = (k_x^2 k_z v^2 + ik_x^2 c^2 [(1 - (\frac{v}{c})^2)(\frac{\gamma-1}{\gamma H}) - \frac{v^2}{Hc^2}(\frac{1}{\gamma} - \frac{1}{2})])f \quad (A3)$$

Introducing the vertical displacement field,

$$\frac{h}{H} = \frac{w}{L\omega H} = ik_x^2 c^2 (\frac{1}{H}) [1 - (\frac{v}{c})^2]f \quad (A4)$$

$$\text{we get } \frac{\Delta\rho}{\rho_0} = (\frac{\gamma-1}{\gamma})\frac{h}{H} + k_x^2 v^2 [k_z - i(1 - \frac{\gamma}{2})\frac{g}{c^2}]f \quad (A5)$$

Finally, we use $u = k_x^2 c^2 v [k_z - i(1 - \gamma/2)g/c^2]f$ to obtain

$$\frac{\Delta\rho}{\rho_0} = (\frac{\gamma-1}{\gamma})\frac{h}{H} + \frac{uv}{c^2} \quad (A6)$$

which is exactly equation (2).

Appendix II

From now on we consider only $k_z^2 > 0$ (i.e. k_z real). To obtain equation (3), we note (using (A4)),

$$\begin{aligned} \frac{|\Delta\rho|}{\rho_0} &= (\frac{\gamma-1}{\gamma})\frac{|h|}{H} = (\gamma-1)k_x^2 g [1 - (\frac{v}{c})^2] |f| \\ &= (\frac{\gamma-1}{\gamma}) (\frac{1}{H}) (\frac{c^2}{v^2} - 1) \omega^2 |f| \end{aligned} \quad (A7)$$

Using (A1), eliminating k_x and g , and substituting in $\eta = - (1-\gamma/2)g/c^2$ we obtain

$$\frac{|\Delta\rho|}{\rho_0} = (k_z^2 + [(\frac{\gamma-1}{\gamma})\frac{1}{H}(\frac{c^2}{v^2} - 1) + \eta]^2)^{1/2} \omega^2 |f| \quad (A8)$$

Using the dispersion relation (Hines, 1960), and letting $\epsilon = c^2/v^2 - 1$, we have

$$k_z^2 = \frac{\omega_b^2 - \omega^2}{v^2} - \frac{\omega_a^2 - \omega^2}{c^2} = \frac{\omega_b^2 - \omega^2}{c^2} \epsilon - |\eta|^2 \quad (A9)$$

where $\eta^2 = \frac{\omega_a^2 - \omega_b^2}{c^2}$

Thus,

$$\begin{aligned} \frac{|\Delta\rho_a|}{|\Delta\rho|} &= \frac{(\frac{\gamma-1}{\gamma})\frac{\epsilon}{H}}{(\frac{\omega_b^2 - \omega^2}{c^2} \epsilon + [(\frac{\gamma-1}{\gamma})\frac{1}{H}]^2 \epsilon^2 + \epsilon^2 \frac{(\gamma-1)}{\gamma H})^{1/2}} \\ &= \left[\frac{(\frac{\gamma-1}{\gamma})^2 \frac{\epsilon}{H^2}}{\frac{\omega_b^2 - \omega^2}{c^2} + [(\frac{\gamma-1}{\gamma})\frac{1}{H}]^2 \epsilon - (\frac{\gamma-1}{\gamma}) \frac{(2-\gamma)g}{Hc^2}} \right]^{1/2} \quad (A10) \end{aligned}$$

Using $\omega_b^2 = (\gamma-1)g^2/c^2$ and dividing it from the numerator and the denominator, we obtain

$$\frac{|\Delta\rho_a|}{|\Delta\rho|} = \left[\frac{(\gamma-1)\epsilon}{1 - (\omega/\omega_b)^2 + (\gamma-1)\epsilon + (\gamma-2)} \right]^{1/2}$$

so

$$\frac{|\Delta\rho_a|}{|\Delta\rho|} = \left[\frac{(\gamma-1)(1-(v/c)^2)}{(\gamma-1) - (\omega/\omega_b)^2 (v/c)^2} \right]^{1/2} \quad (A11)$$

which is equation (3).

To compute $|\Delta\rho_c|/|\Delta\rho|$, we note

$$\frac{\Delta\rho_c}{\rho_0} = \frac{v\omega}{c^2} = \frac{v}{c^2} (\omega k_x c^2 [k_z - i(1 - \frac{\gamma}{2})\frac{g}{c^2}]) f \quad (A12)$$

where, again, we use the polarization relation for u (Hines (1960)).

Substituting for η ,

$$\Delta\rho_c/\rho_0 = v/c^2 [\omega k_x c^2 (k_z + i\eta)] f \quad (A13)$$

$$\text{so } \frac{|\Delta \rho_c|}{|\Delta \rho|} = \left(\frac{k_z^2 + \eta^2}{k_z^2 + [((\gamma-1)/\gamma)(1/H)\epsilon + \eta]^2} \right)^{1/2} \quad (\text{A14})$$

where we have used (A8) and (A13).

Using (A9) we obtain:

$$\begin{aligned} \frac{|\Delta \rho_c|}{|\Delta \rho|} &= \left(\frac{\frac{\omega_b^2 - \omega^2}{c^2} \epsilon}{\left(\frac{\omega_b^2 - \omega^2}{c^2} \epsilon - \eta^2 \right) + \left[\frac{\gamma-1}{\gamma} \frac{\epsilon}{H} + \eta \right]^2} \right)^{1/2} \\ &= \left(\frac{(\omega_b^2 - \omega^2)/c^2}{(\omega_b^2 - \omega^2)/c^2 + [((\gamma-1)/\gamma)(1/H)]^2 \epsilon + 2(\gamma-1)\eta/\gamma H} \right)^{1/2} \end{aligned}$$

$$\text{so } \frac{|\Delta \rho_c|}{|\Delta \rho|} = \left(\frac{1 - (\omega/\omega_b)^2}{(\gamma-1) - (\omega/\omega_b)^2} \frac{(v/c)^2}{(v/c)^2} \right)^{1/2} (v/c) \quad (\text{A15})$$

which is equation (4).

Appendix III

From (10) we write

$$\begin{aligned} \frac{\Delta T}{T_0} &= (\gamma-1) \frac{v u}{c^2} - \frac{(\gamma-1)h}{\gamma H} \\ &= (\gamma-1) (v/c^2 [\omega k_x c^2 (k_z + i\eta)] - i k_x^2 g (v/c)^2 (c^2/v^2 - 1)) f \quad (\text{A16}) \end{aligned}$$

where we have used (A4) & (A13). Thus,

$$\Delta T/T_0 = (\gamma-1) k_x^2 v^2 (k_z + i[\eta - g/c^2 (c^2/v^2 - 1)]) f$$

since $\frac{\Delta T_a}{T_0} = - \frac{\Delta \rho_a}{\rho_0}$ (see (12)), we obtain by using (A7)

$$\frac{|\Delta T_a|}{|\Delta T|} = \frac{(\gamma-1) (k_x^2 v^2 g/c^2) \epsilon}{(\gamma-1) k_x^2 v^2 [k_z^2 + (\eta - (g/c^2)\epsilon)^2]^{1/2}} \quad (\text{A17})$$

Using again the dispersion relation for k_z^2 , we obtain

$$\begin{aligned} \frac{|\Delta T_a|}{|\Delta T|} &= \frac{(g/c^2) \epsilon}{\left[\frac{\omega_b^2 - \omega^2}{c^2} \epsilon - \frac{2\eta g}{c^2} \epsilon + \frac{g^2}{c^4} \epsilon^2 \right]^{1/2}} \\ &= \frac{1/2}{[1 - (\omega^2/c^2)/g^2 + \epsilon]^{1/2}} \end{aligned}$$

$$= \left(\frac{1 - (v/c)^2}{1 - (\omega^2 v^2)/g^2} \right)^{1/2}$$

$$\text{so } \frac{|\Delta T_A|}{|\Delta T|} = \left(\frac{1 - (v/c)^2}{1 - (\gamma-1)(\omega/\omega_D)^2 (v/c)^2} \right)^{1/2} \quad (\text{A18})$$

which is equation (13).

Equation (14) may be similarly obtained. The denominator is the same as (13) as expected, but the numerator is given by $|(\gamma-1)uv/c^2|$ which is identical to (4) except for the additional $(\gamma-1)$ factor.

Appendix IV

The K.E. density is given by:

$$\text{K.E.} = 1/4 \rho_0 (|u|^2 + |w|^2) \quad (\text{A19})$$

From Hines (1960) and the definition of $\bar{\eta}$, we may write

$$u = \omega k_x c^2 [k_z + i\eta] f \quad (\text{A20})$$

$$w = -\omega k_x^2 c^2 [1 - (v/c)^2] f \quad (\text{A21})$$

$$\text{so } |u|^2 = \frac{k_z^2 + \eta^2}{k_x^2 (1 - (v/c)^2)^2} |w|^2$$

From the disperison relation

$$\left(\frac{k_z}{k_x}\right)^2 = \frac{\omega_D^2 \omega^2}{\omega^2} - \left(\frac{v}{c}\right)^2 \frac{\omega_A^2 - \omega^2}{\omega^2}$$

and

$$\frac{|\eta|^2}{k_x^2} = \left(\frac{v}{c}\right)^2 \frac{\omega_A^2 - \omega^2}{\omega^2}$$

$$\text{Hence, } |u|^2 + |w|^2 = |w|^2 \left(1 + \frac{[(\omega_D^2/\omega^2) - 1][1 - (v/c)^2]}{(1 - (v/c)^2)^2} \right) \quad (\text{A22})$$

The total K.E. then becomes:

$$\text{K.E.} = \frac{1}{4} \rho \omega_B^2 |h|^2 \frac{[1 - (\omega/\omega_B)^2 (v/c)^2]}{[1 - (v/c)^2]} \quad (\text{A23})$$

Obviously (A23) is equation (19).

III. NONLINEAR RESPONSES

PART A: On the Nonlinear Response of Airglow to Linear Gravity Waves

J. R. Isler^{*,†}, T. F. Tuan^{*}, R. H. Picard[#] and U. Makhlof[‡]

^{*} Physics Department
University of Cincinnati
Cincinnati, Ohio 45221

[#] Optical Environment Division (OPS)
Geophysics Directorate, Phillips Laboratory
Hanscom AFB, Bedford, MA 01731

[†] Present Address: Geophysical Institute
University of Alaska, Fairbanks, AK 99775

[‡] Present Address: Optical Environment Division (OPS)
Geophysics Directorate, Phillips Laboratory
Hanscom AFB, Bedford, MA 01731

Abstract

The question of whether a linear gravity wave will give rise to nonlinear effects in ground-based airglow observations is important for the proper interpretation of gravity wave dynamics. In this paper, we obtain a closed form solution for the integrated airglow response to a linear gravity wave, containing all the higher-order nonlinear response terms. A comparison is made to the linear response, and the higher orders are seen to be significant. In addition, the wave-induced airglow intensity fluctuations are shown to be much greater than the corresponding major species density fluctuations.

1. Introduction

Ground-based airglow observations have often been used for studying middle and upper atmospheric dynamics. The common assumption has been that the airglow intensity (or "brightness") fluctuations correspond directly to atmospheric disturbances. However, if the airglow response is nonlinear, many of the airglow power spectrum peaks may be due to the nonlinearity of the airglow response, rather than an indication of the actual dynamic behavior of the atmosphere as a whole. This paper deals primarily with the purely dynamical effects of a linear gravity wave on airglow as observed by ground-based equipment. We ignore, as have other authors, photochemistry, quenching, and molecular/eddy diffusion on the time scale of the wave period.

Minor species involved in airglow reactions often have a layered structure, i.e. a sharply peaked unperturbed density profile, with a very steep vertical gradient just below the peak. As a consequence, it has been realized for some time that the fluctuation of the minor constituent's density, induced by a linear gravity wave, can be very large at a point where its unperturbed gradient is steep. For example, a linear gravity wave which produces a 10% density fluctuation in the major species may induce a 50-100% density fluctuation in the minor species at the same point. Thus, the local response of the minor species at particular height levels may not be amenable to a linear treatment.

Weinstock (1978) computed the first-order, linear airglow response and the unperturbed background airglow for $O_2(^1\Sigma^+_g)$ emissions. He also attempted to calculate the nonlinear response. Hines and Tarasick (1987) (hereafter, HT87) have recently questioned the necessity of invoking the higher-order nonlinear response terms produced by the steep gradient. They have reasoned that, while the local response may be nonlinear, the integrated response as measured from the ground should be linear, since the

effect of the large density gradient can be removed by the integration. They have demonstrated this by means of a transformation from the Eulerian to the semi-Lagrangian frame, in which the air parcels in motion due to the gravity wave are mapped back to their original resting positions (before the onset of the gravity wave). This is a very important result, since it permits, if true, a great simplification in calculating the column-integrated response of airglow to a gravity wave. Radar or resonance lidar which measures the local response of a minor species must contend with nonlinearities associated with steep gradients, leading to harmonics not present in the original wave perturbation; on the other hand, passive instruments such as photometers and radiometers, which measure total column brightness, effectively filter out such nonlinear responses.

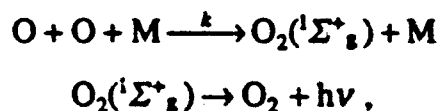
In this paper we reexamine the higher-order nonlinear terms in the semi-Lagrangian formulation of HT87 (for convenience "semi" will be dropped for the remainder of the paper). We propose to show that whilst the steep vertical density gradient of the minor species no longer shows up in the Lagrangian system, the higher-order response terms remain important. This is because a new nonlinearity is introduced by the Lagrangian transformation itself.

In general, an atmospheric field variable (for example, pressure or density) which is linear in its dependence on velocity at a fixed point (in Eulerian coordinates) may be nonlinear along a Lagrangian trajectory passing through that point. For example, while the density may fluctuate with a small amplitude at a fixed point, along a trajectory passing through that point it may fluctuate with a much larger amplitude, due in part to the large variation in background density and pressure experienced during vertical motion. By a simple extension of the procedure in HT87, it is possible to obtain the total airglow response to a general gravity wave in closed form, which can then be used to quantitatively demonstrate the importance of the higher-order nonlinear response terms.

It is tempting to think that the large nonlinear response in the Lagrangian frame is due implicitly to the steep density gradient in the Eulerian frame. However, we have not been able to show this explicitly. Nevertheless, we believe it is worthwhile to point out that the nonlinear response can be shown to be large, whatever frame is chosen for the calculation.

2. Airglow Intensity Fluctuations

Since we focus on purely dynamical effects which are largely independent of the particular radiator, we will discuss solely the $O_2(^1\Sigma^+_g)$ emission considered by Weinstock and by HT87. We ignore quenching and all other losses except radiative loss. We assume, for the sake of discussion, that this state is produced and destroyed solely through the reactions



where M denotes the major species, O is a minor species with a layered structure in the atmospheric region of interest (lower thermosphere and upper mesosphere) and k is the reaction rate. O is assumed to be a passive tracer of the atmospheric motions. The local intensity will be given by

$$I = k n^2 N \quad (1).$$

Here n (N) is the minor (major) species number density. The reaction rate k is known to be temperature-dependent, but again, for the sake of clarity and brevity, we will take it to be constant.

If we separate the number densities into an unperturbed part and a wave induced fluctuation

$$n(x,y,z,t) = n_0(z) + n'(x,y,z,t)$$

$$N(x,y,z,t) = N_0(z) + N'(x,y,z,t),$$

the volume emission rate profile, I , upon linearization, is given by

$$I = k n_0^2 N_0 \left[1 + 2 \frac{n'}{n_0} + \frac{N'}{N_0} \right] \quad (2).$$

However, as mentioned in section 1, the minor species number density, n , may require a nonlinear treatment even though the wave itself, carried by N , is linear. One method (Isler et al., 1988) is to solve for n order by order via a perturbation expansion in the velocity field, and so obtain n_1, n_2, n_3 and so forth. This allows one to calculate I to any order in the velocity field and thus obtain the column-integrated brightness

$$B = \int_0^{\infty} I dz \quad (3)$$

to any order in the velocity field. The results show that the higher-order terms are important and do not cancel.

HT87 maintained that the dynamical nonlinearities in I , which are local, are not present in B , which is height-integrated. To show this, they made two assumptions: (i) that n/N is conserved exactly along a parcel's trajectory and (ii) that the essentially nonlinear transformation from Eulerian to semi-Lagrangian coordinates can be adequately represented by a first-order Taylor expansion, given the linearity of the gravity wave carried by the major species. As to the first assumption, along a Lagrangian trajectory the continuity equations can be written

$$\frac{1}{N} \frac{dN}{dt} = -\nabla \cdot \bar{\mathbf{v}} \quad (4)$$

$$\frac{1}{n} \frac{dn}{dt} = -\nabla \cdot \bar{\mathbf{v}}_{\text{minor}} + \frac{P}{n} - L \quad (5),$$

where $\bar{\mathbf{v}}$ ($\bar{\mathbf{v}}_{\text{minor}}$) is the velocity of the major (minor) species and P and L are the production rate and loss frequency for the minor species. This implies

$$\frac{d}{dt}\left(\frac{n}{N}\right) = \frac{n}{N} \left[\nabla \cdot (\tilde{\mathbf{v}} - \tilde{\mathbf{v}}_{\text{mean}}) + \frac{P}{n} - L \right] \quad (6).$$

Thus, the first assumption is correct if production and loss processes are negligible over gravity wave time scales and, in addition, the two species have the same velocity fields at all times. But the former is only true for some airglow reactions (see, for example, Walterscheid et al., 1987), while the latter ignores the diffusion velocity of the minor species, inherent in any hydrostatically unstable density profile, such as a layered structure. The effects of such diffusion are not negligible during the transient onset of the gravity wave, nor during some fraction of each gravity wave period when the wave amplitude is small. However, for the remainder of this paper, we will ignore these effects of diffusion and chemistry and like HT87 allow that the mixing ratio is conserved along a trajectory. We turn now to the second assumption, namely the linearization of the Lagrangian transformation.

3. Lagrangian Formulation

A. The Exact Solution

We begin by writing the coupled set of equations expressing mass and momentum conservation and the adiabatic equation of state for the major species in the Eulerian system (using $D/Dt = \partial/\partial t + \tilde{\mathbf{v}} \cdot \nabla$):

$$\frac{1}{N} \frac{DN}{Dt} = -\nabla \cdot \tilde{\mathbf{v}} \quad (7)$$

$$N \frac{D\tilde{\mathbf{v}}}{Dt} = -\frac{1}{m} \nabla p + N\tilde{\mathbf{g}} \quad (8)$$

$$\frac{1}{m} \frac{Dp}{Dt} = c^2 \frac{DN}{Dt} \quad (9),$$

where m is the mean molecular mass, \bar{g} is the acceleration due to gravity and c is the speed of sound. Here, the only assumptions made are that m is constant and that the dissipative loss terms representing kinetic viscosity and heat conduction are negligible. These assumptions are generally valid in the mesosphere and lower thermosphere, where the $O_2(^1\Sigma^+_g)$ airglow and other important airglow emissions originate. Since the momentum transferred to the minor species is overwhelmingly dominated by collisions with the major species and since we neglect chemistry and diffusion, the minor species may be assumed to have the same velocity and acceleration fields as the major species, so that $\bar{v}_{\text{minor}} = \bar{v}$, and the continuity equation for the minor species reduces to

$$\frac{1}{n} \frac{Dn}{Dt} = -\nabla \cdot \bar{v} \quad (10).$$

With no further assumptions, we can in principle solve equations (7)-(9) for the exact \bar{v} in the original Eulerian system. This allows us to transform the continuity equations, (7) and (10), using this \bar{v} into the Lagrangian system. Thus,

$$\frac{1}{N} \frac{dN}{dt} = -\nabla \cdot \bar{v} \quad (11)$$

$$\frac{1}{n} \frac{dn}{dt} = -\nabla \cdot \bar{v} \quad (12).$$

We next integrate these equations along the trajectory of a fluid parcel, from time $t = 0$, before the gravity wave arrives when the

parcel is at rest at $z = \zeta$, to time t , when the parcel is moving with velocity \vec{v} . We obtain

$$N = N_o(\zeta) \exp \left(- \int_0^t \nabla \cdot \vec{v} dt' \right) \quad (13)$$

$$n = n_o(\zeta) \exp \left(- \int_0^t \nabla \cdot \vec{v} dt' \right) \quad (14).$$

Equations (13) and (14) are a direct consequence of the mass conservation equations, (11) and (12). Obviously,

$$\frac{n}{N} = \frac{n_o(\zeta)}{N_o(\zeta)},$$

and the mixing ratio is conserved along the trajectory. The exponential term in these expressions is the Jacobian of the transformation from Lagrangian to Eulerian coordinates [see, e.g., Dutton (1986)], in agreement with the usual form in which the Lagrangian continuity equation is written,

$$N = \left| \frac{\partial(x,y,z)}{\partial(\zeta,\eta,\zeta)} \right|^{-1} N_o.$$

Clearly, the Jacobian in equations (13) and (14) is nonlinear in \vec{v} in general.

The Eulerian luminosity profile, $I_E = k n_E^2 N_E$ (where, in the future, the subscripts E and L will denote the Eulerian and Lagrangian systems, respectively), can then be transformed to the Lagrangian system as follows:

$$I_E = k n_E^2 N_E \rightarrow I_L = \begin{cases} k \left[\frac{n_o(\zeta)}{N_o(\zeta)} \right]^2 N_L^3 & (15 a) \\ k \left[\frac{N_o(\zeta)}{n_o(\zeta)} \right]^2 n_L^3 & (15 b) \end{cases}$$

where the same expression for the conservation of the mixing ratio yields the two alternate forms (15a) and (15b). Using either form for I_L , the integrated brightness, B_L , is given by

$$B_L = \int_0^{\bar{z}} k n_o^2(\zeta) N_o(\zeta) \exp\left(-3 \int_0^{\zeta} \nabla \cdot \bar{v} dt'\right) \left(1 + \frac{\partial h}{\partial \zeta}\right) d\zeta \quad (16).$$

The factor after the exponential term is the Eulerian dz transformed to Lagrangian coordinates, using $z = \zeta + h$, where h is the vertical component of the parcel trajectory. In equation (16) and from now on, we assume that the horizontal fluid displacement is small compared to the horizontal wavelength. We are then justified in considering only the vertical trajectory. This was implicitly assumed by HT87.

This is the total integrated airglow response to a general gravity wave velocity field for the three-body reaction considered, neglecting only the effects of diffusion and chemistry. Note that, of course, the column-integrated brightness, being a real physical quantity, should be independent of the coordinate system used, so that $B_L = B_E$, where B_E is the Eulerian brightness integral. However, since the transformation from Eulerian to Lagrangian coordinates is nonlinear in \bar{v} , one cannot assume that, in a series expansion in \bar{v} , B_L will be equal to B_E term by term.

B. Approximation Schemes

We begin by making two observations. First, from equations (13) and (14) it is obvious that, along a trajectory, n and N vary as complicated functions of the trajectory. For a monochromatic simple harmonic trajectory with frequency ω , n and N are periodic with fundamental frequency ω and all the higher harmonics. The question is: Under what conditions are the higher-order harmonics negligible? Second, we note that any approximation scheme may violate some conservation principle. Actually, in this context, there are only two

basic conservation laws involved, namely the mass conservation of the minor and of the major species. From them, one can deduce the conservation of the mixing ratio. However, the converse is not true; the conservation of the mixing ratio does not imply that the species densities are each individually conserved. In HT87 the conservation of the mixing ratio was initially assumed. As a result, their subsequent Lagrangian linearization of the major species automatically forced the linearization of the minor species.

Before we consider the effect of linear gravity waves we consider a hypothetical wind or wave velocity, \bar{v} , which is exactly known and is carried by the major species. Once again, we neglect chemistry and diffusion and assume that $\bar{v}_{\text{minor}} = \bar{v}$ so that the behavior of the minor species is determined completely by (10).

We introduce a dimensionless parameter λ and let $\bar{v} \rightarrow \lambda \bar{v}$ so that the magnitude of the velocity can be adjusted by varying λ . Substituting $\lambda \bar{v}$ in (10), transforming into the Lagrangian system and integrating along the trajectory of a fluid parcel, we obtain

$$n = n_0(\zeta) \exp \left(-\lambda \int_0^t \nabla \cdot \bar{v} dt' \right) \quad (17),$$

where ζ is the vertical coordinate of the parcel before the wind or wave arrives at time $t = 0$.

Since \bar{v} is known exactly, n from (17) is a power series in λ . Clearly if λ is chosen small enough, we need only keep the first-order term in λ . If λ is large, on the other hand, we need to use many terms, or even the entire series which is summable in closed form. Thus for a given wind or wave velocity, $\lambda \bar{v}$, the Lagrangian density response is highly nonlinear in λ .

In the case of gravity waves we expand the dynamical variables of equations (7)-(9) in a power series in a dimensionless parameter λ (λ here does not mean quite the same thing as before). Thus,

$$\begin{aligned} p &= p_0 + \lambda p_1 + \lambda^2 p_2 + \dots \\ N &= N_0 + \lambda N_1 + \lambda^2 N_2 + \dots \\ \bar{v} &= \lambda \bar{v}_1 + \lambda^2 \bar{v}_2 + \dots \end{aligned} \quad (18),$$

where we have assumed that the velocity is entirely wave-induced (no prevailing wind), and, for convenience, we choose the coordinate system so that $\bar{v} = (u, v, w)$. Substituting this expansion into the dynamical equations and solving them to first order in λ gives the well-known expressions of Hines (1960) for \bar{v}_1 , p_1 , and N_1 . Solving the equations to λ^2 gives \bar{v}_2 , p_2 , and N_2 in terms of products of first-order terms. For example, \bar{v}_2 would be a linear combination of $N_1 p_1$, $N_1 \bar{v}_1$, \bar{v}_1^2 etc.. For $|u| \ll v_{phx}$, where v_{phx} is the horizontal phase trace speed, ω/k_x , one finds (Fritts, 1984),

$$\begin{aligned} \lambda^2 |\bar{v}_2| &\ll \lambda |\bar{v}_1| \\ \lambda^2 |p_2| &\ll \lambda |p_1| \\ \lambda^2 |N_2| &\ll \lambda |N_1| \end{aligned} \quad (19).$$

Here we can see that the power series expansion in λ given by the third line of (18) is an expansion for the major species velocity which has to satisfy the hydrodynamic equations, with major species background density, pressure, etc.. The expansion in λ given by (17) is an expansion in velocity for the minor species density which needs to satisfy only the continuity equation for the minor species, with a minor species background. The two are very different expansions and would not in general converge at the same rate.

Through (19) and the continuity equation for the major species it is easy to show that

$$\lambda^2 |\nabla \cdot \bar{v}_2| \ll \lambda |\nabla \cdot \bar{v}_1| \quad (20).$$

Thus, using $\bar{v} = \lambda \bar{v}_1 + \lambda^2 \bar{v}_2 + \dots$, equation (17) becomes

$$\begin{aligned}
n &= n_0(\zeta) \prod_{n=1}^{\infty} \exp \left[-\lambda^n \int_0^t (\nabla \cdot \bar{v}_n) dt' \right] \\
&= n_0(\zeta) \left\{ \exp^{-\lambda \int_0^t (\nabla \cdot \bar{v}_1) dt'} \exp^{-\lambda^2 \int_0^t (\nabla \cdot \bar{v}_2) dt'} \dots \exp^{-\lambda^n \int_0^t (\nabla \cdot \bar{v}_n) dt'} \dots \right\} \\
&= n_0(\zeta) \left\{ 1 - \lambda \int_0^t (\nabla \cdot \bar{v}_1) dt' + \frac{\lambda^2}{2!} \left[\int_0^t (\nabla \cdot \bar{v}_1) dt' \right]^2 \right. \\
&\quad \left. - \lambda^2 \int_0^t (\nabla \cdot \bar{v}_2) dt' + O(\lambda^3) \right\} \tag{21}.
\end{aligned}$$

In the second line of (21), we see that for each order of velocity perturbation, (\bar{v}_1 , \bar{v}_2 , etc.), the response of the minor species is in the form of an exponential function of that particular order: a very nonlinear response. In this paper we shall discard all the terms of $O(\lambda^2)$ and higher in the exponent of the second line of (21), leaving only the exponential response to a strictly linearized gravity wave, i.e. $\bar{v} = \lambda \bar{v}_1$. The same approximation was made by Gardner and Shelton (1985) when they also considered the nonlinear response to a linear gravity wave.

To see that there can be no cancellation between the higher-order terms in the nonlinear response to $\lambda \bar{v}_1$, and a corresponding higher-order term in the expansion of \bar{v} such as $\lambda^2 \bar{v}_2$, we consider the third line in (21). Of the two λ^2 terms on the right-hand side of (21) the first belongs to a series expansion of (17), the second belongs to the velocity expansion in (18), and, as already mentioned, the two series do not converge at the same rate. Furthermore, \bar{v}_1 and \bar{v}_2 are linearly independent so that there is no way (for arbitrary time t) that the two λ^2 terms can cancel. Indeed, owing to the oscillatory nature of \bar{v}_2 and the fact that the term involving \bar{v}_1 is always positive, there are times when the two terms would reinforce rather than partially cancel. Whilst for the larger gravity waves \bar{v}_2 may well be important, for this paper we shall only be concerned with a linear gravity wave, i.e. $\bar{v} = \lambda \bar{v}_1$, and as in the case of small

magnitude winds we shall consider the nonlinear response to a linear velocity perturbation (bearing in mind that the nonlinear response cannot in general be cancelled by higher-order terms such as \bar{v}_2). Our numerical results seem to show that the higher-order corrections in the expansion of (17), even for a gravity wave with a very modest amplitude (say a 4% fluctuation in the major species density, which should allow (20) to be valid), the nonlinear response of the airglow is important (see Table 1). From now on we shall omit writing λ .

It is customary in the Hines linear gravity wave model to replace the real fields \bar{v}_1 , P_1 and N_1 by complex fields to take advantage of the simplicity of the algebra in the complex notation. This is permissible because only linear transformations are carried out on the variables. It is tacitly understood that the real part is to be taken at the end of the calculation. On the other hand, when nonlinear transformations are carried out, as in the present case, greater care is required to ensure that only real quantities are used in nonlinear transformations. As an example, we note that, in squaring a sinusoidal field,

$$\cos^2 \omega t \neq \text{Re } e^{2i\omega t}$$

The right member correctly yields the second harmonic term, $\cos 2\omega t$, in \cos^2 , but completely misses the dc term. In our case, while we choose to keep the linear field variables \bar{v}_1 , P_1 and N_1 , complex, so that the usual linear theory may be applied, we also make sure to take the real part of the field variables that appear either in an exponent or in a product of terms.

In the linear theory, we have $\bar{v}_1 = \partial \bar{d}_1 / \partial t$ instead of $\bar{v}_1 = D \bar{d}_1 / Dt$, where \bar{d}_1 is the Eulerian displacement field (we keep only the linear terms in the Eulerian system; significant effects such as the Stokes drift (Coy et al., 1986) have been neglected). Thus, when the velocity

divergence is evaluated in the Eulerian frame prior to the Lagrangian transformation, we may set

$$\nabla \cdot \bar{\mathbf{v}}_1 = \frac{\partial(\nabla \cdot \bar{\mathbf{d}}_1)}{\partial t} \quad (22).$$

Since, unlike the major species, the minor species obeys only the continuity equation (10), with $\bar{\mathbf{v}} = \bar{\mathbf{v}}_1$, we transform this equation to the Lagrangian system exactly, keeping all orders in $\bar{\mathbf{v}}_1$. Later, we will investigate the magnitudes of the higher-order terms introduced by this transformation. Thus, using (14) and (22), after transforming to the Lagrangian system, we may write

$$\begin{aligned} n_L &= n_o(\zeta) \exp \left(-\text{Re} \int_0^t \frac{\partial(\nabla \cdot \bar{\mathbf{d}}_1)}{\partial t'} dt' \right) \\ &= n_o(\zeta) \exp \left[\text{Re}(-\nabla \cdot \bar{\mathbf{d}}_1|_t + \nabla \cdot \bar{\mathbf{d}}_1|_{t=0}) \right] \\ &= n_o(\zeta) \exp \left[\text{Re} \left(\frac{1}{\omega} \nabla \cdot \bar{\mathbf{v}}_1 \right) \right] \end{aligned} \quad (23),$$

where in the second step we have used the fact that all integrations are partial integrations, and in the last step we have, as stated, neglected any effects of the initial diffusion velocity so that at $t = 0$, taken to be before the onset of the gravity wave, $\bar{\mathbf{d}}_1 = 0$ for all x , y and z . At time t , we have assumed that the gravity wave has reached a steady asymptotic state with a monochromatic velocity field so that $\bar{\mathbf{v}}_1 = i\omega \bar{\mathbf{d}}_1$. The exact conservation of the mixing ratio then implies

$$N_L = N_o(\zeta) \exp \left[\text{Re} \left(\frac{1}{\omega} \nabla \cdot \bar{\mathbf{v}}_1 \right) \right] \quad (24).$$

With these expressions, we have the exact conservation of each species and of the mixing ratio. The column-integrated brightness of equation (16) becomes

$$B_L = \int_0^{\bar{\omega}} k n_0^2(\zeta) N_n(\zeta) \exp[\operatorname{Re}(3 \frac{1}{\omega} \nabla \cdot \bar{v}_1)] [1 - \operatorname{Re}(\frac{1}{\omega} \frac{\partial \bar{v}_1}{\partial \zeta})] d\zeta \quad (25).$$

The factor after the exponential reflects the fact that $h(z,t)$, in steady state, is a simple harmonic vertical trajectory.

It is important to stress again at this point that N_{2L} may be significant even though N_{2E} is negligible, and this is due to the nonlinearity of the transformation relating them. In fact, while N_L and N_E both refer to the major species, they are actually quite different physically; N_L being the density of one air parcel along its trajectory is affected by background variations over a cycle, while N_E is the density of a succession of air parcels passing through a fixed point where the background is fixed. So there is no reason to expect N_L and N_E to be the same, or even to converge at the same rate in a perturbation expansion. As evident in equation (24), following a closed, simple harmonic trajectory, $N_L = N_L(\bar{d}_1, t) = N_L(-\frac{1}{\omega} \bar{v}_1, t)$ is in general nonlinear in \bar{v}_1 , even though at any fixed point N_E may be linear in \bar{v}_1 . Again, the reason is the transformation from the Eulerian to the Lagrangian system, that is, the Jacobian given by the exponential in equation (24) is nonlinear in \bar{v}_1 .

This transformation was linearized by HT87 who transformed N_{1E} (which is already linear in \bar{v}_1) to the Lagrangian system via a linearized transformation, or a first-order Taylor expansion. Thus, according to HT87,

$$\begin{aligned}
N_e + N_{ie} &\rightarrow N_e(z(\zeta, t)) + N_{ie}(z(\zeta, t), t) \\
&= N_e(\zeta + h_1) + N_{ie}(\zeta + h_1, t) \\
&= N_e(\zeta) + \frac{dN_e}{d\zeta} h_1 + N_{ie}(\zeta) + O(\bar{v}_1^2) \\
&= N_e(\zeta) + \frac{dN_e}{d\zeta} h_1 + \frac{i}{\omega} N_e \nabla \cdot \bar{v}_1 + \frac{i}{\omega} \frac{dN_e}{d\zeta} w_1 + O(\bar{v}_1^2) \\
&= N_e(\zeta) \left(1 + \frac{i}{\omega} \nabla \cdot \bar{v}_1 \right) \zeta = N_e + N_{ie}
\end{aligned} \tag{26}$$

where the first two lines are nonlinear in \bar{v}_1 , while the last three are linearized. In going from the third line to the fourth line, the first-order Eulerian continuity equation for a sinusoidal wave,

$$i\omega N_{ie} = -N_e \nabla \cdot \bar{v}_1 - w_1 dN_e/d\zeta \tag{27}$$

has been used.

So far as we can see, the rationale behind this linearization is that if N_E is linear, then N_L , being still the major species, should also be used in its linearized form. However, N_E at a fixed point is a different function of \bar{v} from N_L which follows a trajectory through the same fixed point. In general if $g(\bar{v})$ and $f(\bar{v})$ are two arbitrary functions related by a transformation nonlinear in \bar{v} , the fact that $g(\bar{v})$ can be accurately linearized does not ensure that $f(\bar{v})$ can also be accurately linearized. Hence, in our case, the linearity of N_L does not follow from the linearity of N_E .

It is clear that equation (26) is the same as the first-order term of equation (24), as it should be. If we adopt this form for N_L , conservation of the mixing ratio would force n_L to acquire the same form. We then have the peculiar case of an exact conservation in the mixing ratio, while each species is conserved only to first order; a point we have mentioned earlier. In addition, if we now write equation (25) to first order in \bar{v}_1 , we obtain

$$B_L = \int_0^{\bar{\zeta}} k n_s^2(\zeta) N_o(\zeta) \left[1 + 3 \operatorname{Re} \left(\frac{i}{\omega} \nabla \cdot \bar{v}_1 \right) \right]_{\zeta} - \operatorname{Re} \left(\frac{i}{\omega} \frac{\partial w_1}{\partial \zeta} \right) \Big|_{\zeta} d\zeta \quad (28).$$

This is just the expression for B given by equation (20) of HT87 (with $\alpha=1$, $\beta=2$, $A=0$). (As remarked in HT87, this expression may also be obtained directly from the linearized Eulerian equation (2), after an integration by parts). The linearization of the coordinate transformation, called a Lagrangian linearization by HT87, has guaranteed a linear response for B.

To summarize this section, HT87 assumed that N_{1E} , being a solution to the linearized Eulerian hydrodynamic equations, could be transformed linearly to the Lagrangian system with no loss of accuracy. Then, through the constancy of the mixing ratio, (15a) was employed to express I_L in terms of N_{1L} , which upon further linearization gave equation (28). We, in contrast, use (15b), which is just as valid as (15a), to express I_L in terms of n_L . Since n_E satisfies a single equation (the continuity equation) exactly, in the Lagrangian system the solution n_L must satisfy equation (23). With the constancy of the mixing ratio we obtain equation (25). If the transformation can be accurately linearized, as HT87 assumed, there should be no significant difference between using either equation (25) or (28). We now explicitly calculate the higher-order Lagrangian terms, to determine if this is true.

4. Importance of the Higher Order Terms

To first order in \bar{v}_1 in the Eulerian system, using the polarization relations of Hines (1960), one can show (Makhlouf et al., 1989)

$$\frac{N_{1E}}{N_o} = \frac{(\gamma-1) h_1}{\gamma H} + \frac{\mathbf{v}_E \cdot \mathbf{u}_1}{c^2} \quad (29).$$

Here, γ is the ratio of specific heats and H is the atmospheric density scale height. Combining this with the first-order continuity equation, equation (27), we have

$$\begin{aligned}\frac{i}{\omega} \nabla \cdot \bar{v}_1 &= \frac{i w_1}{\omega H} + \frac{N_{1E}}{N_0} \\ &= -\frac{h_1}{H} + \frac{(\gamma-1) h_1}{\gamma H} + \frac{v_{rms} u_1}{c^2}.\end{aligned}$$

Thus, to first order in \bar{v}_1 in the Lagrangian system, using equation (24),

$$\frac{N_{1L}}{N_0} = \frac{i}{\omega} \nabla \cdot \bar{v}_1 = -\frac{h_1}{\gamma H} + \frac{v_{rms} u_1}{c^2} \quad (30).$$

For the small scale waves ($v_{phs} \ll c$), often found in middle atmosphere airglow, we may neglect the second term on the right-hand sides of (29) and (30) and obtain

$$\frac{|N_{1L}|}{N_0} = \frac{1}{\gamma-1} \frac{|N_{1E}|}{N_0} = 2.5 \frac{|N_{1E}|}{N_0} \quad (31),$$

where we have used $\gamma = 1.4$. This demonstrates that the Lagrangian density fluctuation is larger than the Eulerian by a factor of 2.5. For larger scale waves, the relation is not so simple, but the Lagrangian density fluctuation remains on average significantly greater than the Eulerian density fluctuation. So, in an obvious expansion of I_L , the integrand of equation (25), we write

$$I_L = I_0 \left[1 + \frac{I_{1L}}{I_0} + \frac{I_{2L}}{I_0} + O(\bar{v}_1^3) \right]$$

$$= kn_0^2(\zeta) N_0(\zeta) \times \left\{ 1 + 3 \operatorname{Re} \left(\frac{i}{\omega} \nabla \cdot \bar{v}_1 \right) + \frac{9}{2} \left[\operatorname{Re} \left(\frac{i}{\omega} \nabla \cdot \bar{v}_1 \right) \right]^2 + O(\bar{v}_1^3) \right\} \quad (32).$$

Then, we obtain from equations (30) and (31)

$$\frac{|I_{1L}|}{I_0} = 3 \frac{|N_{1L}|}{N_0} = 7.5 \frac{|N_{1E}|}{N_0} \quad (33)$$

$$\frac{|I_{2L}|}{I_0} = 4.5 \left(\frac{|N_{1L}|}{N_0} \right)^2 = 28.1 \left(\frac{|N_{1E}|}{N_0} \right)^2 \quad (34)$$

or, dividing equation (34) by equation (33)

$$\frac{|I_{2L}|}{|I_{1L}|} = 1.5 \frac{|N_{1L}|}{N_0} = 3.75 \frac{|N_{1E}|}{N_0} \quad (35).$$

First of all, we notice from (33) that the first-order luminosity fluctuation in the Lagrangian system is 7.5 times the Eulerian major species density fluctuation; a 10% major species density fluctuation can produce a 75% brightness fluctuation. This is very similar to the purely Eulerian computations in which the first-order brightness fluctuation can be very large whilst the major species density fluctuation is only modest. Notice that this factor 7.5 is a product of two factors: a factor of 2.5 from equation (31), which shows that the first-order density fluctuation at a fixed point is only 40% of the fluctuation along a trajectory passing through that point; and a factor, 3, which reflects the conservation of the mixing ratio along a trajectory, coupled with the assumption that the airglow in question is produced by a three-body reaction.

Secondly, we note that for a 10% Eulerian density fluctuation the second-order intensity fluctuation is 37.5% of the first order, and 28.1% of the background -- clearly not insignificant. This agrees with the purely Eulerian calculations (Isler et al., 1988), in which the higher orders are also seen to be important. Table I shows the first- and second-order intensity fluctuations in the Lagrangian system against given Eulerian major species density fluctuations. We see in all cases that the second-order intensity fluctuation is greater than the first-order density fluctuation.

Table I.

$\frac{ N_{1E} }{N_0}$	$\frac{ I_{1L} }{I_0}$	$\frac{ I_{2L} }{ I_{1L} }$	$\frac{ I_{2L} }{I_0}$
4%	30%	15%	4.5%
6%	45%	22.5%	10.1%
8%	60%	30%	18%
10%	75%	37.5%	28.1%

Finally, while the two points mentioned above deal with local intensities and densities, the integrated brightness which is being measured will have the same numerical factors, and would hence be expected to remain important. We can convince ourselves of the importance of the nonlinear response terms by looking at the column brightness. In Fig. 1-4, we have used the Hines gravity wave model which satisfies the rigid surface ground boundary condition. The unperturbed density profiles (O , N_2 , etc.) were taken from the U. S. Standard Atmosphere (1976). Two types of diagrams have been plotted. One (Figures 1 and 4) deals with the variation of brightness as a function of horizontal phase trace speed, v_{phx} , at a fixed time and period. Oscillations occur because of the varying wavelengths produced by varying v_{phx} and the fact that the ground boundary condition ensures that all waves begin with the same phase. The second type of figure (Figures 2 and 3) illustrates the variation in brightness versus time at fixed v_{phx} .

Here we should mention that we assume the background to be approximately uniform so far as the gravity wave is concerned all the way up to and including the airglow region under discussion. The general gravity wave in the airglow region can then be a linear combination of an upwardly travelling Hines gravity wave and a vertically stationary non-evanescent Hines gravity wave. The latter provides for the large downward reflection from the sudden temperature rise at the base of the thermosphere for larger scale waves. For smaller scale waves there can sometimes be significant downward reflection from critical layer regions in the actual atmosphere (He et al., 1990). Since the primary purpose of the present paper is to demonstrate the importance of nonlinear airglow response, even for relatively small amplitude gravity waves, we use only the Hines gravity wave satisfying the rigid surface boundary condition; in the Eulerian system a perturbation expansion for this particular type of wave does not require renormalization and is therefore simpler to use.

In Fig.1, we show a plot of the first-order Lagrangian and first-order Eulerian brightness terms (which are the same, of course, because of the relation via integration by parts referred to above) at a fixed time but for different horizontal phase trace speeds, for a two-hour period gravity wave that induces a 5% major species density fluctuation at 97 km. In the same figure we have also plotted the second-order Lagrangian (dashed line) and second-order Eulerian (dotted line) terms. Clearly both are significant for all horizontal phase trace speeds. In Fig.2 we plot the first and second order terms for a fixed $v_{phx} = 150$ m/s as a function of time, where the maximum density fluctuation of the major species is again set to 5% at 97 km.

Fig. 3a-e show a comparison of the total Lagrangian brightness (equation (25), crosses), as a function of time, and the sum of the first three perturbation terms in the Eulerian brightness (dotted lines) as well as the first-order brightness (equation (28), solid lines), using the same parameters as Fig. 2. Each figure is drawn for a

different fractional major species density fluctuation at 97 km, beginning with 7.5% in Figs. 3a through 5%, 3.75%, 2.5% and ending with 0.5% for Fig. 3e. As can be seen, the nonlinear response, producing a cusp at the waveform crest and a flattening of the wave trough, is very important for the 7.5% case, and almost completely absent for 0.5%. Figs. 4a-e show the brightness response at a fixed time but for different horizontal phase trace speeds; the importance of the higher orders is clear.

5. Conclusion

The question of whether a linear gravity wave will give rise to higher-order harmonics of the basic gravity wave frequency in ground-based observations of airglow brightness fluctuations is important for the investigation of atmospheric dynamics, especially with regard to the proper interpretation of the power spectra of airglow data. That such harmonics are significant has been shown to be the case when they are calculated in the Eulerian and in the Lagrangian frames.

The net consequence of all this is that one would expect the frequent occurrence of higher-order harmonics in the power spectra of airglow brightness fluctuations. The results presented here may be tested by the simultaneous measurement of ground-based brightness fluctuations and local major species density fluctuations via radar or lidar or *in situ* instruments. Such an experiment could determine whether higher harmonics present in the nonlinear airglow response are in fact absent from the actual gravity wave fields.

Acknowledgements

We would like to thank E. A. Dewan and J. R. Winick for several helpful discussions. We would also like to acknowledge correspondence with D. W. Tarasick and C. O. Hines. This work was supported in part by the Air Force Office of Scientific Research and the Air Force Geophysics Laboratory, under Contract No. F19628-87-K-0023. The work was associated with the ARC/AARC Airglow Modeling and MAPSTAR programs.

References

- Coy, L., D.C. Fritts and J. Weinstock (1986). The Stokes drift due to vertically propagating internal gravity waves in a compressible atmosphere, *J. Atmos. Sci.*, 43, 2636.
- Dutton, J.A. (1986). The Ceaseless Wind, Dover.
- Fritts, D.C. (1984). Gravity wave saturation in the middle atmosphere: a review of theory and observations, *Rev. Geophys. Space Phys.*, 22, 275.
- Gardner, C.S. and J.D. Shelton (1985). Density response of neutral atmospheric layers to gravity wave perturbations, *J. Geophys. Res.*, 90, 1745.
- He, F., T.F. Tuan and J.R. Isler (1990). Gravity wave scattering from critical layer regions, *Eos*, 71, No. 17, 573.
- Hines, C.O. (1960). Internal gravity waves at ionospheric heights, *Can. J. Phys.*, 38, 1441.
- Hines, C.O., and D.W. Tarasick (1987). On the detection and utilization of gravity waves in airglow studies, *Planet. Space Sci.*, 35, 851.
- Isler, J.R., T.F. Tuan, U. Makhlof, R. Picard and P.L. Lin, (1988). Perturbation treatment of nonlinear airglow response to linear gravity waves II, *Eos*, 69, No. 44, 1342. (Also, in preparation).
- Makhlof, U., E. Dewan, J.R. Isler and T.F. Tuan, (1990). On the importance of the purely gravitationally induced density, pressure and temperature variations in gravity waves: their application to airglow observations, *J. Geophys. Res.*, 95, 4103.
- Walterscheid, R.L., G. Schubert, and J.M. Straus (1987). A dynamical-chemical model of wave-driven fluctuations in the OH nightglow, *J. Geophys. Res.*, 92, 1241.
- Weinstock, J. (1978). Theory of the interaction of gravity waves with $O_2(^1\Sigma_g)$ airglow, *J. Geophys. Res.*, 83, 5175

Figure Captions

Figure 1. Comparison of the second-order Eulerian and Lagrangian integrated brightness (with a second-order dc offset omitted) to the first-order integrated brightness (eqn. (28)), at a fixed time for a two hour period wave over a range of horizontal phase trace speeds (v_{phx}). The fractional major species density fluctuation (N_{1E}/N_0) at 97 km has been set to 5%. The vertical scale is given in arbitrary units.

Figure 2. The same as in Figure 1, but for a fixed v_{phx} of 150 m/s, plotted as a function of time. The fractional major species density fluctuation at 97 km has been set to 5%. The vertical scale is given in arbitrary units.

Figure 3. Comparison of the sum of the first three orders (including the dc offset) of the integrated brightness in the Eulerian system and the total Lagrangian integrated brightness (eqn. (25)) to the first-order integrated brightness (eqn. (28)), for a two-hour period wave with a horizontal phase trace speed of 150 m/s. The fractional major species density fluctuation at 97 km is 7.5% in Fig. 3a, 5% in Fig. 3b, 3.75% in Fig. 3c, 2.5% in Fig. 3d and 0.5% in Fig. 3e. The vertical scale is given in arbitrary units.

Figure 4. The same as in Figure 3, but at a fixed time and over a range of horizontal phase trace speeds. The vertical scale is given in arbitrary units.

Figure 1

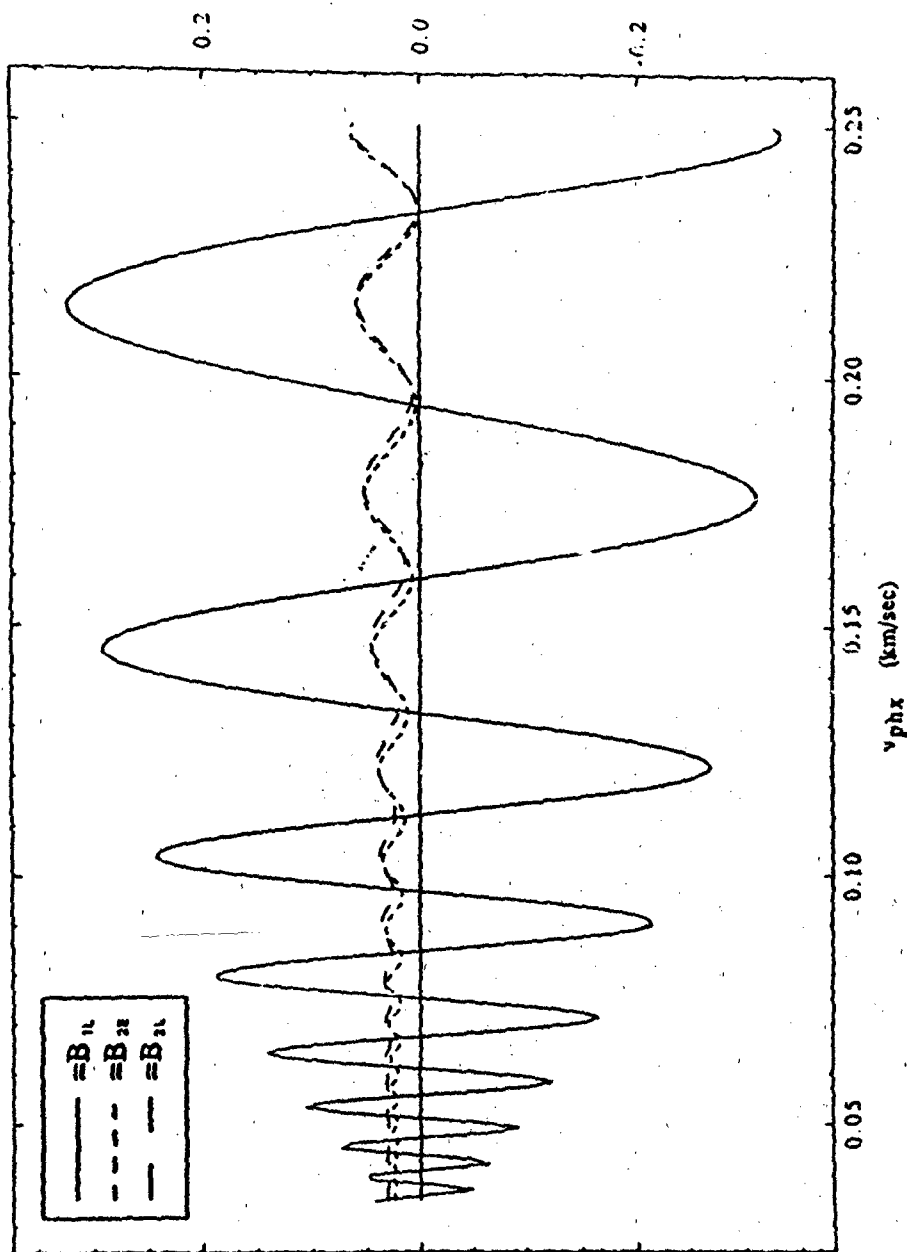


Figure 1 - Comparison of the second-order Eulerian and Lagrangian integrated brightness (with a second-order dc offset omitted) to the first-order integrated brightness (eqn. (28)), at a fixed time for a two hour period wave over a range of horizontal phase trace speeds (v_{phx}). The fractional major species density fluctuation (N_1E/N_0) at 97 km has been set to 5%. The vertical scale is given in arbitrary units.

Figure 2

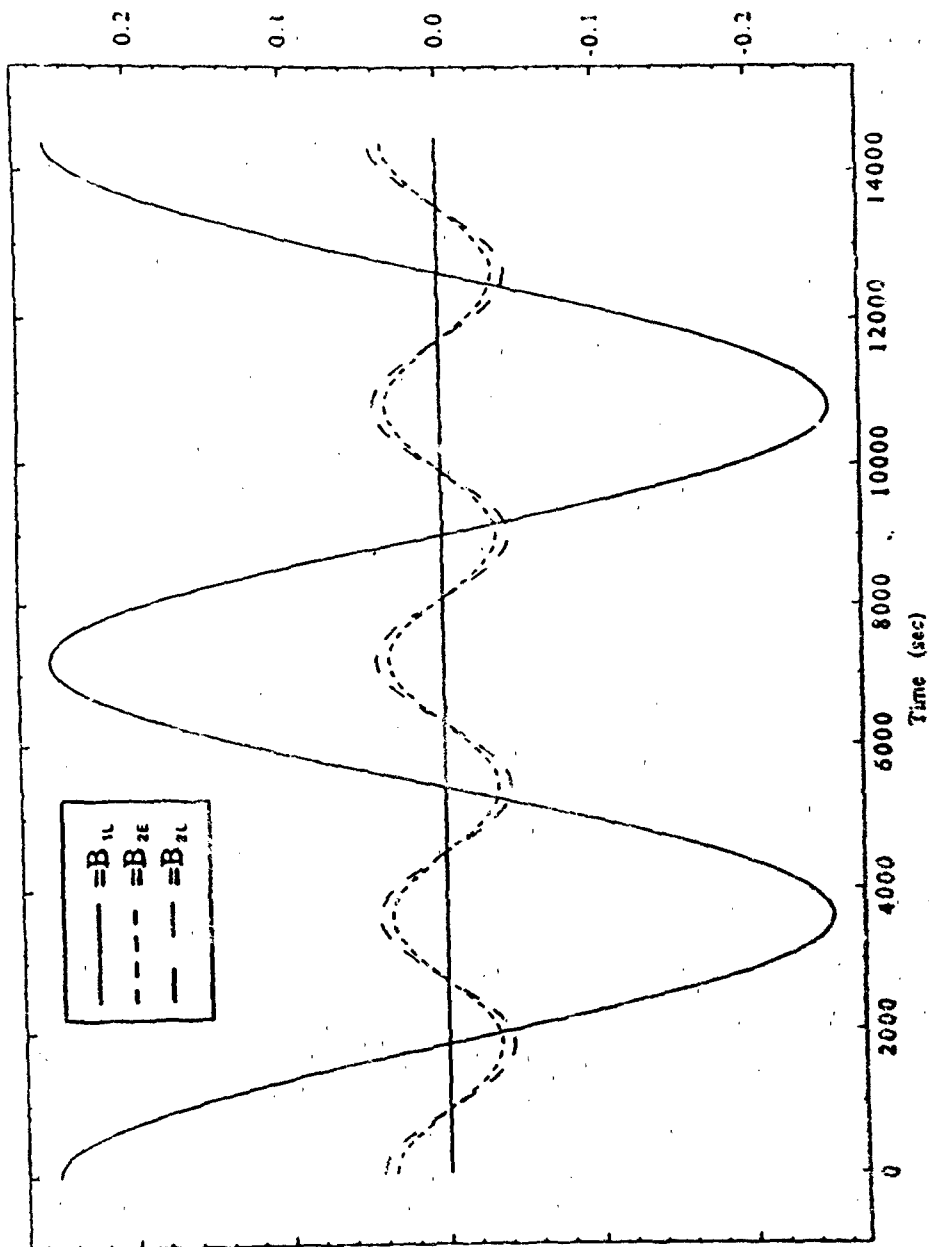


Figure 2 - The same as in Figure 1, but for a fixed v_{ph} of 150 m/s, plotted as a function of time. The fractional major species density fluctuation at 97 km has been set to 5%. The vertical scale is given in arbitrary units.

Figure 3a

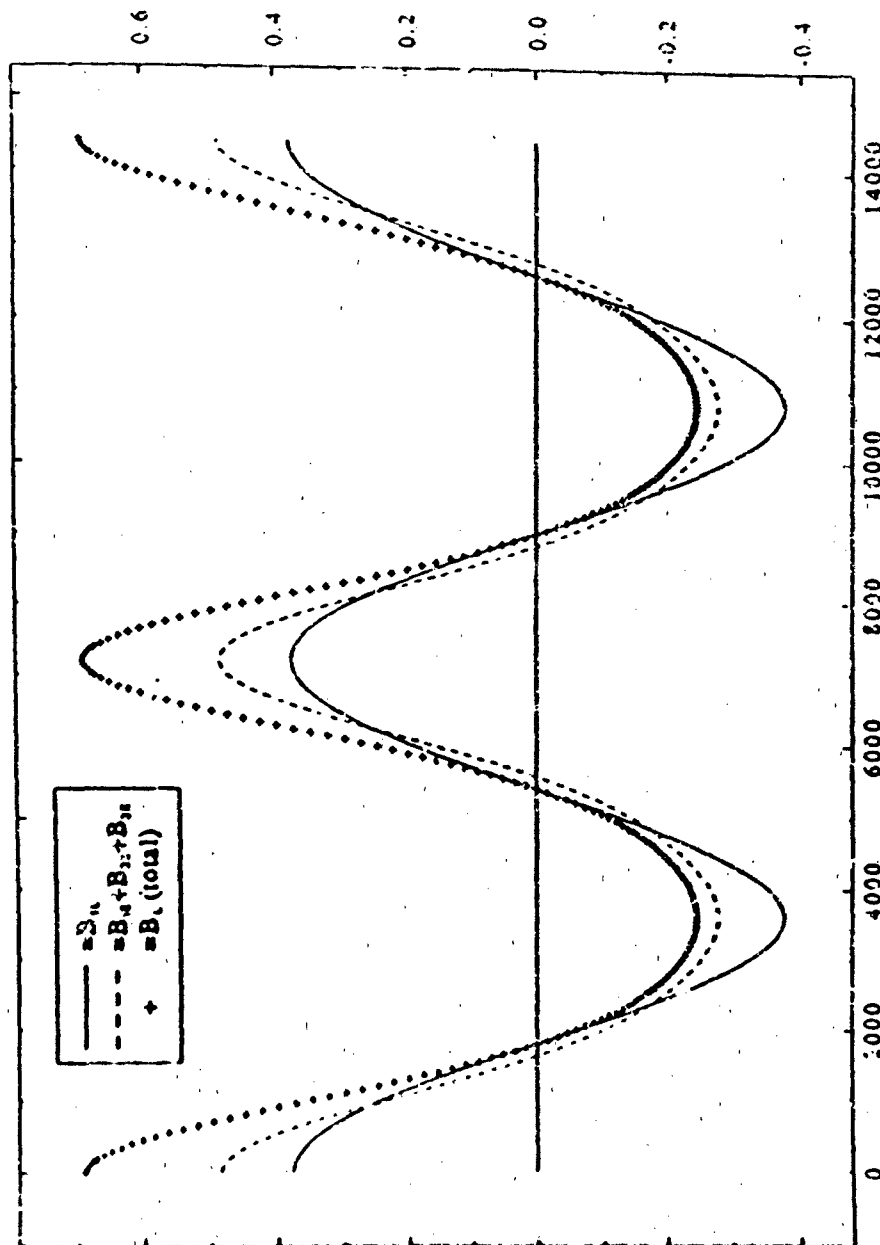


Figure 3 - Comparison of the sum of the first three orders (including the dc offset) of the integrated brightness in the Eulerian system and the total Lagrangian integrated brightness (eqn. 25) to the first-order integrated brightness (eqn. 28), for a two-hour period wave with a horizontal phase speed of 150 m/s. The fractional major species density fluctuation at 97 km is 7.5% in Fig. 3a, 5% in Fig. 3b, 3.75% in Fig. 3c, 2.5% in Fig. 3d and 0.5% in Fig. 3e. The vertical scale is given in arbitrary units.

Figure 3b

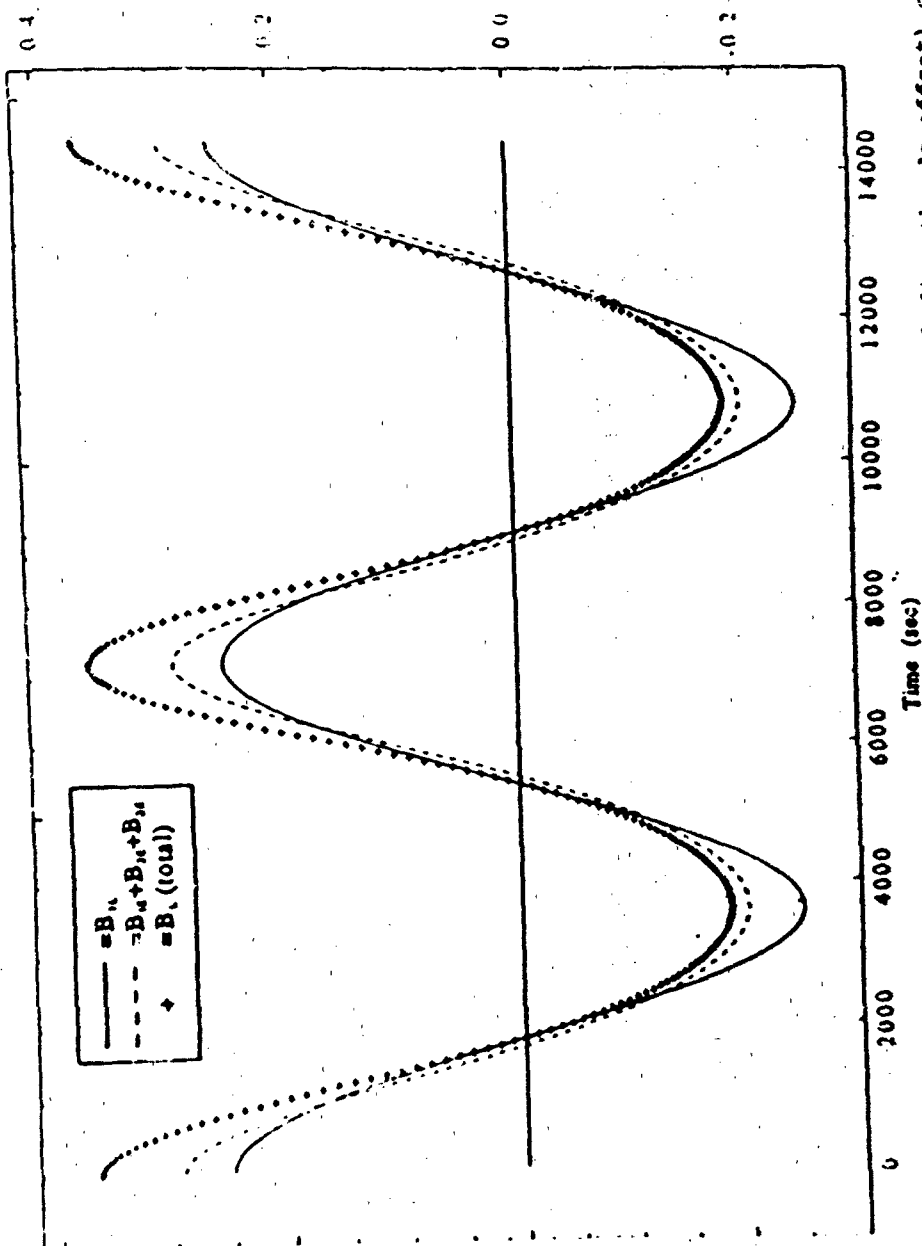


Figure 3 - Comparison of the sum of the first three orders (including the dc offset) of the integrated brightness in the Eulerian system and the total Lagrangian integrated brightness (eqn. 25) to the first-order integrated brightness (eqn. (28)), for a two-hour period wave with a horizontal phase trace speed of 150 m/s. The fractional major species density fluctuation at 97 km is 7.5% in Fig. 3a, 5% in Fig. 3b, 3.75% in Fig. 3c, 2.5% in Fig. 3d and 0.5% in Fig. 3e. The vertical scale is given in arbitrary units.

Figure 3c

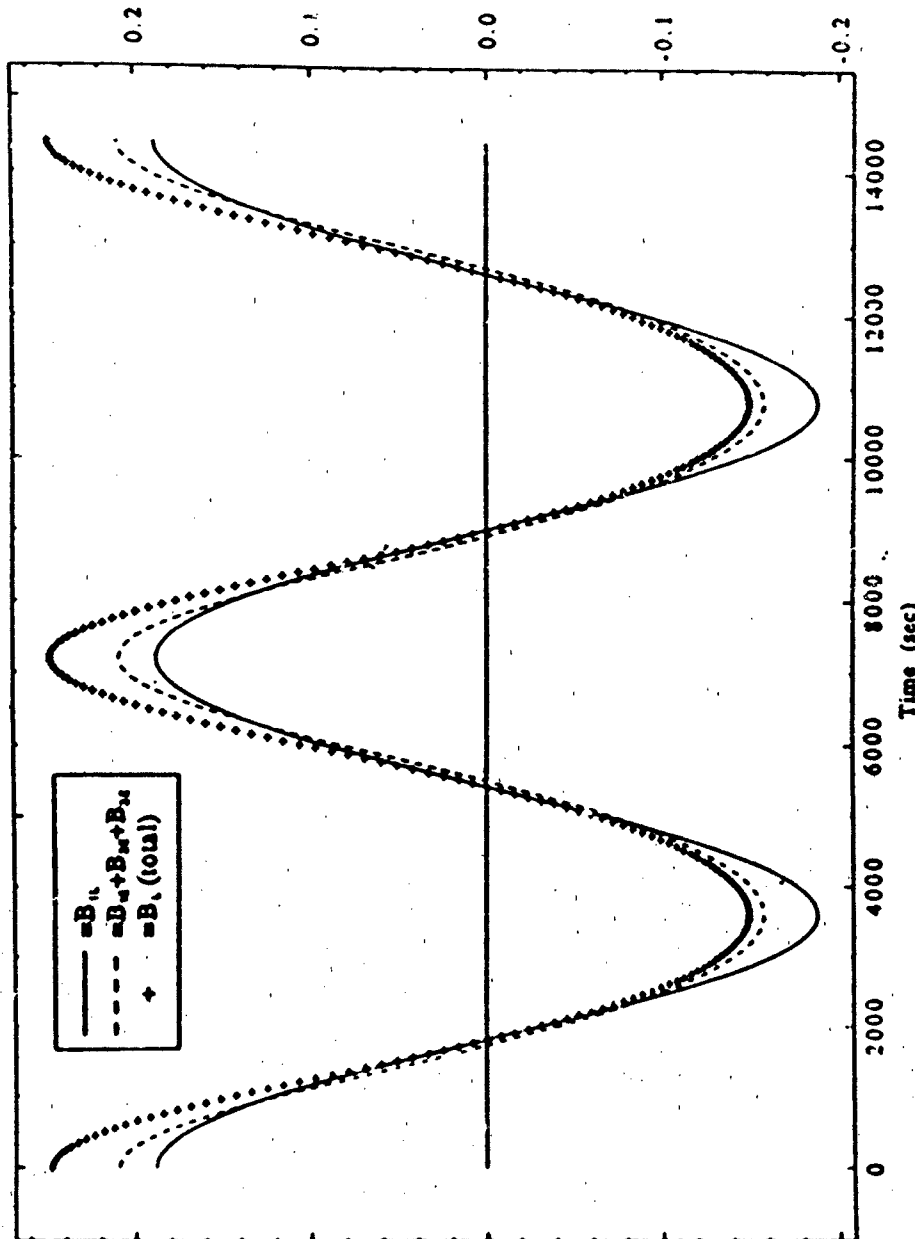


Figure 3 - Comparison of the sum of the first three orders (including the dc offset) of the integrated brightness in the Eulerian system and the total Lagrangian integrated brightness (eqn. 25)) to the first-order integrated brightness (eqn. (28)), for a two-hour period wave with a horizontal phase speed of 150 m/s. The fractional major species density fluctuation at 97 km is 7.5% in Fig. 3a, 5% in Fig. 3b, 3.75% in Fig. 3c, 2.5% in Fig. 3d and 0.5% in Fig. 3e. The vertical scale is given in arbitrary units.

Figure 3d

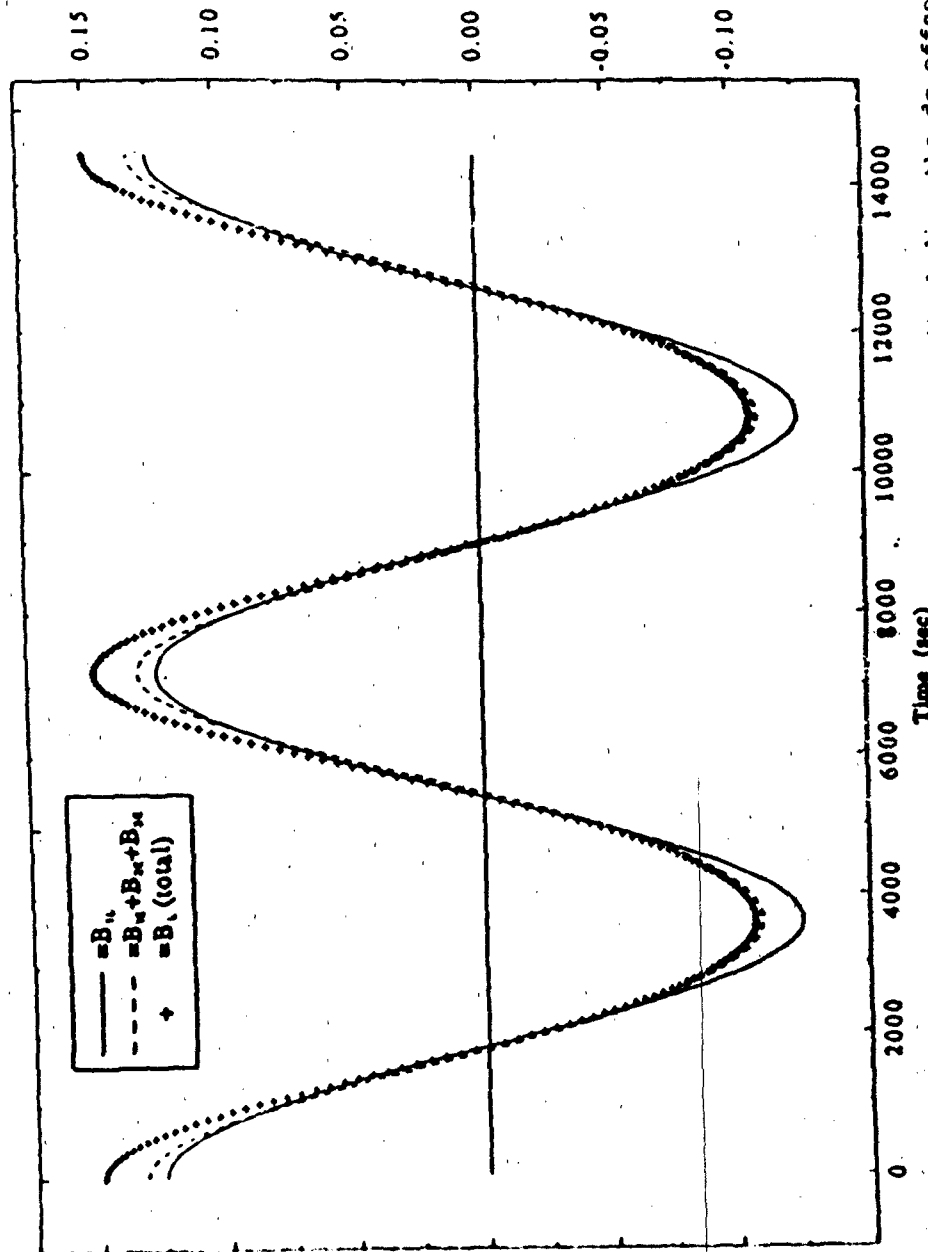


Figure 3 - Comparison of the sum of the first three orders (including the dc offset) of the integrated brightness in the Eulerian system and the total Lagrangian integrated brightness (eqn. 25) to the first-order integrated brightness (eqn. 28), for a two-hour period wave with a horizontal phase trace speed of 150 m/s. The fractional major species density fluctuation at 97 km is 7.5% in Fig. 3a, 5% in Fig. 3b, 3.75% in Fig. 3c, 2.5% in Fig. 3d and 0.5% in Fig. 3e. The vertical scale is given in arbitrary units.

Figure 3e

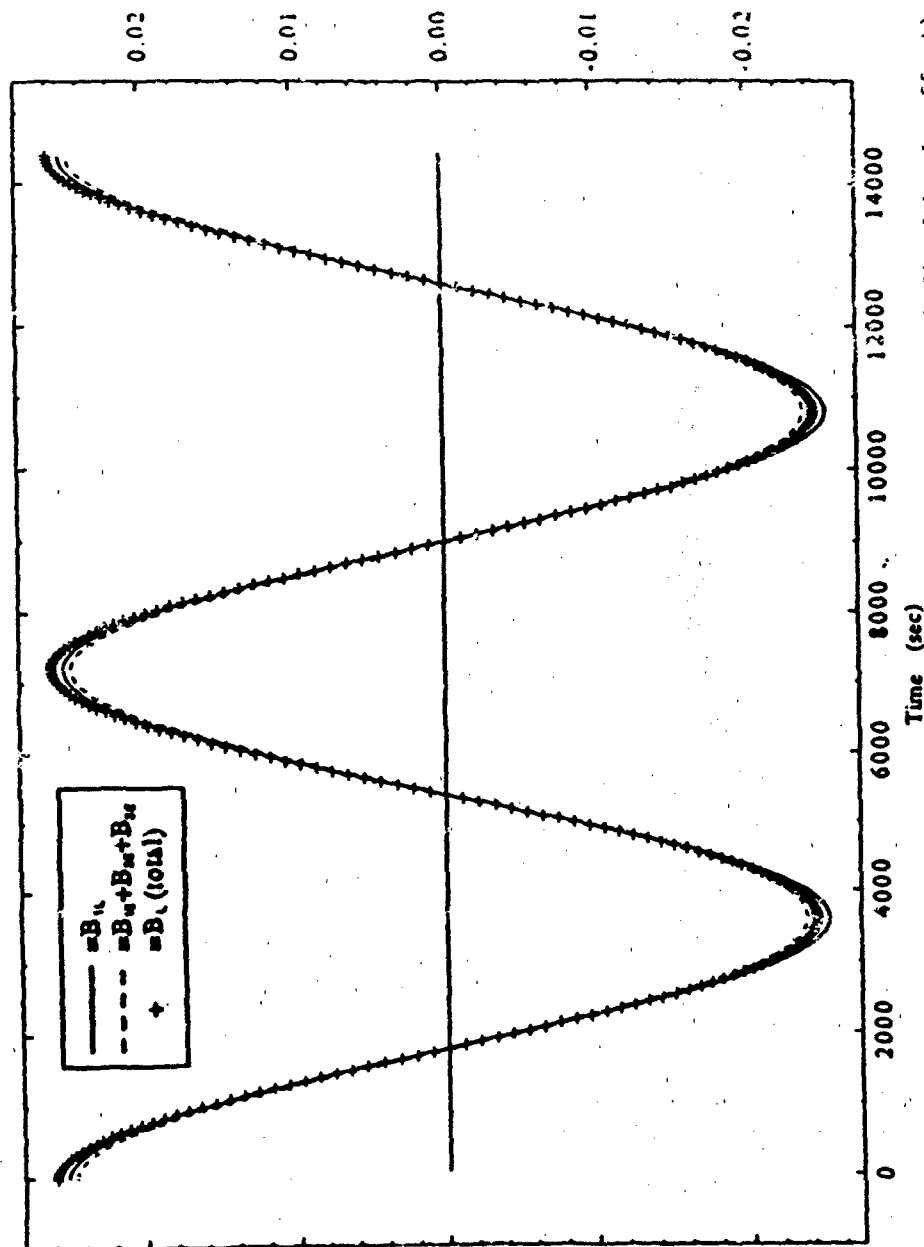


Figure 3 - Comparison of the sum of the first three orders (including the dc offset) of the integrated brightness in the Eulerian system and the total Lagrangian integrated brightness (eqn. 25) to the first-order integrated brightness (eqn. (28)), for a two-hour period wave with a horizontal phase speed of 150 m/s. The fractional major species density fluctuation at 97 km is 7.5% in Fig. 3a, 5% in Fig. 3b, 3.75% in Fig. 3c, 2.5% in Fig. 3d and 0.5% in Fig. 3e. The vertical scale is given in arbitrary units.

Figure 4a

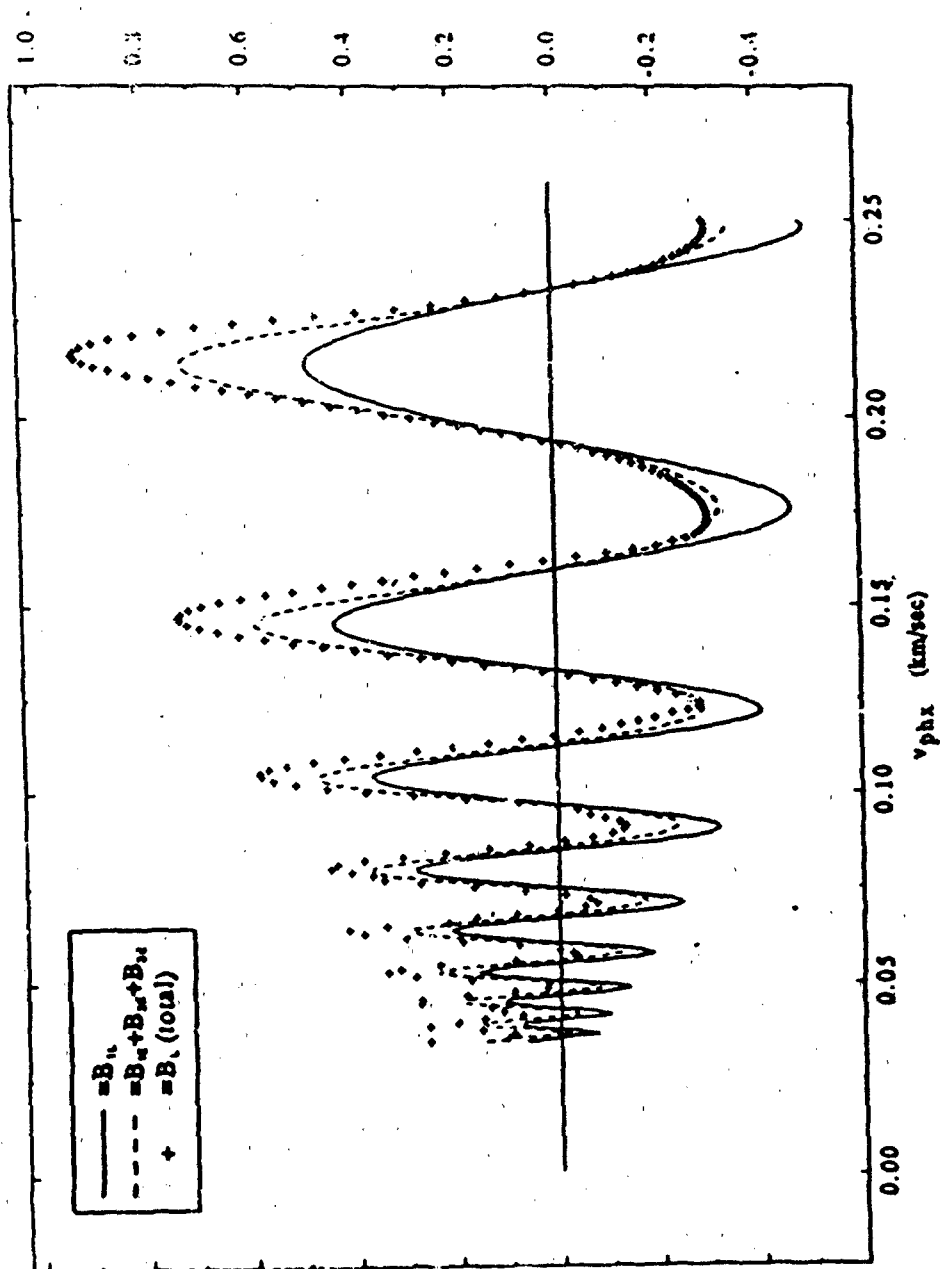


Figure 4 - The same as in Figure 3, but at a fixed time and over a range of horizontal phase trace speeds. The vertical scale is given in arbitrary units.

Figure 4b

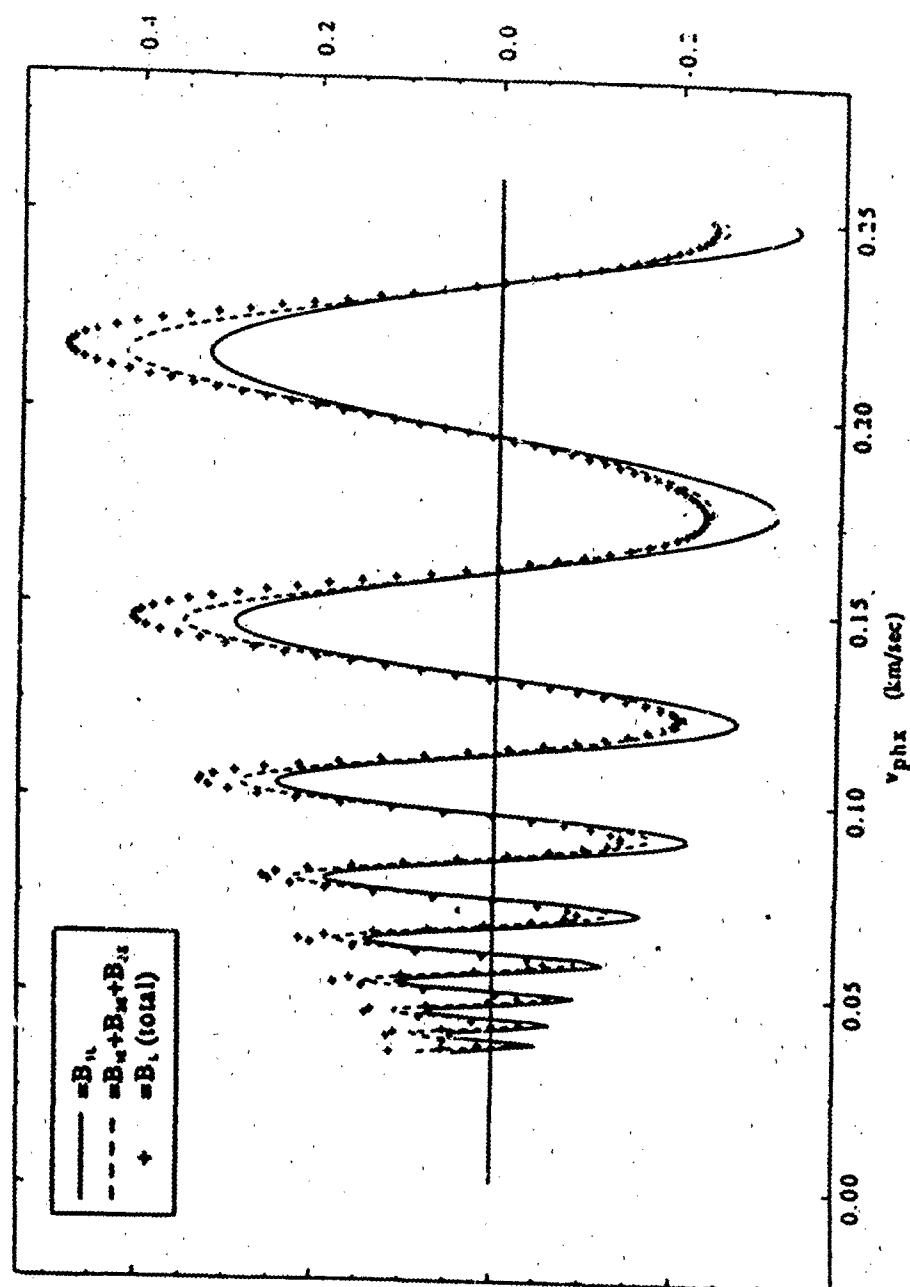


Figure 4 - The same as in Figure 3, but at a fixed time and over a range of horizontal phase trace speeds. The vertical scale is given in arbitrary units.

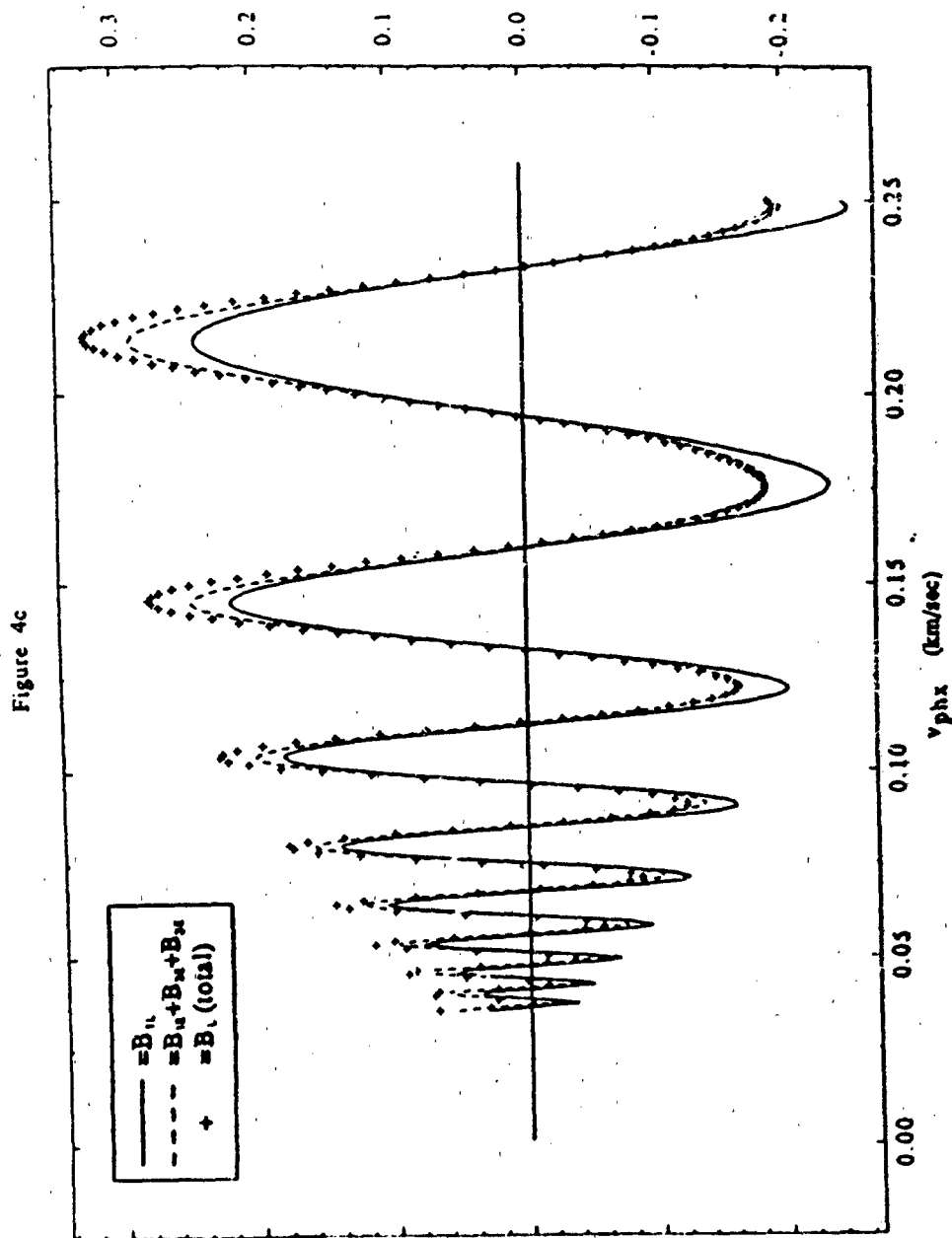


Figure 4 - The same as in Figure 3, but at a fixed time and over a range of horizontal phase trace speeds. The vertical scale is given in arbitrary units.

Figure 4d

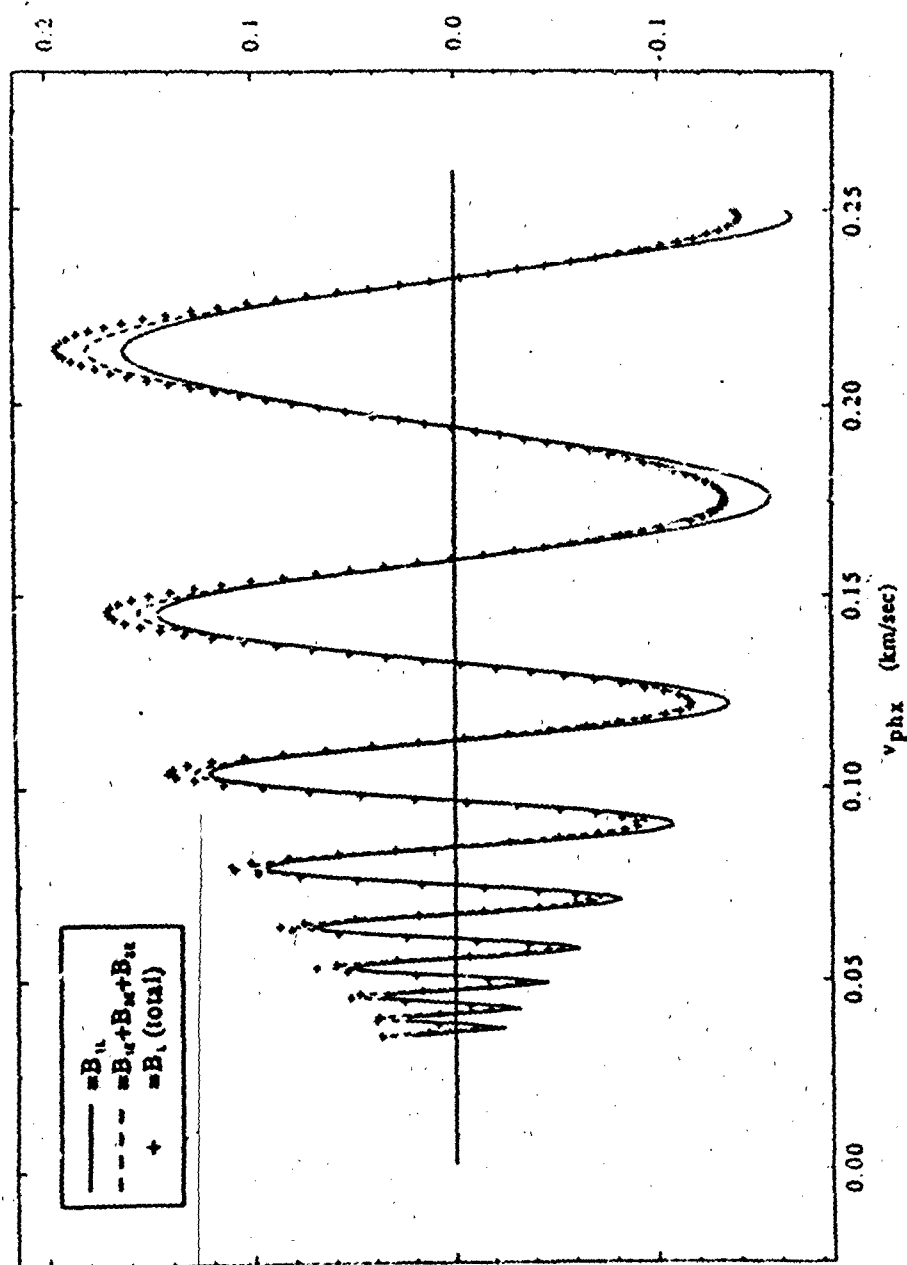


Figure 4 - The same as in Figure 3, but at a fixed time and over a range of horizontal phase trace speeds. The vertical scale is given in arbitrary units.

Figure 4e

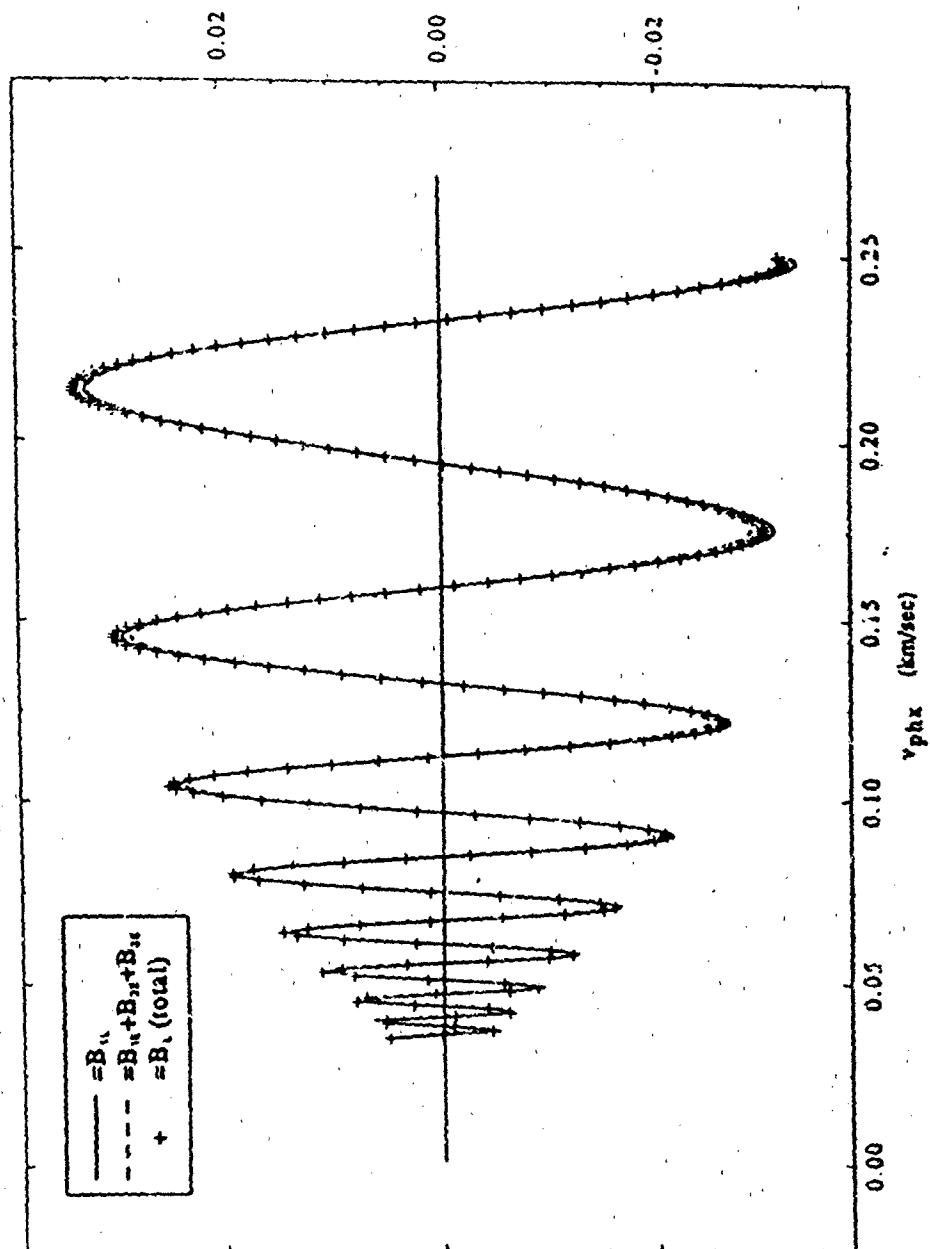


Figure 4 - The same as in Figure 3, but at a fixed time and over a range of horizontal phase trace speeds. The vertical scale is given in arbitrary units.

PART B:

**Perturbation Treatment of the Nonlinear Response of
Minor Atmospheric Species to Linear Gravity Waves**

J. R. Isler⁺, T. F. Tuan, and F. He

Physics Department

University of Cincinnati, Cincinnati, OH 45221

R. H. Picard

Optical Environment Division (OPS)

Geophysics Directorate, Phillips Laboratory

Hanscom AFB, Bedford, MA 01731

February 1991

**+Present Address: Geophysical Institute
University of Alaska, Fairbanks, AK 99775**

Abstract

The local fluctuations of a minor atmospheric species concentration caused by linear gravity wave motions can be nonlinear if the minor species density gradient is sufficiently steep. To treat such a case, a method is outlined by which it is possible to calculate the minor species response to any order in the linear gravity wave. Calculations to third order over a wide range of wave parameters show that the nonlinear effects can be substantial. As a result, care must be taken when analysing data from minor species fluctuations, so that frequencies due solely to the nonlinear nature of the minor species response are not attributed to gravity waves.

1. Introduction

The study of gravity waves in the middle and upper atmosphere has relied from its beginning upon the detection of the motion of minor atmospheric constituents. Early examples include deformations of meteor trails and radio echoes from ionospheric layers, while more recently many observations have been made of airglow intensity fluctuations and resonance lidar backscatter fluctuations.

Many of the minor constituents of the atmosphere are distributed in layers which are sharply peaked. The atomic sodium layer, for example, is concentrated around 90 km in a layer which has on average a half-width much less than the atmospheric scale height. Because of such background structures, small-amplitude (i.e. linear) gravity waves can induce local fluctuations of much larger amplitude in a minor species concentration. Modelling the response of minor atmospheric species to gravity wave perturbations has been carried out by many investigators (Thome, 1968; Porter and Tuan, 1974; Chiu and Ching, 1978; Weinstock, 1978; Gardner and Shelton, 1985; Molina et al., 1985; Walterscheid, et al., 1987; Hines and Tarasick, 1987; Hickey, 1988; Tarasick and Shepard, 1989). With the exception of Weinstock (1978) and Gardner and Shelton (1985), previous studies have focused on the linear response. The present work develops a perturbation expansion approach that can be used to model the nonlinear response of neutral minor species to linear gravity waves. The approach taken is Eulerian, so that the method has direct application to measurements made at a fixed height. It is apparent that with the inherent reliance of so many remote sensing technologies (ionosondes, airglow photometers, radars, lidars) on the detection of minor species motions, a clear understanding of the response of minor atmospheric layers to linear gravity waves is essential for

the proper interpretation of such data, particularly when the data are spectrally analysed.

The present paper confines itself to the treatment of the *local* minor species response, as measured at a given height by active instruments such as radars or resonance lidars. A companion paper addresses the minor species response integrated along a line-of-sight, as measured by passive instruments such as ground-based photometers.

Section 2 displays the origin of the nonlinear dynamical response of minor species with sharply peaked profiles. Section 3 develops the perturbation expansion method in general, and in section 4 it is used to calculate higher-order terms in the minor species dynamical response over a broad range of wave parameters as well as for an illustrative specific case. Conclusions are presented in section 5.

2. Dynamical Nonlinearity

Linear gravity wave theory has on the whole been developed for the special case of a homogeneous fluid, where the mean molecular mass is constant and mixing processes overwhelm diffusive separation. This is in general a good approximation below the mesopause; near and above 100 km, however, the mean molecular mass becomes strongly variable with increasing altitude, and at the same time the mean free path is large enough for species to separate diffusively. In the thermosphere, therefore, even for neutral minor species, a proper treatment of the response to gravity wave perturbations must incorporate multi-component fluid effects and have separate momentum equations for each component (Volland, 1969; Mayr et al., 1984). In the present paper, attention is restricted to neutral minor species in the stratosphere and mesosphere. In these regions, where minor species concentrations never exceed 1% of the total atmospheric concentration, one is justified in considering only the continuity equation for the investigation of neutral minor species. This is because the overwhelming majority of minor species collisions are with major-species particles, and one can assume that they have the same velocity as the major species, except possibly for diffusion, which we will consider next.

The Eulerian continuity equation for any minor species is

$$\frac{\partial n}{\partial t} = -\nabla \cdot (n\vec{v}_m) + P - nL \quad (1)$$

where $n(x, y, z, t)$ is the minor species number density, $\vec{v}_m(x, y, z, t)$ is the minor species velocity field, P is the minor species production rate per unit volume, and L is the minor species loss frequency. Since we want our theory to apply to airglow emission as well as active probing, we will take the term *minor species*, in such cases, to mean the particular electronic or vibrational state of the species which is

the source of the airglow. We wish to use this equation to examine the response of a minor species to dynamical perturbations induced by a gravity wave, in particular the nonlinear response to such perturbations.

Other processes which must be considered, in addition to gravity-wave-induced dynamical perturbations, are diffusive processes and chemical (including collisional and radiative) production and loss. Even in the absence of any motion of the atmosphere as a whole, it may be that $\vec{v}_m \neq 0$. This is because any minor species with a layered structure is in diffusive, not hydrostatic, equilibrium, and is therefore continually diffusing from regions of net production to regions of net loss. The vertical diffusive velocity for an isothermal atmosphere is given by (Chamberlain and Hunten, 1987)

$$w_{diff} = -D \left(\frac{1}{n_o} \frac{dn_o}{dz} + \frac{m_n g}{kT} \right) \quad (2)$$

where D is the diffusion coefficient, m_n the molecular mass of the minor species, g is the acceleration due to gravity, k is Boltzmann's constant, and T is the temperature.

If there is pure gravity wave motion (i.e. no prevailing wind) with parcel velocity \vec{v} , so long as $|\vec{v}| \gg |w_{diff}|$, one can set $\vec{v}_m = \vec{v}$. However, for small scale waves it may be that $|\vec{v}| \approx |w_{diff}|$, and even for somewhat larger scale waves the diffusive velocity may be comparable to the gravity wave velocity for an appreciable part of each gravity wave period, as \vec{v} passes through zero twice per cycle.

In addition to this diffusive velocity, perturbations to the production and loss terms induced by the gravity wave motion may be comparable to the other perturbation terms. If this is the case, the effects of chemistry will be as important as dynamical effects in determining minor species density fluctuations. One measure of whether this is so (Walterscheid et al., 1987; Fritts and Thrane, 1989) is if the

diffusion time (or the lifetime of an excited state) is much greater than the wave period, $\tau_{diff(chem)} \gg T$. The range of diffusion times (lifetimes) of minor constituents, from seconds to days (Winick, 1983), encompasses the gamut of gravity wave periods, which are from 5 or 6 minutes up to several hours. Thus, whether or not perturbations to the production chemistry should be incorporated in the solution to equation (1) must be decided on a case by case basis. For example, for the $\text{OH}(\nu^1)$ levels, which are the source of the Meinel bands, $\tau_{chem} \sim 1$ sec, and chemistry must be included. For atomic sodium, on the other hand, $\tau_{diff} > 1$ day, so for this species chemistry may be safely neglected.

Since the focus of this paper is on dynamical effects, we will arbitrarily assume i) $\vec{v}_m = \vec{v}$ to a good approximation, that is $\vec{v}_{diff} = 0$, and ii) perturbations to the production and loss terms are negligible. Under these assumptions, equation (1) becomes

$$\frac{\partial n}{\partial t} = -\nabla \cdot (n\vec{v}), \quad (3)$$

where \vec{v} is a known quantity, and (3) is therefore an uncoupled equation for n only. To simplify the analysis, for the remainder of this paper we shall take this \vec{v} to represent a monochromatic, linear gravity wave with angular frequency ω , horizontal wavenumber k_x , vertical wavenumber k_z , propagating in a windless, isothermal, horizontally stratified atmosphere with components $(u, 0, w)$ in suitably chosen Cartesian coordinates, with x and t dependence given by $\exp i(\omega t - k_x x)$. Such a wave is a solution to the linearized hydrodynamic equations of the major atmospheric species, implying that the major species number density (hereafter denoted by N), is fluctuating with a small amplitude about an unperturbed, background

value. Given this, we can write the relative fluctuation in the major species number density directly from the linearized continuity equation as

$$\frac{N'}{N_0} = \frac{k_z}{\omega} u + \frac{i}{\omega} \frac{\partial w}{\partial z} + \frac{i}{\omega} \frac{1}{N_0} \frac{dN_0}{dz} w \quad (4)$$

where $N'(x, z, t)$ = perturbed part of N and $N_0(z)$ = unperturbed part of N .

This wave will induce a fluctuation in the minor species density (hereafter denoted by n). However, it is important to note that the minor species fluctuation is not necessarily a "wave" in the same sense as the major species fluctuation is a wave. While the latter is a solution to the entire set of linearized, coupled hydrodynamic equations for a fluid, the former is the response of a minor constituent embedded in the fluid to wave-induced perturbations and is the solution to just the uncoupled continuity equation given by (3) for the minor species density n . This is true because the minor species momentum equation is overwhelmingly dominated by the collision term representing momentum transfer from particles of the major species. In a fashion quite analogous to the derivation of equation (4) for the major species, linearizing equation (3) gives the first-order approximation to the minor species response

$$\frac{n'}{n_0} = \frac{k_z}{\omega} u + \frac{i}{\omega} \frac{\partial w}{\partial z} + \frac{i}{\omega} \frac{1}{n_0} \frac{dn_0}{dz} w \quad (5)$$

where $n'(x, z, t)$ = perturbed part of n and $n_0(z)$ = unperturbed part of n .

Two points to consider about the minor species response, evident in the first-order equation (5), are the following. First, for minor species with a layered structure, the unperturbed density gradient is positive in the region below the peak and negative in the region above the peak, while the unperturbed major species gradient is always negative. This implies a shift in the phase difference between the

major and minor species density fluctuations at the point of the minor species peak. Indeed, for a wide range of gravity waves, equations (4) and (5) are dominated by their third terms (Makhlouf, et al., 1987), so that below the peak the first-order minor species response is 180 degrees out of phase with the major species fluctuation, while above the peak it is in phase with the major species. This phase reversal in the region of the profile peak has been known for some time on both theoretical (Thorne, 1968; Porter and Tuan, 1974; Weinstock, 1978) and observational grounds (Thorne, 1968; Noxon, 1978; Shelton et al., 1980).

A second point to consider about equation (5) is its magnitude relative to equation (4). For the case of pure linear gravity wave motion which we are considering, the magnitude of the major species fluctuation, given by equation (4), is by assumption small, say 10% or less. However, when the same velocity field is used in equation (5), the magnitude of the first-order minor species response can be much greater. This result occurs because the advective part of the Eulerian time derivative, which produces the third terms of equations (4) and (5), involves gradients of background densities. As mentioned previously, such gradients can be much larger for minor species than the corresponding major species gradient. Consequently, though equation (4) is by assumption valid for the major species, retaining only first-order terms for the minor species, as in equation (5), is not in general justified. As an explicit example, if one uses the U.S. Standard Atmosphere (USSA) 1976 model of atomic oxygen, at 90 km (just below the O peak at 97 km) a gravity wave which corresponds to a 10% density fluctuation in the major species will induce a 40% first-order fluctuation in the atomic oxygen density. Thus dynamical nonlinearities enter naturally into the minor species response. In the next section, a method is developed to treat these dynamical nonlinearities.

3. Perturbation Expansion Method

To calculate higher-order solutions to equation (3), we begin by rewriting it (Isler, et al., 1988) as

$$\frac{\partial \psi}{\partial t} = \lambda Q \frac{\partial \psi}{\partial x} + \lambda R \frac{\partial \psi}{\partial z} + \lambda S \psi + \lambda S \quad (6)$$

where

$$\psi \equiv n'/n_o,$$

$$Q = -u,$$

$$R = -w,$$

$$S = -\left(\frac{\partial u}{\partial x} + \frac{\partial w}{\partial z} + \frac{1}{n_o} \frac{dn_o}{dz} w\right),$$

and we have simply used

$$\frac{d}{dz} \psi = \frac{1}{n_o} \frac{dn'}{dz} - \frac{n'}{n_o^2} \frac{dn_o}{dz}$$

in rewriting equation (3). Note that we have rewritten the exact equation (3), retaining all orders in the wave velocity \bar{v} . A dimensionless parameter, λ , has been introduced as a bookkeeping device to keep track of orders in \bar{v} , or equivalently of orders in N'/N_o , since u and w are linearly related to N'/N_o . Next, we write

$$\psi = \lambda \psi_1 + \lambda^2 \psi_2 + \lambda^3 \psi_3 + \dots \quad (7)$$

where ψ_1 is linear in N'/N_o , ψ_2 is quadratic in N'/N_o , etc.. Inserting this expansion into equation (6), we can proceed to solve for the minor species response to a linear gravity wave to any order in λ , that is in N'/N_o .

To first order in λ , equation (6) is $\partial \psi_1 / \partial t = S$, and so

$$\psi_1 = - \int_{t_o}^t \left(\frac{\partial u}{\partial x} + \frac{\partial w}{\partial z} + \frac{1}{n_o} \frac{dn_o}{dz} w \right) dt'. \quad (8)$$

Since we are interested in fluctuations at some time t long after the gravity wave has settled into its monochromatic state, we take the initial time in equation (8), $t = t_0$, to be a time before gravity wave motion begins, when $\bar{v} = 0$. We assume that the transient state develops smoothly and continuously into a monochromatic state. As it should be, ψ_1 obtained in this way is equivalent to equation (5). Using the above notation, $\psi_1 = Re - iS/\omega$.

When calculating higher-order solutions to equation (6), it must be remembered that the real parts of complex quantities must be taken prior to any multiplication; otherwise, difference-frequency effects can be missed altogether. Thus, to second order in λ , equation (6) is given by

$$\frac{\partial \psi_2}{\partial t} = ReQ Re \frac{\partial \psi_1}{\partial x} + ReR Re \frac{\partial \psi_1}{\partial z} + ReS Re \psi_1 \quad (9)$$

which can be solved since ψ_1 is known. Once again, the integration is chosen to be from a time prior to the gravity wave motion.

In general, at the n th order, we have the recursion relation

$$\frac{\partial \psi_n}{\partial t} = ReQ Re \frac{\partial \psi_{n-1}}{\partial x} + ReR Re \frac{\partial \psi_{n-1}}{\partial z} + ReS Re \psi_{n-1}. \quad (10)$$

In this way, one can obtain ψ , the minor species response, to any order in the linear gravity wave parameters.

Gardner and Shelton (1985) devised a similar perturbation expansion approach; they too neglected production and loss perturbations and diffusion, and began, as we have done, from equation (3). However, their approach assumed a form for the solution in advance, and they considered only large period gravity waves, while the approach taken here is more general.

It may be suggested that to be consistent, one would have to retain all n th order terms, and so in equation (6) put in for \bar{v} the expansion

$$\bar{v} = \lambda \bar{v}_1 + \lambda^2 \bar{v}_2 + \lambda^3 \bar{v}_3 + \dots \quad (11)$$

These higher orders in \bar{v} would be the result of retaining higher orders in the solutions to the coupled hydrodynamic equations of the major species, i.e. incorporating nonlinear gravity wave effects. However, we have assumed that the minor species fluctuations are due to perturbation by a linear gravity wave, that is $\bar{v} = \bar{v}_1$ to a good approximation, so we further assume that any contributions to the minor species response due to higher-order corrections to \bar{v} are negligible relative to those due to the linear \bar{v} alone. This was also implicitly assumed by Gardner and Shelton (1985).

4. Results

We have calculated the minor species response to third order in the linear gravity wave for several different background profiles and over a wide range of gravity wave parameters. As one would expect, the importance of the higher-order terms in the response depends strongly upon the steepness of the vertical density gradient of the minor species. Specifically, we have used various Chapman function and Gaussian analytic models, and the USSA 1976 model of atomic oxygen as well. Figures 1a-1c show the profiles used in obtaining the subsequent plots: namely, a Chapman function, a Gaussian distribution, and the USSA 1976 atomic oxygen model. For easy comparison, the two analytic profiles have each been set to peak at 92 km.

We have considered two gravity wave models. The first is a free travelling wave in an infinite isothermal atmosphere (Hines, 1960), with velocity components

$$u = A\omega k_z c^2 (k_z + i\eta) e^{z/2H} e^{i(\omega t - k_x x - k_z z)} \quad (12)$$

$$w = A\omega(\omega^2 - k_z^2 c^2) e^{z/2H} e^{i(\omega t - k_x x - k_z z)} \quad (13)$$

where H is the atmospheric scale height, c is the speed of sound, A is an amplitude factor, and $\eta = -(1 - \gamma/2)g/c^2$, with γ the ratio of specific heats. The second is a vertically stationary wave in a semi-infinite atmosphere with a rigid surface ground boundary, having velocity components

$$v = \frac{\alpha k_x k_z}{\omega^2} \left(\cos k_z z + \frac{\eta}{k_z} \sin k_z z \right) e^{z/2H} e^{i(\omega t - k_x x)} \quad (14)$$

$$w = i\alpha \sin k_z z \left(\frac{k_z^2 + \eta^2}{\omega_b^2 - \omega^2} \right) e^{z/2H} e^{i(\omega t - k_x x)} \quad (15)$$

where ω_b is the Brunt-Vaisala frequency and α is another amplitude factor. Such waves come from either a high altitude source, or a once-reflected wave from a low

altitude source, or a guided mode; in general, an arbitrary gravity wave is a linear combination of (12), (13) and (14), (15). The detailed algebra leading to ψ_2 and ψ_3 for each case will not be presented here.

The stability of the perturbation method outlined above is dependent upon the type of gravity wave model used; in particular, secularity (divergence in time) is present in the response to the travelling wave, but is absent in the response to the vertically stationary wave. The absence of secularity in the latter case is due to the fact that the horizontal and vertical velocity fields are 90° out of phase, so that at the second order the time integral contains a pure elliptically polarized sinusoid. For the travelling wave, on the other hand, the time integral contains an offset sinusoid, and secularity results. It is interesting to note that the growth rate of the instability is proportional to

$$\left(1 - \frac{\omega^2}{k_z^2 c^2}\right) \left(\frac{1}{H} + \frac{1}{n_0} \frac{dn_0}{dz}\right). \quad (16)$$

Thus, i) the instability disappears if the minor species density falls off with the atmospheric scale height, and ii) the instability is more pronounced for small-scale waves ($\omega \ll k_z c$) than for larger-scale waves, as one would expect, since the relative importance of vertical motion is greater for the former than for the latter, and it is vertical motion which produces the nonlinear response. To correct for the secularity, we are investigating the use of renormalization schemes which would ultimately lead to a solution containing non-integer multiples of the gravity wave frequency. To avoid the secularity, for the present paper we have restricted attention to the vertically stationary wave model (it is this model which has been used in the Figures 2-5); however, the relative magnitudes of the higher-order terms are comparable in the two cases, so that the results would not be greatly altered had we used a renormalized solution for the vertically travelling wave model.

To ensure the linearity of the gravity wave, the envelope of the amplitude of the vertically stationary velocity field has been normalized to induce at most a 15% major species density fluctuation at the profile peak. In the case of the wave used in Figures 2-4, this results in an actual major species density fluctuation of only 5% in the major species density at the profile peak.

The gravity wave used in Figures 2-4 has a horizontal phase trace speed of 150 m/s, an intrinsic period of 2 hrs, a horizontal wavelength of 1080 km, and a vertical wavelength of 55 km. The results for this particular gravity wave are not unique, and we have used it solely for illustrative purposes. In all three figures, we have plotted the major species density fluctuation, the first-order minor species response, and the sum of the first three orders in the minor species response.

In Figure 2, the background minor species profile is that of Figure 1a. Figure 2a shows the response at 87 km, where the background density is orders of magnitude below its peak value. The first-order response here is greater than 400% (the major species fluctuation is barely visible on this scale). As a result, the nonlinear response is overwhelming. In Figure 2b, the response at 89 km is shown. The nonlinear response at this height remains considerable, and is responsible for the cusp effect of sharpening the waveform peak and flattening the waveform trough. In Figure 2c, the response at 95 km is shown. At this height, the response is for the most part linear.

In Figure 3, the background minor species profile is that of Figure 1b. Figures 3a, 3b and 3c show the response at 87 km, 89 km and 95 km, respectively. The nonlinear effects for this profile are not as pronounced as they were in the previous figure, but they are noticeable nonetheless. The cusping of the waveform is evident at 87 km. Also noticeable is the phase reversal of the response at the profile peak.

The response is 180 degrees out of phase with the major species fluctuation below the profile peak, and in phase above the peak.

In Figure 4, the background profile is that of Figure 1c. Figures 4a, 4b and 4c show the response at 89 km, 92 km and 102 km, respectively. Even for this relatively broad profile, there is a noticeable cusp effect at certain height levels.

Figure 5 serves to show the importance of higher-order effects over a broad range of wave parameters for the response at 89 km, using the profile of Figure 1a. In Figure 5a, we have plotted the first, second and third-order response as a function of time for a gravity wave with a horizontal phase trace speed of 150 m/s and an intrinsic period of 2 hrs. It is the sum of these which appears in large dashes in Figure 2b. In Figure 5b we have plotted the first, second and third-order response at a fixed time as a function of horizontal phase trace speed (v_{phz}) from 35 m/s up to 250 m/s for an intrinsic period of 2 hrs. Oscillations occur over the range of phase speeds because of the vertically stationary gravity wave model we employ. Figure 5c is the same as Figure 5b, except the intrinsic period is now 20 min. We should point out that it is unlikely that smaller-scale waves (phase speeds less than 50 m/s, say) will reach the amplitude necessary to induce even a 10% major species fluctuation before becoming unstable or encountering a critical level, and so smaller-scale waves should not be expected to produce a significant nonlinear response. However, it is clear that the significance of the higher-order terms is not sensitive to the particular gravity wave parameters.

The above results demonstrate the significance of the nonlinear response for minor atmospheric constituents which are distributed in narrow layers. For example, there can be a substantial cusp effect in the response at certain height levels. As a consequence, it is to be expected that the spectra obtained from minor species

fluctuations at particular height levels can contain peaks not only at frequencies associated with the actual gravity wave field, but at integer-multiple harmonics of the gravity wave frequencies as well.

5. Conclusions

We have outlined a method which can be used to calculate higher-order, non-linear terms in the local response of minor atmospheric species to linear gravity waves. The method results in an expansion of the minor species response to any order in the linear gravity wave. Due to secular terms arising when the method is applied to vertically travelling waves, for the present we have therefore only considered the case of vertically stationary waves. Higher-order effects have been shown to be important over a broad range of wave parameters. Consequently, particular care must be taken in inferring from the power spectra of minor species fluctuations the wave field of the atmosphere as a whole. In future work we intend to extend the method to treat charged minor species and incorporate the effects of perturbations to the production and loss chemistry.

Acknowledgements

This work was supported in part by the Air Force Office of Scientific Research and the Geophysics Directorate, Phillips Laboratory, under contract F19628-87-K-0023. The work was associated with the ARC/AARC Airglow Modeling and MAPSTAR programs. In addition, support was provided by the Air Force Office of Scientific Research (AFSC) under contract AFOSR-91-0026 and by the SDIO/IST and managed by the Office of Naval Research under contract N00014-J-1271.

Bibliography

- [1] Chamberlain, J. W. and D. M. Hunten (1987). *Theory of Planetary Atmospheres*. Academic Press.
- [2] Chui, Y. T. and B. K. Ching (1978). *Geophys. Res. Lett.*, **5**, 539.
- [3] Gardner, C. S., J. D. Shelton and C. F. Sechrist (1980). *Geophys. Res. Lett.*, **7**, 1069.
- [4] Gardner, C. S. and J. D. Shelton (1985). *J. Geophys. Res.*, **90**, 1745.
- [5] Hatfield, R., T. F. Tuan and S. M. Silverman (1981). *J. Geophys. Res.*, **86**, 2429.
- [6] Hickey, M. (1988). *J. Geophys. Res.*, **93**, 4077.
- [7] Hines, C. O. (1960). *Can. J. Phys.*, **38**, 1441.
- [8] Isler, J. R., T. F. Tuan, U. Makhlof, R. H. Picard and P. L. Lin (1988). *EOS*, **69**, 44, 1342.
- [9] Isler, J. R., T. F. Tuan and R. H. Picard (1991). *J. Geophys. Res.*, **11**, .
- [10] Makhlof, U., D. Y. Wang, J. J. Lin and T. F. Tuan (1987). *EOS*, **68**, 44, 1394.
- [11] Mayr, H. G., I. Harris, F. Varosi and F. A. Herrero (1984). *J. Geophys. Res.*, **89**, 10,929.
- [12] Molina, A. (1986). *J. Atmos. Sci.*, **40**, 2444.
- [13] Noxon, J. F. (1978). *Geophys. Res. Lett.*, **5**, 25.
- [14] Porter, H. S., S. M. Silverman and T. F. Tuan (1974). *J. Geophys. Res.*, **79**, 3827.
- [15] Thome, G. (1968). *J. Geophys. Res.*, **73**, 6319.
- [16] U.S. Standard Atmosphere (1976). U.S. Government Printing Office, Washington, D.C.
- [17] Volland, H. (1969). *J. Atmos. Terr. Phys.*, **31**, 491.

- [13] Walterscheid, R. L., G. Schubert and J. M. Straus (1987). *J. Geophys. Res.*,
92, 1241.
- [19] Weinstock, J. (1978). *J. Geophys. Res.*, 83, 5175.
- [20] Winick, J. R. (1983). *Solar-Terrestrial Physics*, edited by J. M. Forbes and
R. L. Carovillano, D. Reidel Publishing Company.

Figure Captions

Figure 1. (a) Chapman function used in Figures 2 and 5. (b) Gaussian distribution used Figure 3. (c) USSA atomic oxygen model, used in Figure 4.

Figure 2. (a) First-order major species fluctuation (solid line), first-order minor species response (large dashes), and the sum of the first three orders of the minor species response (small dashes), at 87 km, for a gravity wave with an intrinsic period of 2 hrs and a horizontal phase trace speed of 150 m/s. The minor species profile is that of Figure 1a. (b) Same as (a), but at 89 km. (c) Same as (a), but at 95 km.

Figure 3. (a) First-order major species fluctuation (solid line), first-order minor species response (large dashes), and the sum of the first three orders of the minor species response (small dashes), at 87 km, for a gravity wave with an intrinsic period of 2 hrs and a horizontal phase trace speed of 150 m/s. The minor species profile is that of Figure 1b. (b) Same as (a), but at 89 km. (c) Same as (a), but at 95 km.

Figure 4. (a) First-order major species fluctuation (solid line), first-order minor species response (large dashes), and the sum of the first three orders of the minor species response (small dashes), at 89 km, for a gravity wave with an intrinsic period of 2 hrs and a horizontal phase trace speed of 150 m/s. The minor species profile is that of Figure 1c. (b) Same as (a), but at 92 km. (c) Same as (a), but at 102 km.

Figure 5. (a) First-order minor species response (solid line), second-order minor species response (large dashes), and third-order minor species response (small dashes), at 89 km, for a gravity wave with an intrinsic period of 2 hrs and a horizontal phase trace speed of 150 m/s. The minor species profile is that of Figure 1a.

(b) Same as (a), but at a fixed time as a function of horizontal phase trace speed (v_{phz}), for a gravity wave with an intrinsic period of 2 hrs. (c) Same as (b), but for a gravity wave with a period of 20 min.

Figure 1a

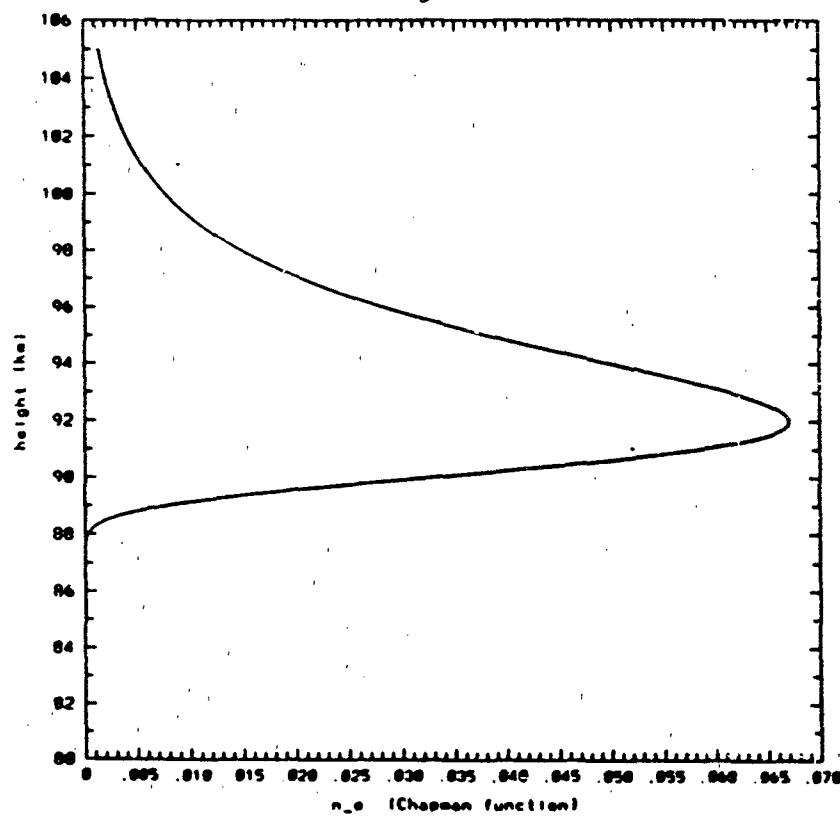


Figure 1. (a) - Chapman function used in Figures and and 5. (b) Gaussian distribution used in Figure 3. (c) USSA atomic oxygen model, used in Figure 4.

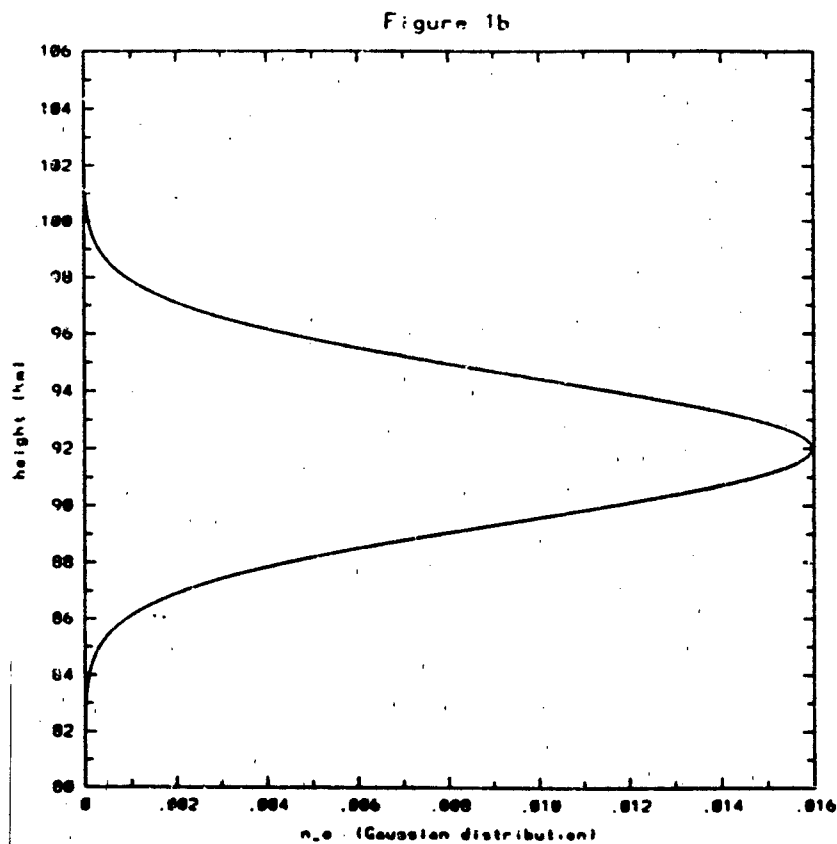


Figure 1. (a) - Chapman function used in Figures and and 5. (b) Gaussian distribution used in Figure 3. (c) USSA atomic oxygen model, used in Figure 4.

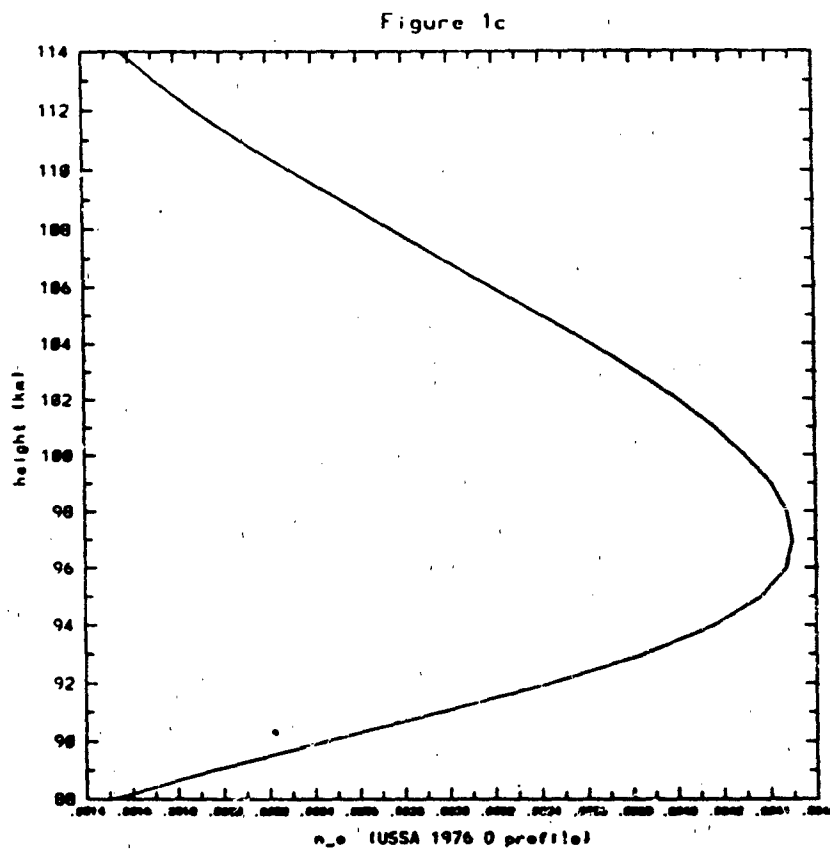


Figure 1. (a) - Chapman function used in Figures and and 5. (b) Gaussian distribution used in Figure 3. (c) USSA atomic oxygen model, used in Figure 4.

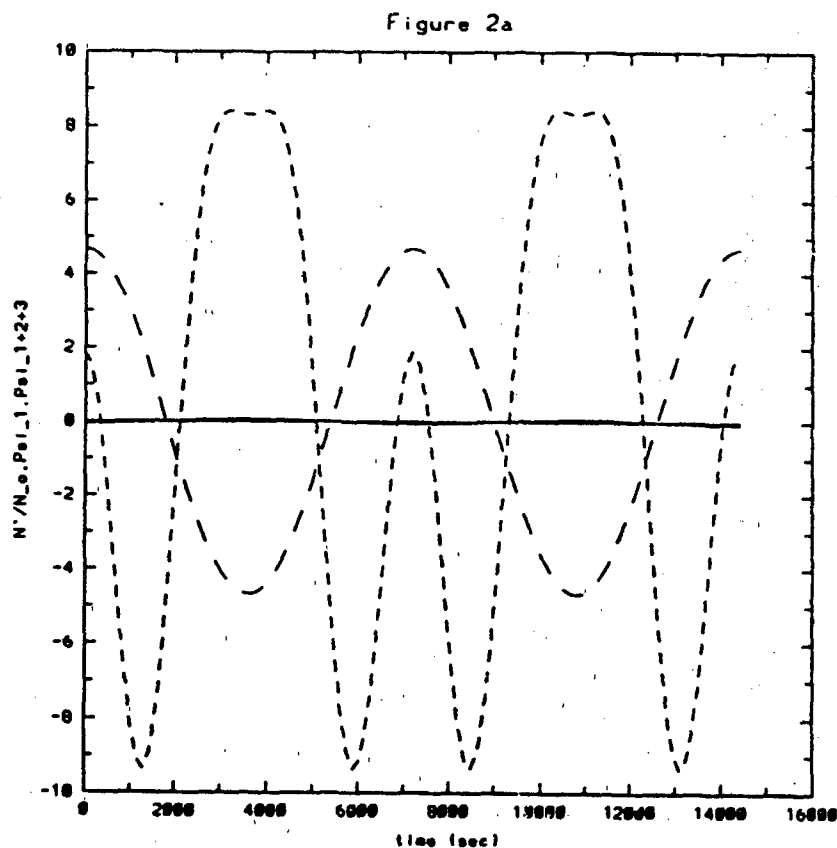


Figure 2. (a) First-order major species fluctuation (solid line), first-order minor species response (large dashes), and the sum of the first three orders of the minor species response (small dashes), at 87 km, for a gravity wave with an intrinsic period of 2 hours and a horizontal phase trace speed of 150 m/s. The minor species profile is that of Figure 1a. (b) Same as (a), but at 89 km. (c) Same as (a), but at 95 km.

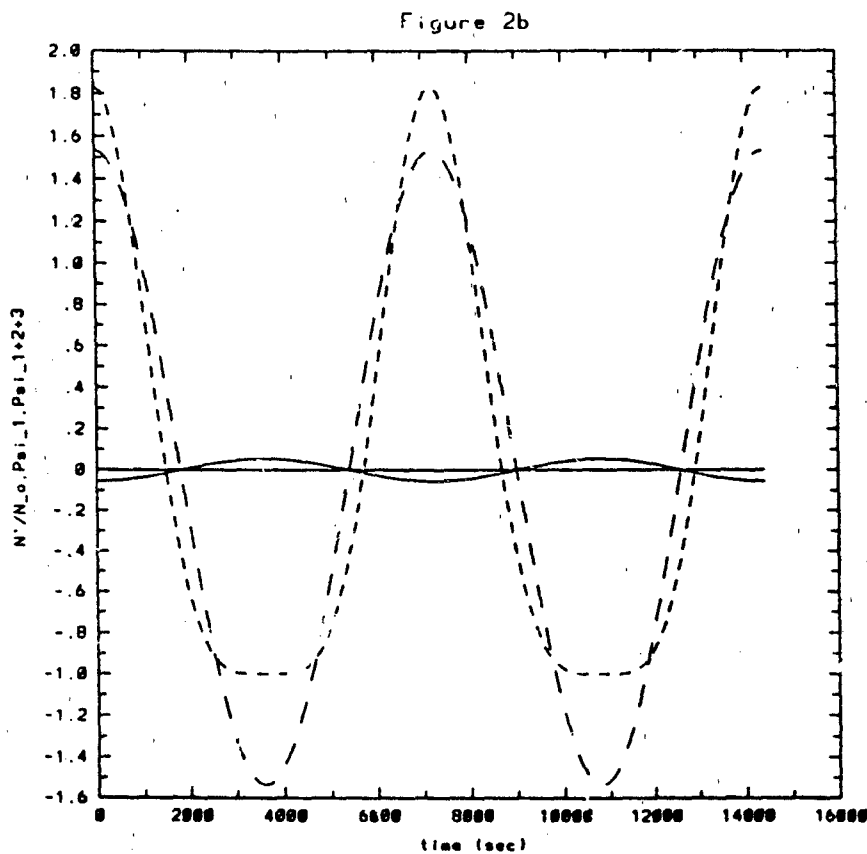


Figure 2. (a) First-order major species fluctuation (solid line), first-order minor species response (large dashes), and the sum of the first three orders of the minor species response (small dashes), at 87 km, for a gravity wave with an intrinsic period of 2 hours and a horizontal phase trace speed of 150 m/s. The minor species profile is that of Figure 1a. (b) Same as (a), but at 89 km. (c) Same as (a), but at 95 km.

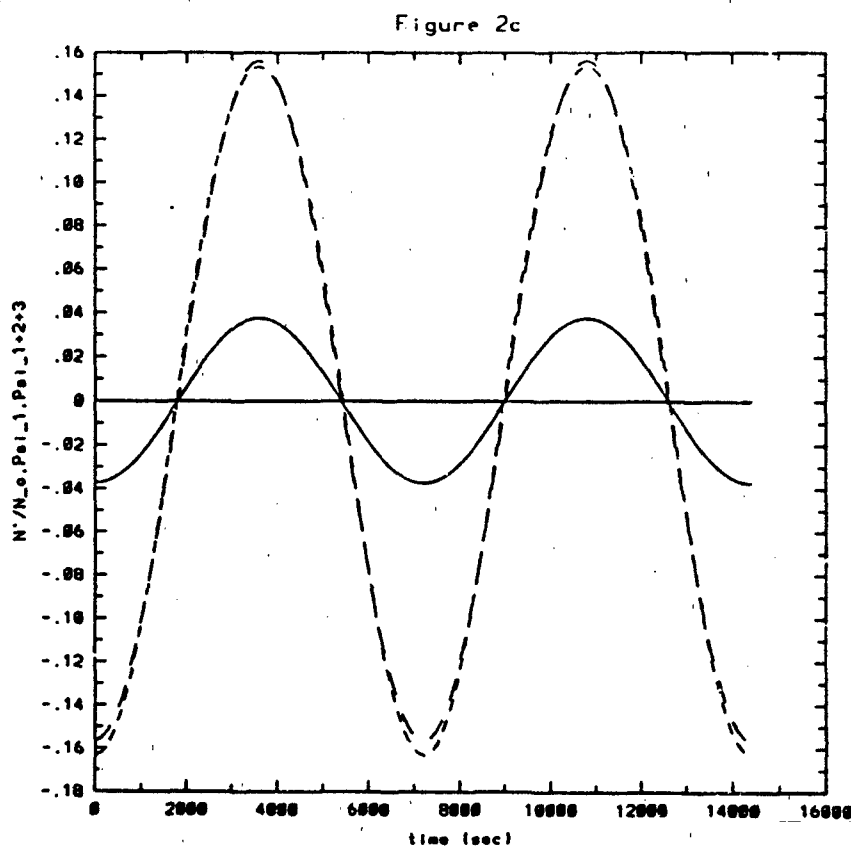


Figure 2. (a) First-order major species fluctuation (solid line), first-order minor species response (large dashes), and the sum of the first three orders of the minor species response (small dashes), at 87 km, for a gravity wave with an intrinsic period of 2 hrs and a horizontal phase trace speed of 150 m/s. The minor species profile is that of Figure 1a. (b) Same as (a), but at 89 km. (c) Same as (a), but at 95 km.

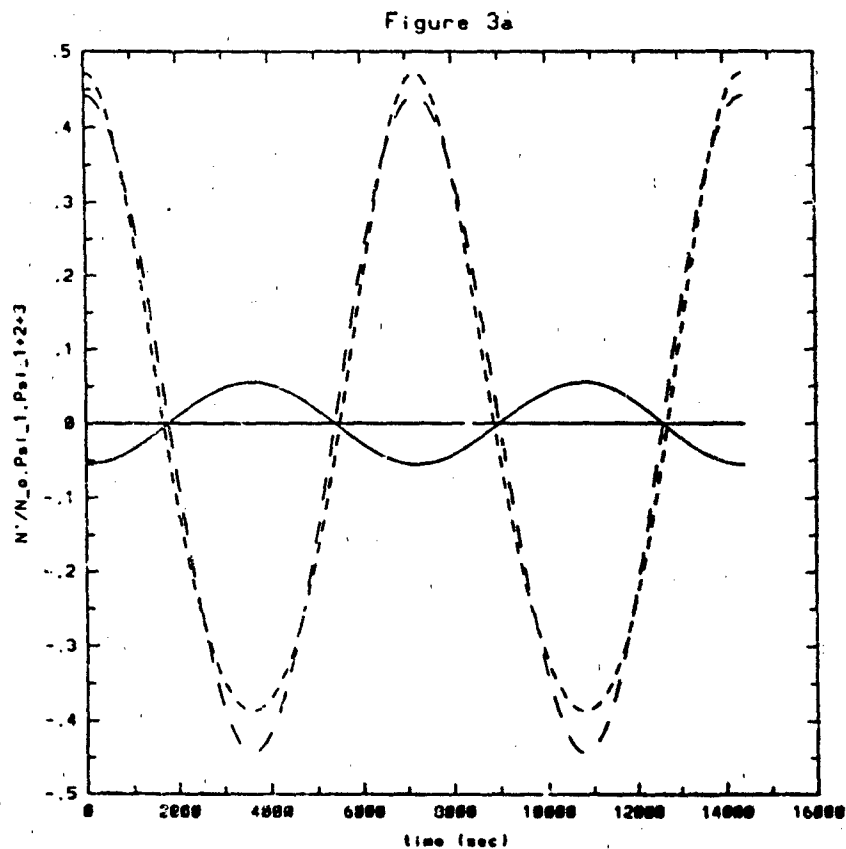


Figure 3. (a) First-order major species fluctuation (solid line), first-order minor species response (large dashes), and the sum of the first three orders of the minor species response (small dashes), at 87 km, for a gravity wave with an intrinsic period of 2 hrs and a horizontal phase trace speed of 150 m/s. The minor species profile is that of Figure 1b. (b) Same as (a), but at 89 km. (c) Same as (a), but at 95 km.

Figure 3b

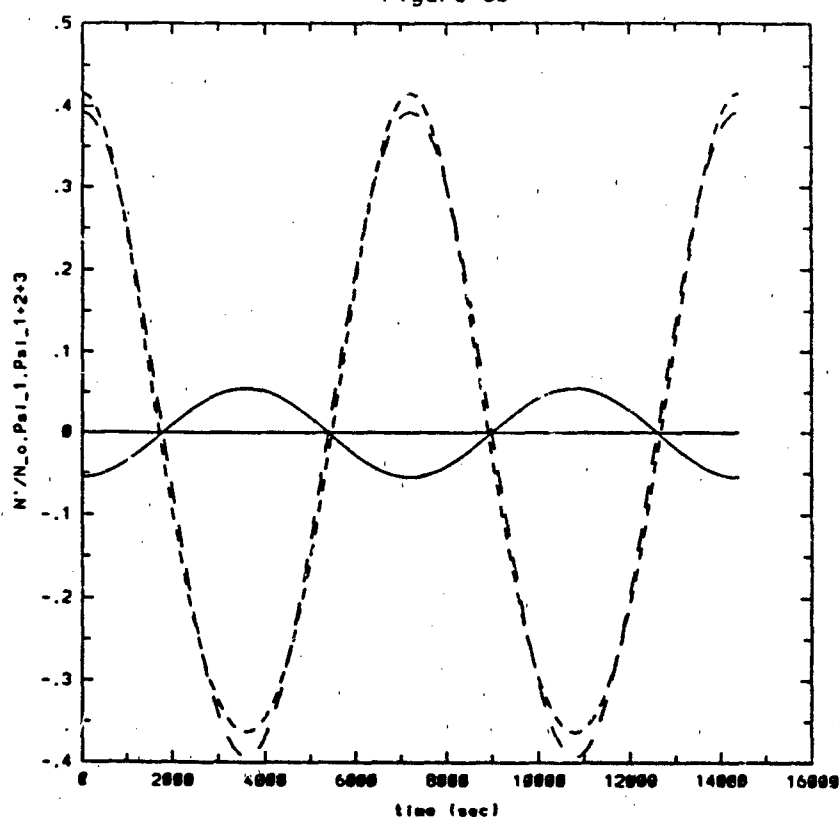


Figure 3. (a) First-order major species fluctuation (solid line), first-order minor species response (large dashes), and the sum of the first three orders of the minor species response (small dashes), at 87 km, for a gravity wave with an intrinsic period of 2 hrs and a horizontal phase trace speed of 150 m/s. The minor species profile is that of Figure 1b. (b) Same as (a), but at 89 km. (c) Same as (a), but at 95 km.

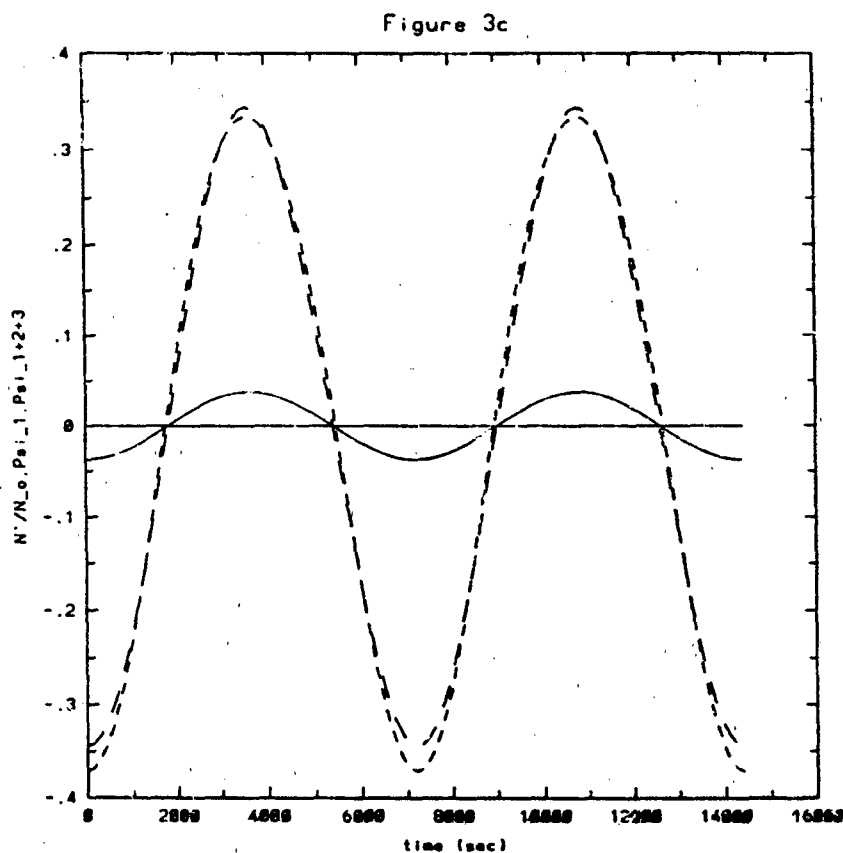


Figure 3. (a) First-order major species fluctuation (solid line), first-order minor species response (large dashes), and the sum of the first three orders of the minor species response (small dashes), at 87 km, for a gravity wave with an intrinsic period of 2 hrs and a horizontal phase trace speed of 150 m/s. The minor species profile is that of Figure 1b. (b) Same as (a), but at 89 km. (c) Same as (a), but at 95 km.

Figure 4a

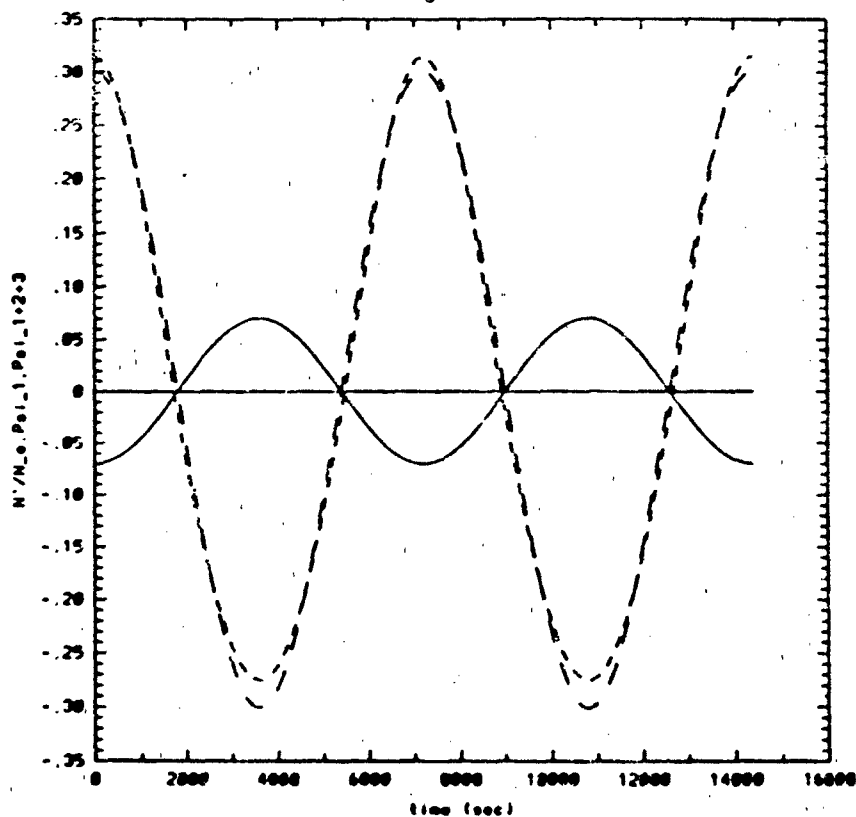


Figure-4. (a) First-order major species fluctuation (solid line), first-order minor species response (large dashes), and the sum of the first three orders of the minor species response (small dashes), at 89 km, for a gravity wave with an intrinsic period of 2 hrs and a horizontal phase trace speed of 150 m/s. The minor species profile is that of Figure 1c. (b) Same as (a), but at 92 km. (c) Same as (a), but at 102 km.

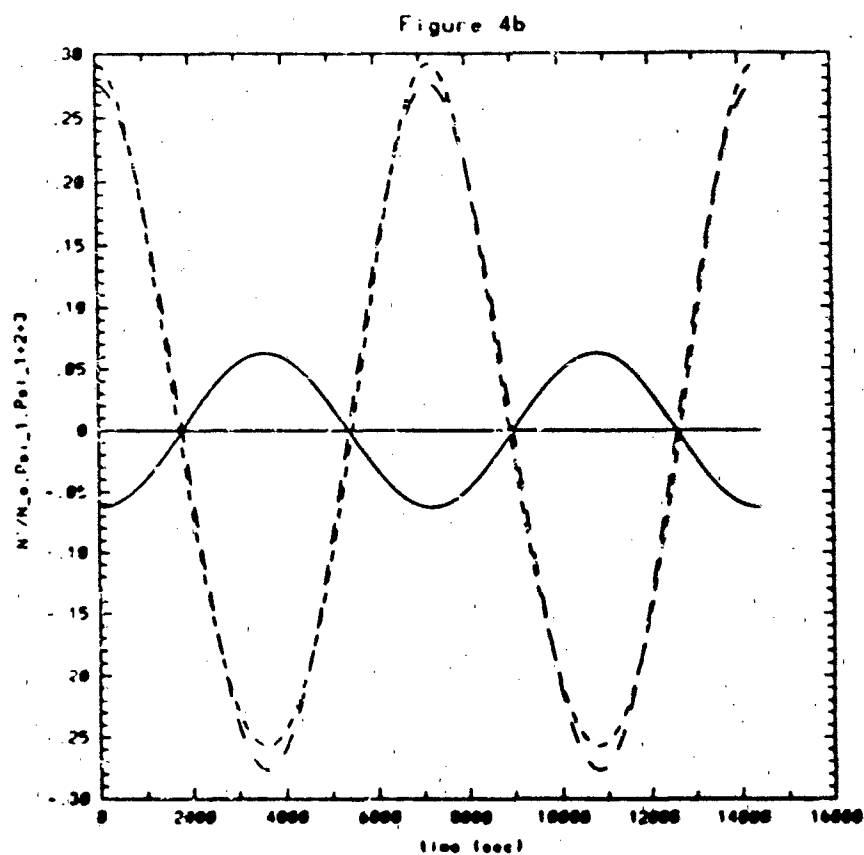


Figure 4. (a) First-order major species fluctuation (solid line), first-order minor species response (large dashes), and the sum of the first three orders of the minor species response (small dashes), at 89 km, for a gravity wave with an intrinsic period of 2 hrs and a horizontal phase trace speed of 150 m/s. The minor species profile is that of Figure 1c. (b) Same as (a), but at 92 km. (c) Same as (a), but at 102 km.

Figure 4c

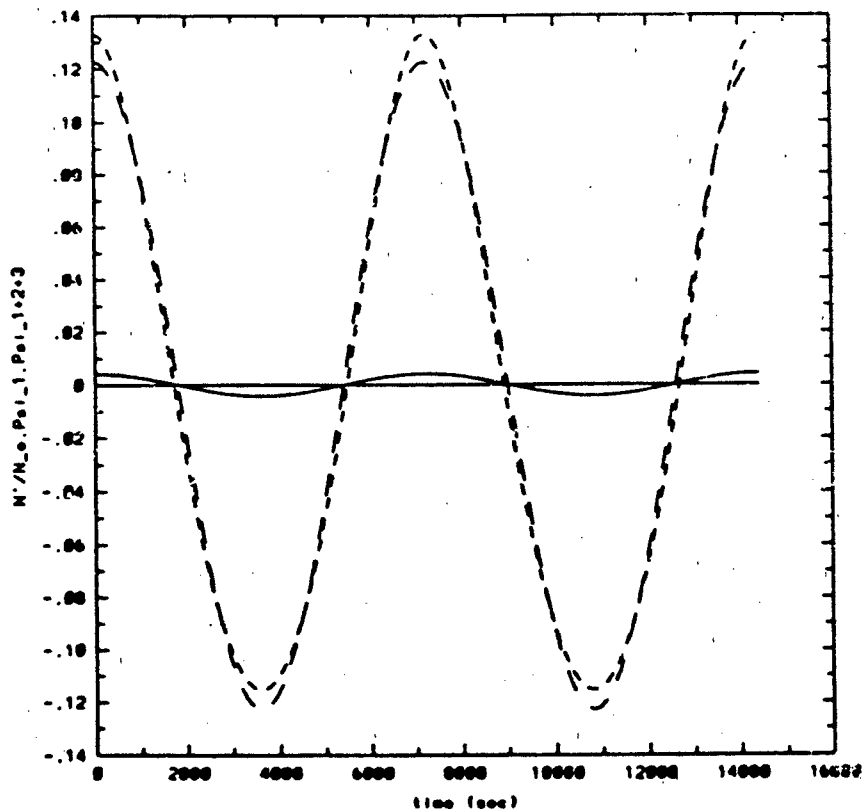


Figure 4. (a) First-order major species fluctuation (solid line), first-order minor species response (large dashes), and the sum of the first three orders of the minor species response (small dashes), at 89 km, for a gravity wave with an intrinsic period of 2 hrs and a horizontal phase trace speed of 150 m/s. The minor species profile is that of Figure 1c. (b) Same as (a), but at 92 km. (c) Same as (a), but at 102 km.

Figure 5a

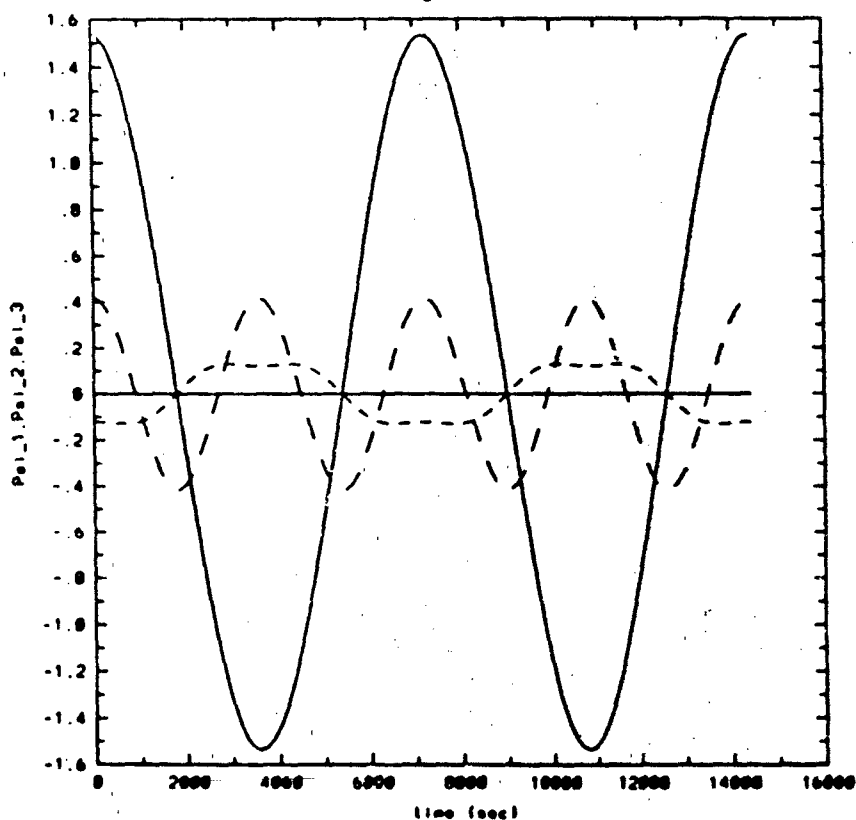


Figure 5. (a) First-order minor species response (solid line), second-order minor species response (large dashes), and third-order minor species response (small dashes), at 89 km, for a gravity wave with an intrinsic period of 2 hrs and a horizontal phase trace speed of 150 m/s. The minor species profile is that of Figure 1a. (b) Same as (a), but at a fixed time as a function of horizontal phase trace speed (v_{phx}), for a gravity wave with an intrinsic period of 2 hrs. (c) Same as (b), but for a gravity wave with a period of 20 min.

Figure 5b

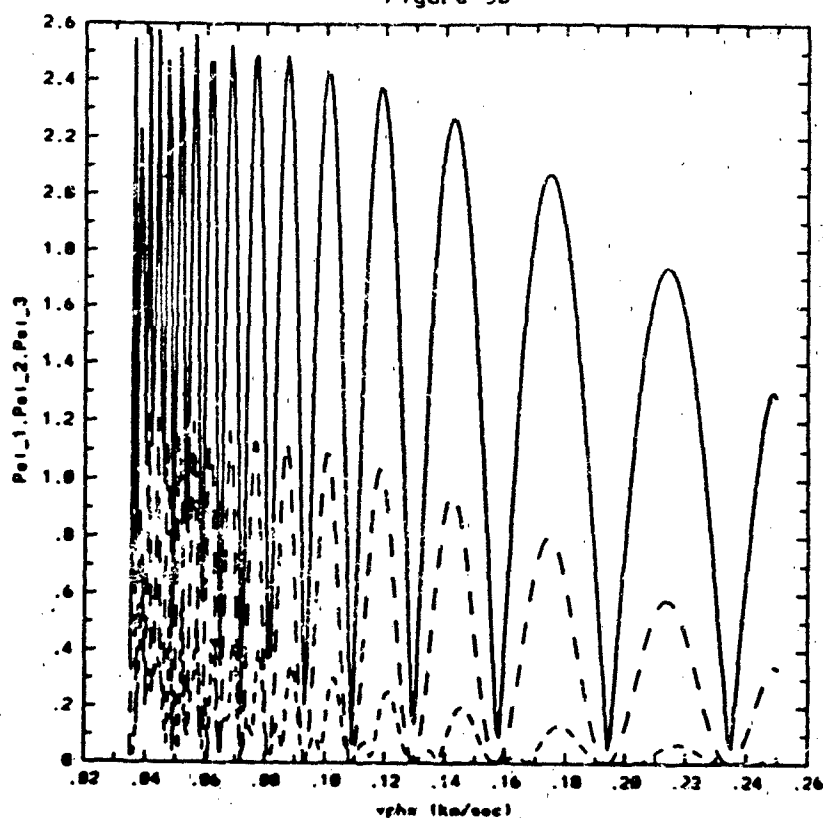


Figure 5. (a) First-order minor species response (solid line), second-order minor species response (large dashes), and third-order minor species response (small dashes), at 89 km, for a gravity wave with an intrinsic period of 2 hrs and a horizontal phase trace speed of 150 m/s. The minor species profile is that of Figure 1a. (b) Same as (a), but at a fixed time as a function of horizontal phase trace speed (v_{phx}), for a gravity wave with an intrinsic period of 2 hrs. (c) Same as (b), but for a gravity wave with a period of 20 min.

Figure 5c

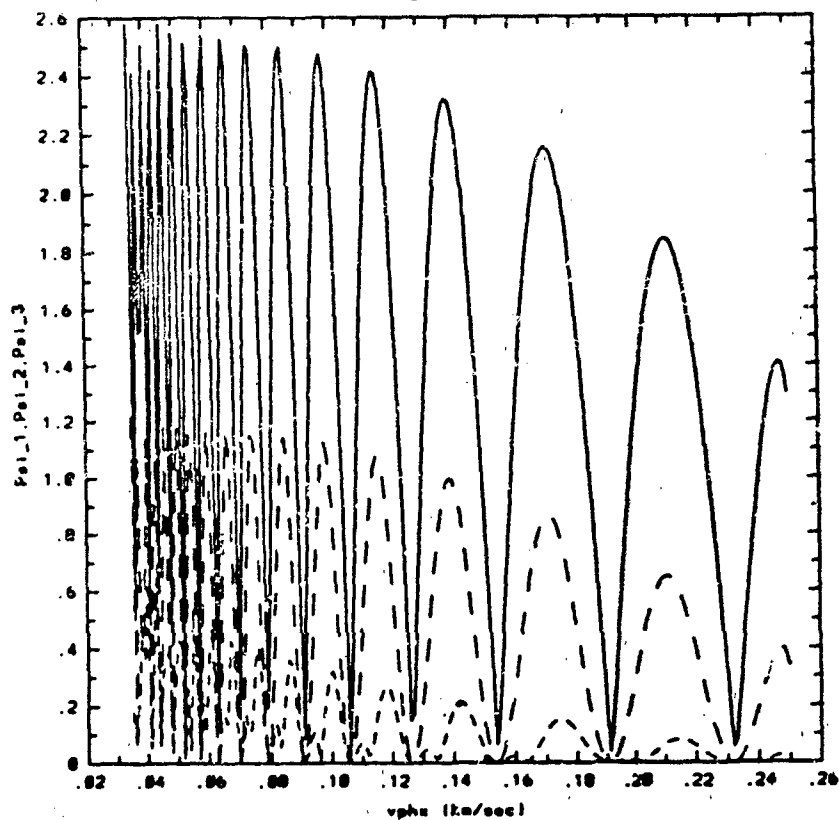


Figure 5. (a) First-order minor species response (solid line), second-order minor species response (large dashes), and third-order minor species response (small dashes), at 89 km, for a gravity wave with an intrinsic period of 2 hrs and a horizontal phase trace speed of 150 m/s. The minor species profile is that of Figure 1a. (b) Same as (a), but at a fixed time as a function of horizontal phase trace speed (v_{phx}), for a gravity wave with an intrinsic period of 2 hrs. (c) Same as (b), but for a gravity wave with a period of 20 min.

IV. MEASUREMENTS OF OH AIRGLOW WAVE STRUCTURES

**FINAL REPORT
on
Subcontract between
The University of Southampton, and
The University of Cincinnati**

**by
M. J. Taylor**

**Department of Physics
University of Southampton
Southampton, SO9 5NH, U.K.**

**This contract was issued as part of
The US Airforce Contract F19628-87-K-0023 to
The University of Cincinnati for research under the
project entitled "Investigations in Atmospheric Dynamics".**

4 June 1991

FINAL REPORT

Submitted by: M.J. Taylor
Department of Physics,
University of Southampton,
Southampton, SO9 5NH, U.K.

Period covered: 3 May 1990 to 4 April 1991.

1. This report covers the extension (Modification No 1) of the subcontract between the University of Southampton and the University of Cincinnati issued as part of the US Airforce Contract F19628-87-K-0023 to UC for research under the project entitled "Investigations in Atmospheric Dynamics".

2. The primary aim of this research contract was to image wave structure in the OH nightglow emission to determine the frequency of occurrence, geographical location, horizontal wavelength, horizontal velocity (and hence apparent period) of short period (<1 hour) mesospheric gravity waves present over an ocean site. The measurements were successfully made in late March and early April, 1990 from Maui, Hawaii as part of the ALOHA-90 campaign.

3. Due to the success of the ALOHA campaign it was decided, at short notice, to leave the cameras set up on Haleakala and to make a second set of measurements during the following new moon period 18-28 April. All three cameras continued to function well and excellent data were obtained for comparison with the first set of measurements. The additional funding awarded in Modification No 1 of this subcontract have been used towards the costs incurred during this second set of measurements and to cover the initial data analysis.

4. In progress report No 1 (submitted 22 June 1990) details of the instrumentation were given together with a summary of the measurements. An introduction to the image data was also presented at the first ALOHA workshop which was held during the CEDAR meeting, Boulder, in June 1990.

5. The analysis of both data sets has progressed well. The first detailed results were presented at the ALOHA session of the AGU meeting, held in San Francisco, December 1990. During this meeting it was decided to concentrate on two nights 25 and 31 March so that the image data could be compared with the measurements obtained by the other instruments (both airborne and ground based).

6. The results of this study have recently been submitted for publication in Geophysical Research Letters as part of a special section on the ALOHA-90 campaign. Copies of these papers are appended. Although there is still much data to be analyzed the campaign was a great success and we have already achieved several of our stated goals.

(Dr M.J. Taylor)

Appendix 1

NEAR INFRARED IMAGING OF HYDROXYL WAVE STRUCTURE OVER AN OCEAN SITE AT LOW LATITUDES

M.J. Taylor and M.J. Hill

Physics Department, University of Southampton,
Southampton, SO9 5NH, U.K.

Abstract. Coordinated observations of wave structure in the near infrared hydroxyl (OH) nightglow emission have been made from Maui, Hawaii using a suite of narrow angle and all-sky TV cameras. Two sets of data were obtained, the first in conjunction with the ALOHA-90 campaign and the second during the subsequent new moon period. Well formed, short period (< 20 min) wave patterns of comparable morphology, dynamics and abundance to those regularly imaged from mid-latitude mountain sites were detected on several occasions. Although the Hawaiian islands comprise several high volcanic peaks, the patterns were not consistent with gravity waves generated by the interaction of strong winds with the local island topography. This suggests that other mid-latitude wave patterns may also not be of mountain origin. The wave patterns imaged during ALOHA-90 were of significantly lower contrast than those detected later. This effect may be related to changes in the characteristics of the middle atmosphere that occur shortly after the spring equinox.

Introduction

Photographic and low light TV observations of wave structure in the near infrared (NIR) OH nightglow emission (peak altitude ~ 87 km, halfwidth 5-8 km) have been made from several mid-latitude sites for almost two decades [Peterson and Kieffaber, 1973; Moreels and Herse, 1977; Armstrong, 1986; Taylor et al., 1987]. Measurements have also been obtained at auroral latitudes [Clairemidi et al., 1985] and from within the arctic polar cap [Taylor and Henriksen, 1989]. The data frequently show extensive wave-like patterns exhibiting horizontal wavelengths shorter than 100 km.

To date there is very little information available on mesospheric wave motions that occur at low latitudes. Peterson [1979] reported visual and near infrared photographic observations from Hawaii of two small scale wave events (termed ripples), but no details were given of any other wave patterns that may have been detected. Subsequent attempts to image wave structure at low latitudes from Puerto Rico (18.5°N), during the AIDA '89 campaign were restricted by poor observing conditions.

These observations of the NIR and visible nightglow emissions from Hawaii allow the properties of short period mesospheric wave motions that occur at low latitudes over an oceanic site to be investigated and compared with those regularly observed at mid-latitudes.

Observations and Results

Observations were made from the Department of Energy (DOE) building, Haleakala Crater, Maui (20.8°N , 156.2°W , 2970m), over two consecutive new moon periods; 18

March-4 April during the ALOHA-90 campaign, and 18-27 April to provide additional data on mesospheric wave activity shortly after the spring equinox. The high altitude and favourable weather during these periods provided excellent conditions for imaging structure in the faint nightglow emissions.

Four cameras were operated, three of which were broad band NIR OH imagers; a narrow field Isocon (30°), a medium field CCD (55°), an all-sky Isocon (180°), and an all-sky "monochromatic imager" filtered to observe structure in the OH (557.7 nm) nightglow emission (peak altitude ~95 km). Further details of the instrumentation are given in the ALOHA-90 overview paper [Gardner, 1991]. On several occasions during this campaign, remarkably coherent but faint NIR wave patterns were imaged. Comparison with spectrometer observations confirmed that these displays were due primarily to variations in the OH emission [Taylor et al., 1991].

Figure 1 shows four examples of wave structure imaged by the CCD camera at low elevations (~15°) during ALOHA-90. The wave patterns were clearest in the CCD data which had the highest signal-to-noise ratio. Measurements of the horizontal scale size and motion of each of these wave patterns are listed in Table 1. Figure 1a shows several faint coherent wave crests curving upwards from the eastern horizon. The image was obtained on 21 March at 11:34 UT and formed part of an extensive display that lasted for about 2 hours. The pattern had an average horizontal wavelength, λ_x , of ~25 km and moved with a speed, v_x , of ~47 ms⁻¹, indicating an apparent period, τ , of ~9 min. A similar short period display (~12 min) is shown in Figure 1b. The pattern was detected on 24 March, also around noon UT, but to the south and west of the site. Unfortunately meteorological cloud (seen in the low elevation foreground of the picture) limited the observations this night.

Figure 1c shows another well developed wave display. The data were obtained at 12:16 UT on 30 March looking northwards. On this occasion images of wave structure were also made in the zenith indicating an extensive spatially coherent display over much of the sky (confirmed by the NIR all-sky observations). Initially faint structure was detected around 08:00 UT but it was not until later that the display became as conspicuous as shown in the figure. A similar enhancement in wave activity during the latter half of the night was noticed on several other occasions.

Sometimes much smaller scale wave patterns termed "ripple events" [Peterson, 1979] were detected. Figure 1d is an example and it can be seen that the morphology of the wave forms is quite different. In particular, ripples are significantly smaller in geographical extent and have shorter lifetimes (typically <1 hour) than the displays discussed above. In this example the average separation of the wave crests was 14.5 km and the wave packet moved with a uniform velocity of 46 ms⁻¹ indicating an apparent period of 5.3 min, close to the local Brunt-Väisälä period. Unlike the larger scale motions, ripples are thought to be caused by localised regions of strong wind shear generating Kelvin-Helmholtz instabilities in the mesosphere.

Discussion

Wave displays of comparable morphology and dynamics to the examples shown in Figure 1 were detected on many occasions during ALOHA-90, and the subsequent new moon period, indicating a wealth of short period mesospheric wave structure over the Hawaiian islands. In particular the patterns shown in Figure 1a,b,c exhibit good correspondence with the mid-latitude wave patterns termed "stripes" [Taylor and Henriksen, 1989]. The principal features of this type of display are:

Horizontal wavelength: 20-70 km,
Horizontal velocity: $10\text{-}50\text{ ms}^{-1}$,
Lateral extent $>500\text{ km}$,
Duration: 0.5-2 hours.

The majority of the reports detailing measurements of mid and high latitude wave structure are of this type. Experimental and theoretical investigations indicate that many of the patterns are induced by the passage of short period (10-20 min) gravity waves through the nightglow layers e.g. Taylor et al. [1987]. As similar wave motions were also detected over the Hawaiian islands this suggests that the sources of short period gravity waves are plentiful and can occur at any latitude.

Nearly all of the mid-latitude observations were made either from high altitude mountain sites (to facilitate the seeing conditions) or in the vicinity ($<500\text{ km}$) of large mountainous regions. Wave activity in the upper troposphere and lower stratosphere is considerably enhanced over mountain regions compared with the oceans. Much of this enhancement has been attributed to the interaction between strong tropospheric winds and the surface topography generating gravity waves (mainly in the lee of the mountains). Schoeberl [1985] has modelled the propagation of mountain waves through the stratosphere and mesosphere up to an altitude of 70 km. He determined that orographically induced gravity waves with horizontal scale sizes greater than 30 km may penetrate freely into the upper atmosphere.

If mountains are a primary source of the short period wave motions seen in the nightglow emissions then it is reasonable to expect considerably less wave activity over a remote oceanic site such as the Hawaiian islands (which are over 3,000 km from any sizeable land mass) than over a large mountainous region such as the Rockies. During both observing periods NIR wave structure was imaged on a remarkably high percentage of nights (nearly every night, but not all night). This compares with typically 30-80% of the clear sky observing time at mid-latitudes, depending on site and season. This suggests that there are similar type sources for the waves observed over the Hawaiian islands and over large mountainous region.

However, as the Hawaiian islands themselves consist of several high volcanic mountains then prevailing winds blowing over local island peaks (such as Haleakala Crater) may be a rich source of gravity waves. Balsley and Carter, [1989] and Hines, [1989] have investigated the properties of mountain waves observed in the upper troposphere and lower stratosphere. Whether these waves propagate significant amounts of energy into the upper mesosphere is not proven. Due to the isolated location of the Hawaiian islands any gravity waves generated by topographic forcing should be distinguishable from waves of meteorological (or other) origin as they should be observed primarily downwind of the source mountain(s) and should feature near zero phase speeds (since mountain waves are stationary), and curved wave crests (as the wave patterns are viewed at a range of only a few hundred km). Although curved wave patterns were observed on some occasions (Figure 1a) the majority of the displays were highly linear and often extended over much of the sky including the zenith (Figure 1c). Furthermore, all of the displays examined so far have exhibited substantial horizontal motion (see Table 1) and no preferred direction of propagation indicating other sources for the waves.

Compared with data recently obtained using the same instruments at a mountain site near Nederland, Colorado (40.0°N , 105.6°W) the wave patterns imaged during ALOHA-90 were of significantly lower contrast ($<10\%$) and proved quite difficult to detect. During the subsequent new moon period the contrast of the displays was considerably

higher. In the OI (557.7 nm) emission similar morphology wave patterns were imaged on several occasions during this period, but only once during ALOHA-90. Unfortunately the CCD camera was not available for the second observing interval and a quantitative comparison of the intensity and contrast of the patterns can not be made. However, the marked improvement in contrast manifested itself as an apparent increase in wave activity as detected by the OH all-sky camera. Figure 2 plots the number of hours wave structure was detected somewhere within the all-sky field (~500 km circular) for both new moon periods. Due to the good seeing conditions observations were possible on most nights. Wave structure was detected on nearly every occasion but many more high contrast displays were observed after the spring equinox.

As well as this temporal increase, the all-sky data indicate wave forms over a larger spatial area. This effect may be directly related to the higher contrast of the structures or it may indicate an increase in the number of potential sources in the vicinity of the Hawaiian islands. For tropospheric wave sources an alternative possibility is that the background winds in the stratosphere and lower mesosphere changed significantly in the interval between the two observing periods. The COSPAR atmospheric model for 20°N indicates a mean zonal wind component in March around 40 ms⁻¹ at ~60 km height. Depending on the direction of propagation, waves with phase speeds lower than this peak value will be strongly attenuated in the lower mesosphere. However, in April this wind drops to less than 20 ms⁻¹ and waves of lower phase speed (similar to those regularly seen in the nightglow emissions) may propagate freely into the upper atmosphere. The fact that wave structure was detected frequently in both the OH and the OI (557.7 nm) emissions during the post equinox period supports the argument for freely propagating wave motions possibly of meteorological origin. However, during ALOHA-90 there is also good evidence for the in situ generation of short period waves [Taylor and Edwards, 1991].

Summary

Short period (<20 min) mesospheric wave structure frequently exists at low-latitudes over the Hawaiian islands (at least around the spring equinox). Many of the wave patterns imaged were highly coherent and exhibited similar morphology and dynamics to the nightglow displays seen at mid and high latitudes.

The search for mountain waves induced by the interaction of surface winds with the local island topography is continuing. However, the evidence obtained so far suggests (but is by no means conclusive) that gravity waves generated by this mechanism may not be an important source of the short period wave motions seen in the upper atmosphere. For waves of meteorological origin wind filtering in the intervening atmosphere may play a critical role in governing the visibility of wave patterns of low phase speed.

Acknowledgements. We are most grateful to the director J. Dryden and staff of Holmes and Narver Inc. for arranging the use of the DOE facility on Haleakala Crater for the measurements. In particular we thank K. Hiner and L. Yamaguchi for their logistic support. We acknowledge V. Taylor for assistance during the observations and R. Edwards for help with the data analysis. Funding for this project was provided by University of Cincinnati as part of the U.S. Air Force Office of Scientific Research MAPSTAR programme.

References

- Armstrong, E.B., Irregularities in the 80-100 km region: A photographic approach, Radio Sci., **21**, 313-318, 1986.
- Balsley, B.B., and D.A. Carter, Mountain waves in the tropical Pacific atmosphere: a comparison of vertical wind fluctuations over Pohnpei and Christmas island using VHF wind profilers, J. Atmos. Sci., **46**, 2698-2715, 1989.
- Clairemidi, J., M. Herse, and G. Moreels, Bi-dimensional observation of waves near the mesopause at auroral latitudes, Planet. Space Sci., **33**, 1013-1022, 1985.
- Gardner, C.S., Introduction to ALOHA-90: the airborne lidar and observations of the Hawaiian airglow campaign, Geophys. Res. Lett., this issue, 1991.
- Hines, C.O., Tropopausal mountain waves over Arecibo: a case study, J. Atmos. Sci., **46**, 476-488, 1989.
- Moreels, G., and M. Herse, Photographic evidence of waves around the 85 km level, Planet. Space Sci., **25**, 265-273, 1977.
- Peterson, A.W., Airglow events visible to the naked eye, Appl. Optics, **22**, 3390-3393, 1979.
- Peterson, A.W., and L.M. Kieffer, Infrared photography of OH airglow structures, Nature, **242**, 321-322, 1973.
- Schoeberl, M.R., The penetration of mountain waves into the middle atmosphere, J. Atmos. Sci., **42**, 2856-2864, 1985.
- Taylor, M.J., M.A. Hapgood, and P. Rothwell, Observations of gravity wave propagation in the OI (557.7 nm), Na (589.2 nm) and the near infrared OH nightglow emission, Planet. Space Sci., **35**, 413-427, 1987.
- Taylor, M.J. and K. Henriksen, Gravity wave studies at polar latitudes, in Electromagnetic Coupling in the Polar Clefts and Caps, edited P.E. Sandholt and A. Egeland, pp. 421-434, Kluwer Academic Pub., Dordrecht, 1989.
- Taylor, M.J. and R. Edwards, Observations of short period mesospheric wave patterns; evidence for in situ wave generation?, Geophys. Res. Lett., this issue, 1991.
- Taylor, M.J., D.N. Turnbull, and R.P. Lowe, Coincident imaging and spectrometric observations of zenith OH nightglow structure, Geophys. Res. Lett., this issue, 1991.

(Received April 5, 1991;
accepted May 7, 1991.)

Copyright 1991 by the American Geophysical Union.

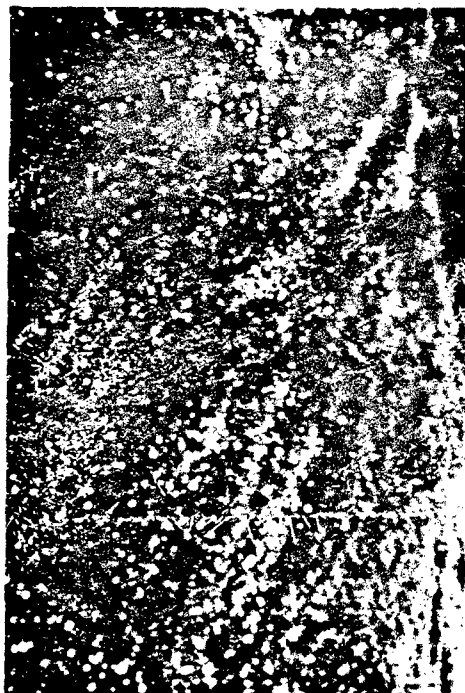
List of Figures

Fig. 1. Four examples of wave structure in the near infrared OH nightglow emission imaged by the CCD camera during the ALOHA-90 campaign. Each image has been flat fielded to enhance the visibility of the faint displays. Note the similar morphology of the wave patterns except in picture (d) which shows a small scale ripple event. Each image was obtained using an integration time of 20s.

Fig. 2. Histogram plots the number of hours NIR wave structure was detected somewhere within the all-sky field for (a) the ALOHA-90 campaign and (b) the subsequent new moon period. The solid areas indicate when structure was detected over the whole sky while the shaded areas signify the presence of some structure within the camera field but not the amount. (Note CCD data were obtained for longer periods of time than indicated in (a) due to the higher sensitivity of the camera.)

TABLE 1. Measurements of the average horizontal wave parameters for the four wave patterns shown in Figure 1 (assuming an emission altitude of 87 km).

Picture	Date	$\lambda_x(\text{km})$	$v_x(\text{ms}^{-1})$	$\tau(\text{min})$
(a)	21 March	25	47	9
(b)	24 March	21	29	12
(c)	30 March	23	30	13
(d)	20 March	14.5	46	5.3



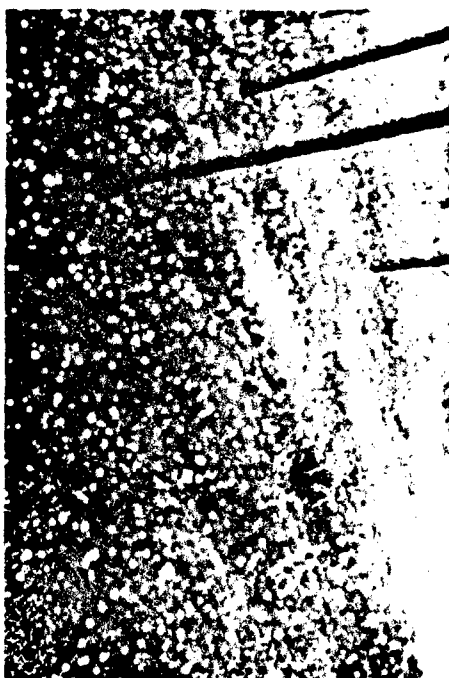
(a)



(b)



(c)



(d)

Figure 1 - Four examples of wave structure in the near infrared OH nightglow emission imaged by the CCD camera during the ALOHA-90 campaign. Each image has been flat fielded to enhance the visibility of the faint displays. Note the similar morphology of the wave patterns except in picture (d) which shows a small scale ripple event. Each image was obtained using an integration time of 20s.

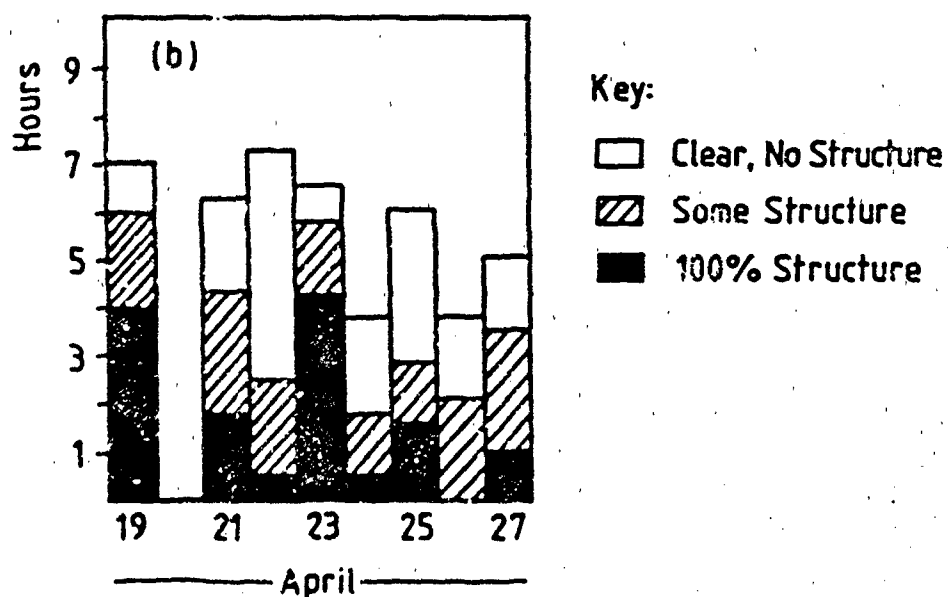
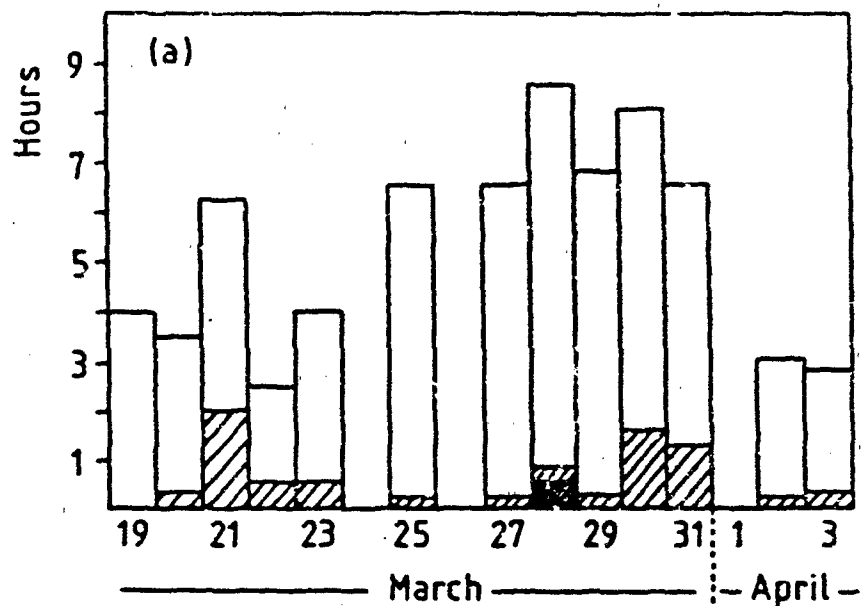


Figure 2 - Histogram plots the number of hours NIR wave structure was detected somewhere within the all-sky field for (a) the ALOHA-90 campaign and (b) the subsequent new moon period. The solid areas indicate when structure was detected over the whole sky while the shaded areas signify the presence of some structure within the camera field but not the amount. (Note CCD data were obtained for longer periods of time than indicated in (a) due to the higher sensitivity of the camera.)

Appendix 2

OBSERVATIONS OF SHORT PERIOD MESOSPHERIC WAVE PATTERNS: IN SITU OR TROPOSPHERIC WAVE GENERATION?

M.J. Taylor, and R. Edwards

Physics Department, University of Southampton,
Southampton, SO9 5NH, U.K.

Abstract. Near infrared images showing wave structure in the hydroxyl (OH) nightglow emission have been obtained from Maui, Hawaii during the ALOHA-90 campaign. Analysis of two nights during this campaign (25 and 31 March) indicate extensive, highly coherent, linear wave patterns of very short apparent period (~5 and 10 min respectively). Both displays exhibited several features characteristic of the in situ breakdown of a large scale, long period, upper atmospheric wave disturbance. Data in support of this mechanism was found by other ALOHA instruments which detected concurrent long period (1-2 hour) mesospheric wave disturbances on both occasions. However, a tropospheric source for these waves cannot be ruled out. At least on 25 March a weather front occurred at ~1400 km range with a favourable orientation and location. Although its range was relatively large, back-ground winds may have substantially increased the path length of the waves through the intervening atmosphere.

Introduction

The presence of coherent wave structure in the mid-latitude mesospheric nightglow emissions is well established [Moreels and Herse, 1977; Armstrong, 1986; Taylor et al., 1987]. Detailed observations have shown that these patterns often exhibit properties associated with short period (10-20 min) gravity waves. During the ALOHA-90 campaign similar morphology wave forms were detected at low latitudes over an ocean site [Taylor and Hill, 1991].

Many sources for these waves have been suggested. They include tropospheric disturbances such as jet streams, storms, weather fronts and the interaction of strong winds with large mountains (generating lee-type gravity waves). Several upper atmospheric sources have also been postulated; they include the auroral electrojet, strong particle precipitation and the in situ breakdown of large-scale, long period atmospheric waves such as tides. It is often difficult to identify individual wave sources from the wealth of potential disturbances. For tropospheric sources this problem is further complicated by the effects of background winds in the intervening atmosphere, which can significantly modify the wave propagation. Images of structure in the nightglow emissions give unique 2-dimensional information on the horizontal wavelength and apparent phase velocity of the gravity wave perturbation. These data together with the location, shape, orientation and time of occurrence of the display have proved valuable for finding possible wave sources [Taylor and Hapgood, 1988]. By imaging structure in the nightglow emissions from the Hawaiian islands the sources of short period gravity waves over a low latitude oceanic site can be investigated.

Observations and Results

Observations were made from the Department of Energy (DOE) building, Haleakala Crater, Maui (20.8°N, 156.2°W, 2970m). The high altitude and favourable weather during the campaign (18 March-4 April) provided excellent conditions for imaging structure in the nightglow emissions. The measurements reported here were made with a medium field (55°) CCD camera filtered to observe the near infra-red (NIR) OH nightglow emission (wavelength range 780-1000 nm). Further details of the instrumentation are given in the ALOHA-90 overview paper [Gardner, 1991]. Wave patterns were imaged on several occasions during the campaign [Taylor and Hill, 1991]. In this report the properties of two faint wave displays imaged on 25 March and 31 March are examined and compared with simultaneous airborne and ground based measurements.

25 March Display

Observations were made from 06:00 UT until dawn twilight at 15:40 UT. A well formed set of steeply inclined wave-like structures was detected at low elevation to the northeast. Figure 1 shows a CCD image of the NIR display at 07:10 UT. Several faint forms emanating from the northeastern horizon are evident. The structures are clearest on the right of the image but the data shows that similarly orientated wave crests exist across the whole field. The uniformity of the wave pattern is quite remarkable. The display was clearest around 06:30-08:00 UT, but was still evident at 11:00 UT nearly 5 hours later.

A similarly shaped but fainter wave pattern was also detected to the southwest of the site. Figure 2 shows a composite ground map of the nightglow display imaged to the northeast at 07:10 UT (Figure 1) and an hour later to the southwest. The flight path of the aircraft during this night is also marked on the figure. Each image was calibrated using known stars as reference points [Hapgood and Taylor, 1982] and mapped onto the ground assuming an emission altitude of 87 km. The geographical location and orientation of the two wave sets indicates an extensive, spatially and temporally coherent display, containing many wave crests > 800 km in length. To the south, in the direction of the airborne measurements, there was no obvious wave structure, but this direction was affected by light from the Milky Way. The average separation of the wave crests, determined from several images, gave a horizontal wavelength (λ_x) of 15.2 ± 0.6 km. The displacement of the wave crests (measured over an interval of 90 min) yielded a mean velocity (v_x) of 51 ± 5 ms⁻¹ towards the southeast, indicating an unusually short apparent wave period (τ) of 5.0 ± 0.5 minutes.

31 March Display

During this night wave structure was detected at most azimuths but was clearest to the west and north. To the west the wave pattern consisted of several steeply inclined crests of similar morphology to those observed on 25 March (Figure 1). To the north the wave crests appeared near horizontal. Figure 3 shows a composite ground map of the structures at 09:36 UT (to the west) and 18 minutes later to the north. The coherence of the structures is not as marked as those imaged on 25 March (Figure 2). Nevertheless, the map clearly shows two sections of an extensive wave display viewed at orthogonal azimuths. A series of images obtained at elevation angles ranging from 17° to 90° confirmed the existence of coherent wave crests extending from the northern and

western horizon through the local zenith. The pattern was present all night indicating a duration of over 6 hours. Measurements of the horizontal parameters of the wave pattern during the interval 06:30-08:00 UT gave $\lambda_x = 19.8 \pm 0.8$ km, $v_x = 32 \pm 4$ ms⁻¹ towards the north signifying an apparent wave period $\tau = 10.3 \pm 1.4$ min.

Discussion

Both wave patterns were extensive ($>250,000$ km²), remarkably coherent, and lasted for several hours. Their horizontal wavelengths and linear morphology were also comparable, indicating similar sources for the disturbances. However, the apparent (i.e. observed) wave periods were significantly different at 5.0 and 10.3 min on 25 and 31 March respectively. In the presence of a background wind the intrinsic period of the gravity wave is Doppler shifted with respect to its apparent period:

$$\tau_i = \tau [v_x / (v_x - \bar{u})] \quad (1)$$

where \bar{u} is the horizontal background wind component in the direction of motion of the wave, τ is the apparent period as measured by an observer on the ground and τ_i is the intrinsic (or true) period of the wave measured in a frame of reference moving with the background wind. The intrinsic period of the wave motion may therefore be significantly different from the apparent period of the wave pattern.

The motion of the gravity wave through the atmosphere depends on its intrinsic period [Hines, 1960] which is usually indeterminate. However, as the apparent horizontal velocity of the wave will be independent of the background wind regardless of height [Hines, 1968], measurements of λ_x and v_x of the nightglow wave patterns (and hence τ) are very useful for studies of the wave sources. On the other hand, if the waves are generated by a disturbance that is moving with respect to the observer, the apparent period of the wave pattern will vary with \bar{u} at the height of the source.

Tropospheric Source

The extensive nature and linear form of both OH displays would suggest either a point-like source such as a thunderstorm [Taylor and Hapgood, 1988] but at a range of at least 1000 km from the observing site, or an extended "line type" source such as a weather front or a jet stream close to the observing site [Hines, 1968]. Without a measurement of the background wind in the intervening atmosphere it is difficult to estimate the range over which the wave energy can propagate. However, gravity waves generated nearby by strong winds blowing over local island peaks (such as Haleakala Crater) can be effectively ruled out on both occasions because of the large lateral extent of the displays and their close proximity and relative motion with respect to the Hawaiian islands (Figures 2,3).

Surface weather charts for 24 and 25 March indicate an extensive high pressure area to the northeast of Hawaii with a well developed low to the northwest both at a large range (>2000 km). An extended cold front, associated with these pressure centres, moved steadily towards the southeast, and came to a halt between 00:00 and 12:00 UT on 25 March at a distance of ~ 1400 km from the observing site. Both the orientation and location of the front agree well with the observed wave motion (Figure 2) but its range was relatively large.

In the absence of background winds wave energy from a tropospheric source of apparent period ~ 5 min would reach the OH layer at a quite short ground range of < 100 km (assuming the vertical extent of the source region was no greater than the atmospheric scale height) [Hines, 1967]. If the background winds in the intervening atmosphere substantially increased the intrinsic period of the waves on this occasion they could travel very large horizontal distances. This situation would arise if $\bar{u} = v_x$ (~ 50 ms^{-1}) over an extended height interval between the source and the region of observation (equation 1).

On 30 and 31 March surface weather charts show a cold front associated with a developing low and a high pressure region to the north of Hawaii at a range of ~ 1500 km. Although aligned in a direction similar to that of the OH wave pattern its location is not consistent with the northward wave motion observed in the nightglow data. To the south of Hawaii there were no obvious weather sources within 30° of latitude.

In Situ Source

If the short period waves were generated in the upper atmosphere in the vicinity of the OH layer then they would most probably have been vertically evanescent. The long lifetimes and the large geographic extent of the wave patterns also suggests that the source regions were extensive and long lasting. One possible mechanism that could account for the observations has been postulated by Tuan et al. [1979]. Under certain conditions long period waves propagating through the upper atmosphere may partially break, generating coherent, small-scale waves of intrinsic period close to the local Brunt-Väisälä period. On both 25 and 31 March τ_b was found to be about 4.6 min (using spectrometer data of Turnbull and Lowe, [1991]). If both wave patterns were generated with an intrinsic period of this value then the difference in the apparent wave periods may have been the result of differing local wind conditions at the source height on each night. The apparent period on 25 March was very close to τ_b indicating a background wind component $\bar{u} \sim 3$ ms^{-1} in the direction of motion of the wave (equation 1). However, on 31 March a neutral wind $\bar{u} \sim 38$ ms^{-1} would have been needed to account for an apparent period of ~ 10 min. Neutral winds of this magnitude and variability are frequently observed at nightglow altitudes but unfortunately there were no coincident measurements over Maui with which to compare these observations.

If the short period waves were generated in situ by this mechanism then their occurrence, speed and direction of motion should be associated with the presence of a large scale wave disturbance on each occasion. Evidence for the presence of long period wave disturbances on both occasions was found in the measurements of the other ALOHA-90 instruments. On 25 March the airborne observations were made to the south of Maui (Figure 2). Sodium lidar measurements were obtained from 08:50 to 15:00 UT (mainly outside the limits of the camera field of view). However, close to the equator a strong disturbance of horizontal wavelength 400-550 km was measured [C.S. Gardner, personal communication, 1991]. Zenith spectrometer measurements from Haleakala show a near linear decrease in OH (3,1) band intensity during most of the night with a small wave-like disturbance of quasi-period ~ 1.2 hour [Turnbull and Lowe, 1991]. Coincident observations by the Aerospace group using a zenith pointing CCD imager show similar period, low amplitude variations in the OH (6,2) band emission and the O_2 (0,1) Atmospheric band. The disturbance moved towards the southeast at a speed of 50-100 ms^{-1} , in a direction comparable with that of the short period wave pattern [Hecht and Walterscheid, 1991].

On 31 March the OH emission was brighter and the spectrometer measured large amplitude wave-like disturbance with dominant periods 2.2 and 1.2 hours in both intensity and temperature. The Aerospace images showed that the disturbance was moving at a velocity of $30\text{--}50\text{ ms}^{-1}$ similar in magnitude to that of the short period wave pattern but in a general eastward direction. The aircraft flew almost due west (Figure 3) and measurements over the period 08:00-15:30 UT show peaks in the horizontal spectra with wavelengths of 170 and 340 km again indicating a large scale wave motion. However, as the aircraft flight path was almost parallel to the OH wave pattern the true horizontal wavelength may have been much shorter.

Summary

Observations of extensive ($>250,000\text{ km}^2$) linear wave patterns with short apparent periods ($\leq 10\text{ min}$) and long lifetimes (several hours) are most unusual. Whether these displays are peculiar to low latitude or oceanic sites remains unknown. On 25 March there was a favourably orientated weather front where linearly extensive short period ($< 10\text{ min}$) gravity waves may have been generated. However, if the waves originated in this region then background winds in the intervening atmosphere must have played an important role in considerably increasing their horizontal range. No obvious source was found for the 31 March display.

It appears more likely that the waves reported here were generated in the upper atmosphere in the vicinity of the OH layer. Both patterns exhibited many of the properties characteristic of the sustained breakdown of a large scale upper atmospheric wave disturbance (possibly of tidal origin). Supporting evidence showing concurrent long period (1-2 hour) mesospheric wave disturbances was found on both occasions. Several other short period ($\leq 10\text{ min}$) displays were also imaged during the ALOHA-90 campaign but it is not yet known if they were associated with long period upper atmosphere wave disturbances. Measurements of gravity waves at low latitudes are few and these data may offer new evidence for the in situ generation of short period waves in the upper atmosphere. However, the possibility that the waves were generated by other weather disturbances such as jet streams [see Hines, 1968] or distant thunderstorms [Taylor and Hapgood, 1988] has yet to be investigated.

Acknowledgements. We are most grateful to the director J. Dryden and staff of Holmes and Narver Inc. for arranging the use of the DOE facility on Mt. Haleakala for the measurements. We thank M.J. Hill for his considerable help both prior to and during the campaign and B.S. Lanchester for many useful discussions. We acknowledge our ALOHA-90 colleagues for the use of their data. Funding for this project was provided through the University of Cincinnati as part of the U.S. Air Force Office of Scientific Research MAPSTAR programme.

References

- Armstrong, E.B., Irregularities in the 80-100 km region: A photographic approach, Radio Sci., **21**, 313-318, 1986.
- Gardner, C.S., Introduction to ALOHA-90: the airborne lidar and observations of the Hawaiian airglow campaign, Geophys. Res. Lett., this issue, 1991.
- Hapgood, M.A., and M.J. Taylor, Analysis of airglow image data, Ann. Geophys., **38**, 805-813, 1982.
- Hecht, J.H., and R.L. Walterscheid, Observations of the OH Meinel (6,2) and O₂ Atmospheric (0,1) nightglow emissions from Maui during the ALOHA-90 campaign, Geophys. Res. Lett., this issue, 1991.
- Hines, C.O., Internal atmospheric gravity waves at ionospheric heights, Can. J. Phys., **38**, 1441-1481, 1960.
- Hines, C.O., On the nature of travelling ionospheric disturbances launched by low-altitude nuclear explosions, J. Geophys. Res., **72**, 1877-1882, 1967.
- Hines, C.O., A possible source of waves in noctilucent clouds, J. Atmos. Sci., **25**, 937-942, 1968.
- Moreels, G., and M. Herse, Photographic evidence of waves around the 85 km level, Planet. Space Sci., **25**, 265-273, 1977.
- Taylor, M.J., M.A. Hapgood, and P. Rothwell, Observations of gravity wave propagation in the OI (557.7 nm), Na (589.2 nm) and the near infrared OH nightglow emission, Planet. Space Sci., **35**, 413-427, 1987.
- Taylor, M.J., and M.A. Hapgood, Identification of a thunderstorm as a source of short period gravity waves in the upper atmospheric nightglow emissions, Planet. Space Sci., **36**, 975-985, 1988.
- Taylor, M.J., and M.J. Hill, Near infrared imaging of hydroxyl wave structure over an ocean site at low latitudes, Geophys. Res. Lett., this issue, 1991.
- Tuan, T.F., R. Hedinger, S.M. Silverman, and M. Okuda, On gravity wave induced Brunt-Väisälä oscillations, J. Geophys. Res., **84**, 393-398, 1979.
- Turnbull, D.N., and R.P. Lowe, Temporal variations in the hydroxyl nightglow observed during ALOHA-90, Geophys. Res. Lett., this issue, 1991.

(Received April 5, 1991;

revised June 5, 1991;

accepted June 10, 1991.)

Copyright 1991 by the American Geophysical Union.

List of Figures

Fig.1 CCD image showing NIR wave structure imaged to the NE on 25 March at 07:10 UT. The camera was aimed at an elevation of 20° and had a field of view of 55° by 30° .

Fig.2 Composite map showing the scale size and geographic location of the OH wave forms imaged to the NE and SW of Maui on 25 March, assuming an emission altitude of 87 km (only the brightest wave forms have been plotted). The x marks the aircraft location at 09:10 UT on the outward leg and 15:30 UT on the return leg.

Fig.3 Composite map showing the OH wave display of 31 March. For comparison the data are plotted on the same scale as Figure 2. The aircraft flew due west almost parallel to the wave structures.



Figure 1 - CCD image showing NIR wave structure imaged to the NE on 25 March at 07:10 UT. The camera was aimed at an elevation of 20° and had a field of view of 55° by 30° .

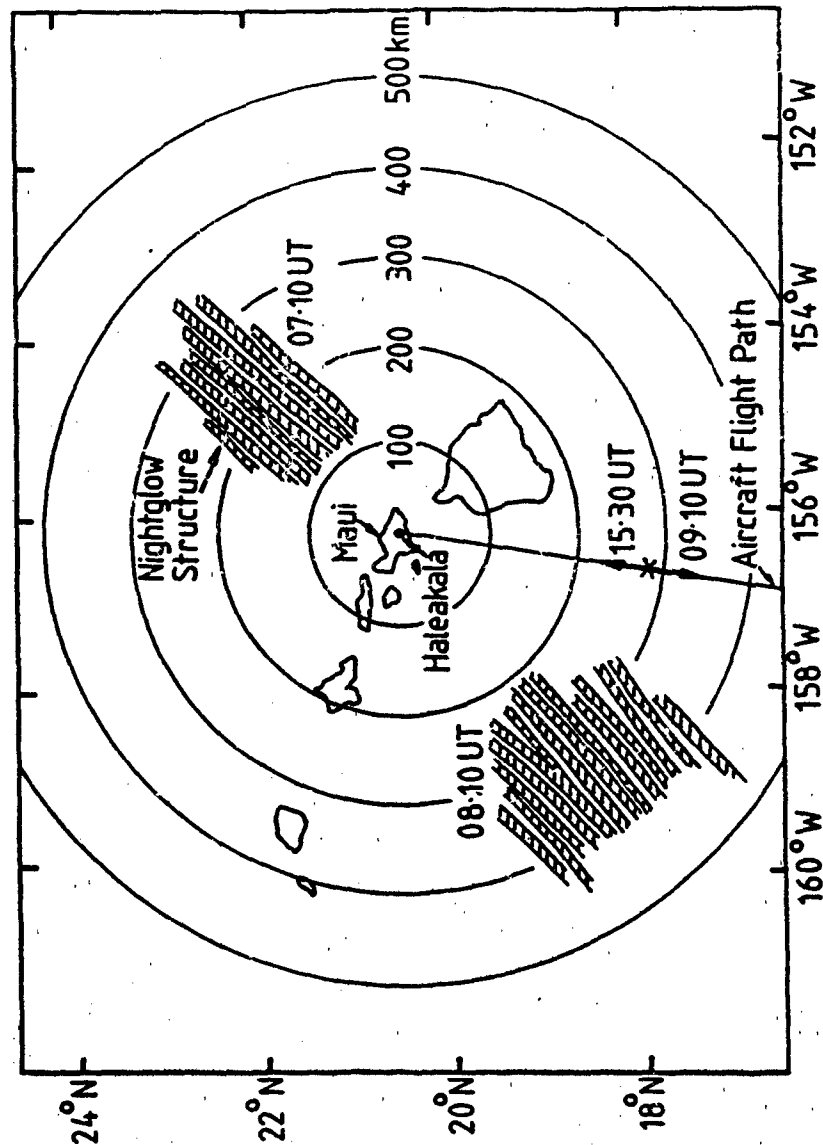


Figure 2 - Composite map showing the scale size and geographic location of the OH wave forms imaged to the NE and SW of Maui on 25 March, assuming an emission altitude of 87 km (only the brightest wave forms have been plotted). The x marks the aircraft location at 09:10 UT on the outward leg and 15:30 UT on the return leg.

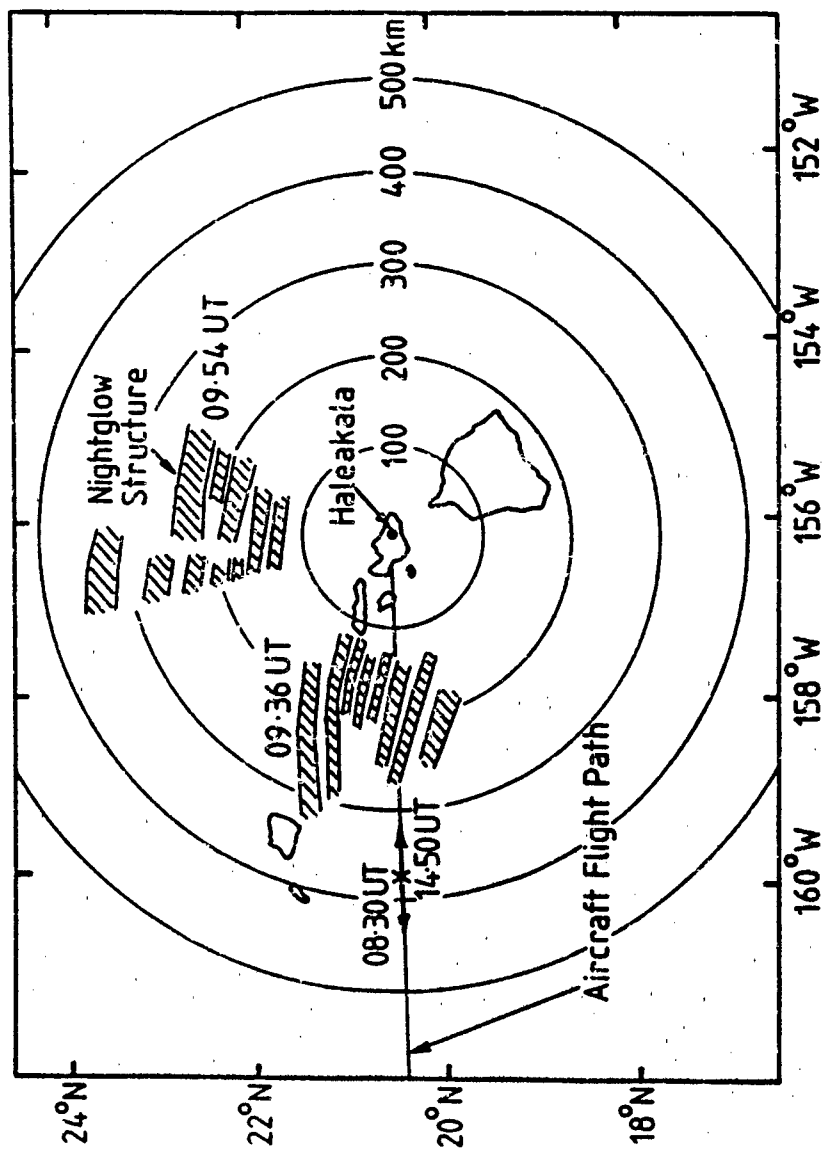


Figure 3 - Composite map showing the OH wave display of 31 March. For comparison the data are plotted on the same scale as Figure 2. The aircraft flew due west almost parallel to the wave structures.

Appendix 3

COINCIDENT IMAGING AND SPECTROMETRIC OBSERVATIONS OF ZENITH OH NIGHTGLOW STRUCTURE

M.J. Taylor

Physics Department, University of Southampton,
Southampton, SO9 5NH, U.K.

D.N. Turnbull, and R.P. Lowe

Institute for Space and Terrestrial Science and,
Physics Department, The University of Western Ontario,
London, Ontario, Canada

Abstract. During the ALOHA-90 campaign a novel comparative study was made between near infrared wave structure imaged in the zenith using a CCD camera and that detected at infrared wavelengths by a Fourier Transform Spectrometer. Coincident measurements were made briefly on several occasions and for an extended period on 31 March. The temporal variations imaged in the near infrared structure during this night almost completely matched those detected in the OH (3,1) band spectrometer data when similar viewing fields were compared. However, the image data also displayed small scale wave forms that were not resolved by the larger field instrument. These structures exhibited significant changes in brightness and position on a time scale much shorter than the local Brunt-Väisälä period indicating that very high resolution measurements are necessary to investigate short period (<20 min) upper atmospheric wave motions.

Introduction

For many years spectrometric measurements of the night sky have been made to ascertain the nature and origin of the upper atmospheric nightglow emissions. More recent investigations have been into quasi-periodic variations which often exhibit characteristics of freely propagating internal gravity waves [Noxon, 1978; Viereck and Deehr, 1989; Swenson et al., 1990]. Observations of the bright infrared OH Meinel band emissions, which originate from a well defined layer centred at ~87 km, have proved most useful in these studies. As the lower rotational levels of the OH emission are usually in thermodynamic equilibrium with the local atmosphere, measurements of both the emission intensity and its rotational temperature can be used as a tracer of the wave motion. Furthermore, long exposure photographic and low light video images of the near infrared (NIR) OH emission can be used to investigate the 2-dimensional horizontal properties of the wave disturbance [Moreels and Herse, 1977; Armstrong, 1986; Taylor et al., 1987].

In general, spectral observations suffer from difficulties in distinguishing between the induced temporal and spatial variations. Recently Taylor et al. [1991] have reported the results of a simultaneous imaging and interferometric study of short period (~14 min) wave structure in the OH nightglow emission. The measurements were made at low elevations, ~15°, (to aid the video observations), and show in detail the relationship

between a coherent gravity wave pattern and the induced intensity and temperature perturbations. During ALOHA-90 a similar comparison was made. Here we report novel observations of a small scale wave pattern imaged in the zenith and compare the intensity records with those detected by the spectrometer.

Observations

The instruments used were a CCD camera (University of Southampton) and a Fourier transform spectrometer (The University of Western Ontario), both of which were located on Haleakala Crater, Maui (20.8°N, 156.2°W, 2970m). A short description of the instruments and their operational characteristics is given by Gardner [1991]. The CCD camera imaged structure in the submicron nightglow emissions (half bandwidth 780-1000 nm) while the spectrometer measured the zenith intensity of several OH Meinel bands in the wavelength range 1000-1650 nm.

Most of the time the camera was used to investigate the low elevation sky in the direction of the aircraft flight path [Gardner, 1991]. However, on several occasions a search for structure in the zenith sky was made. Table 1 lists the dates and times of these measurements. Structure was imaged on every occasion that zenith measurements were attempted (total of six nights) but the observations were usually brief enough to determine only the scale size and orientation of the wave forms. However, on 31 March a series of images were recorded for detailed comparison with the spectrometer measurements.

31 March Display

A summary of the nightglow display imaged at low elevations during this night is given by Taylor and Edwards, [1991]. To the west and north of the site a uniform wave pattern of horizontal wavelength ~20 km was detected over a period of several hours (see their Figure 3). Images of wave structure in the zenith were obtained around 10:00 UT and again over three hours later. Figure 1 is a collection of six CCD images showing examples of the zenith nightglow structure recorded at 4 minute intervals from 13:14 UT. The pictures are quite exceptional and show considerable evolution and movement of the structures. Each image has been flat fielded (to remove the effects of lens vignetting etc that are present in the original records), and color enhanced to highlight the spatial features of the structures which exhibited low contrast ($\leq 5\%$). After 13:18 UT several wave-like forms are evident; the east-west orientation and separation of these structures is similar to those observed in the low elevation pattern, confirming its large geographic extent ($> 250,000 \text{ km}^2$). A total of 32 images of the zenith sky were recorded over the period 13:00-14:51 UT. The field of view of the camera (55° by 30°) was larger than the spectrometer sample area (30° circular), but smaller than the Aerospace Corporation camera (60° by 40°). The variation in responsivity of the spectrometer over its viewing field has not been measured.

Results and Discussion

Images showing nightglow wave structure at high elevations and in the zenith are rare [Peterson and Adams, 1983]. To date most of the video and photographic measurements reported in the literature have been made at low elevation angles to benefit from the 2-3 fold increase in emission intensity which occurs due to line of sight integration through

the nightglow layer. The observations reported here were made using a new broad band nightglow imager and clearly demonstrate the existence of NIR structure in the zenith as well as at low elevations. Although similarities in the separation and orientation of the wave forms are evident in each image, the intensity distribution is different, indicating considerable evolution of the wave field in a relatively small time interval (≤ 4 min).

By summing the video signal in a 30° square centred on the optic axis, the intensity of the NIR TV data can be compared with the OH (3,1) band intensity measured by the spectrometer. Figure 2a plots the relative intensity derived from the spectrometer data (averaged over 1 min intervals) during the period 13:00-15:00 UT [Turnbull and Lowe, 1991]. During the night both the OH relative intensity and the rotational temperature exhibited considerable wave-like variations. In particular a large scale perturbation of quasi-period ~ 2.2 hours was detected. This wave motion is present in the data from the larger field of view Aerospace camera [Hecht and Walterscheid, 1991]. However, the spectrometer also registered much smaller scale structures which are not seen in the Aerospace data, possibly due to averaging effects. These variations are significant and should be present in the image data.

Figure 2b plots the relative intensity derived from the 32 CCD images. The data were recorded at intervals ranging from 1 to 4 minutes using a fixed exposure time of 30s. Each point represents the average intensity of the video signal over a 30° square field. (Note, the dashed line linking the points serves only as a guide to the eye.) It is immediately apparent that the small scale intensity variations in the spectrometer data are also in the CCD data and with no obvious time shift. The video data were the sum of several signal components existing within the broad pass band of the camera (half-width 780-1000 nm) and include the OH (5,1), (6,2), (7,3), (8,4), (3,0) and (9,5) Meinel bands, the $O_2(0,1)$ Atmospheric band near 865 nm, the nightglow continuum and integrated starlight. However, as the temporal variations in the OH (3,1) band intensity are almost exactly duplicated in the image data this indicates that the variations in structure in the images were primarily due to changes in the OH emission. This is to be expected as the OH emission dominates this region of the nightglow spectrum having an integrated emission intensity of typically 12kR.

Alternatively, the intensity variations detected by both instruments could have been due to thin meteorological cloud (although none was visible). However, as the induced intensity and rotational temperature perturbations were highly correlated [Turnbull and Lowe, 1991], with no significant scatter that would result from thin cloud, there can be little doubt that the structures were caused by changes in the OH emission. Any similar perturbations in the NIR continuum and/or the $O_2(0,1)$ band emissions were therefore comparatively faint and/or were in near phase with the OH signal. The primary effect of these emissions was to reduce the contrast of the OH structures. The wave pattern imaged by the TV camera shows several features of smaller dimensions than the spectrometer sample area. (An indication of the limits of the circular spectrometer field is shown in Figure 1 by the large white box which shows the 30° square video sample area.) Thus, on this occasion the spectral signal was the spatial average of more than one nightglow feature. (Note the spectrometer data will be of higher spatial resolution than indicated by this box due to the somewhat smaller area of the 30° circular field.) To investigate the temporal properties of the display in more detail the CCD data have been re-analyzed using a smaller sample area of 5° square (marked by the small white box) which corresponds to a zenith "footprint" of ~ 8 km square. As the wavelength of the OH pattern was ~ 20 km individual bright and dark structures of this dimension should be resolved.

Figure 3 shows the relative intensity data for this sample field. For comparison the data have been plotted using the same intensity and time scales as Figure 2h. Although similar features are present in both plots the short wavelength structures are now evident and the overall contrast of the variations is increased. More critically, although a 4 minute sample interval (13:00-14:00 UT) is ample for tracking the large scale perturbations present in the figure, it is too long for registering accurately the small scale variations. After 14:15 UT the sample interval was reduced to 1 min and the variations are clearly detected. At the time of recording the data little or no change in the images were observed by eye. However, Figure 3 shows that significant changes in the integrated nightglow brightness took place on a minute-by-minute time scale.

Studies of wave structure in the upper atmosphere usually assume the local Brunt-Väisälä (buoyancy) period, τ_b , as a natural lower limit for the temporal resolution of the measurements. At nightglow altitudes τ_b is typically 5-6 min. Wave motions with phase velocities of a few tens ms^{-1} can propagate significant distances (several km) during this time. These measurements demonstrate the need for high temporal and spatial resolution when investigating the properties of short period (<20 min) waves that frequently occur in the nightglow emissions.

Summary

The good seeing conditions at this site permitted OH nightglow wave structure to be imaged in the zenith. The close similarity in the relative intensity data measured by the spectrometer and the CCD camera indicates no observable difference in the wave structure arising primarily from high OH vibrational levels ($v' > 5$) compared with that observed in the $v' = 3$ level of the OH (3,1) band. To date most image data on the nightglow emissions have been obtained at low elevations, and comparative studies with other optical devices are rare [Taylor et al., 1991]. The extension of high resolution imaging measurements into the zenith has several advantages but is made at the expense of signal level.

During ALOHA-90 NIR wave patterns of horizontal wavelength $\ll 100$ km were observed on several occasions. Large field instruments will naturally integrate out much of this structure which appears to be relatively common over both mountain and oceanic sites. Coincident imaging and spectrometric measurements of the OH emission are highly complementary: the spectrometer establishes the spectral integrity of the emission and gives accurate intensity and temperature data while the imager records the 2-dimensional spatial structure of the wave perturbation, its motion and temporal evolution.

Acknowledgements. We are most grateful to the director J. Dryden and staff of Holmes and Narver Inc. for the use of the DOE facility on Haleakala Crater. In particular we thank K. Hiner and L. Yamaguchi for their logistic support and V. Taylor for help with the image analysis. Partial support for this project was provided by the Air Force Office of Scientific Research as part of the MAPSTAR programme. The Institute for Space and Terrestrial Science is an Ontario Centre of Excellence.

References

- Armstrong, E.B., Irregularities in the 80-100 km region: A photographic approach, Radio Sci., **21**, 313-318, 1986.
- Gardner, C.S., Introduction to ALOHA-90: the airborne lidar and observations of the Hawaiian airglow campaign, Geophys. Res. Lett., this issue, 1991.
- Hecht, J.H., and R.L. Walterscheid, Observations of the OH Meinel (6,2) and O₂ Atmospheric (0,1) nightglow emissions from Maui during the ALOHA-90 campaign, Geophys. Res. Lett., this issue, 1991.
- Moreels, G., and M. Herse, Photographic evidence of waves around the 85 km level, Planet. Space Sci., **25**, 265-273, 1977.
- Noxon, J.F., Effects of internal gravity waves upon night airglow temperatures, Geophys. Res. Lett., **5**, 25-27, 1978.
- Peterson, A.W., and G.W. Adan, OH airglow phenomena during the 5-6 July 1982 total lunar eclipse, Appl. Optics, **22**, 2682-2685, 1983.
- Swenson, G.R., S.B. Mende, and S.P. Geller, Fabry-Perot imaging of OH(8-3): Rotational temperatures and gravity waves, J. Geophys. Res., **95**, 12251-12263, 1990.
- Taylor, M.J., M.A. Hapgood, and P. Rothwell, Observations of gravity wave propagation in the OI (557.7 nm), Na (589.2 nm) and the near infrared OH nightglow emission, Planet. Space Sci., **35**, 413-427, 1987.
- Taylor, M.J., P.J. Espy, D.J. Baker, R.J. Sica, P.C. Neal, and W.R. Pendleton Jr., Simultaneous intensity, temperature, and imaging measurements of short period wave structure in the OH nightglow emission, Planet. Space Sci., "in press", 1991.
- Turnbull, D.N., and R.P. Lowe, Temporal variations in the hydroxyl nightglow observed during ALOHA-90, Geophys. Res. Lett., this issue, 1991.
- Viereck, R.A., and C.S. Deehr, On the interaction between gravity waves and the OH Meinel (6-2) and the O₂ Atmospheric (0-1) bands in the polar night airglow, J. Geophys. Res., **94**, 5397-5404, 1989.

(Received April 5, 1991;
accepted May 7, 1991.)

Copyright 1991 by the American Geophysical Union.

List of Figures

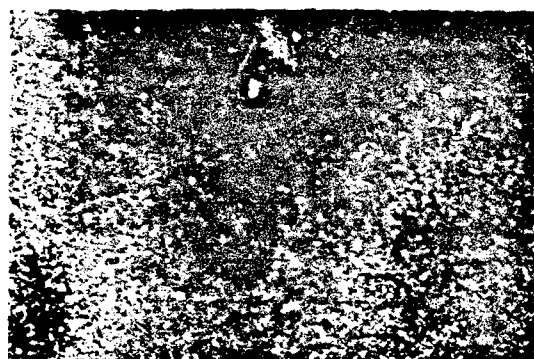
Fig.1. Series of CCD images showing small scale wave structure in the near infrared zenith nightglow emissions. Each image has been flat fielded and color enhanced to highlight the wave features. The structures appear mainly yellow-green but brighter features are red. The camera was aimed at an azimuth of 280° and the near east-west aligned waves are almost vertical in the images.

Fig.2. Relative intensity of (a) the OH (3,1) band recorded by the spectrometer using a 30° circular field of view and, (b) the broad band NIR structure derived from the CCD images using a 30° square sample area.

Fig.3. Relative intensity of the CCD data determined using a 5° square sample area. For comparison the data are plotted on the same scales as Figure 2.

TABLE 1. Dates and times when NIR structure was imaged in the zenith by the CCD camera.

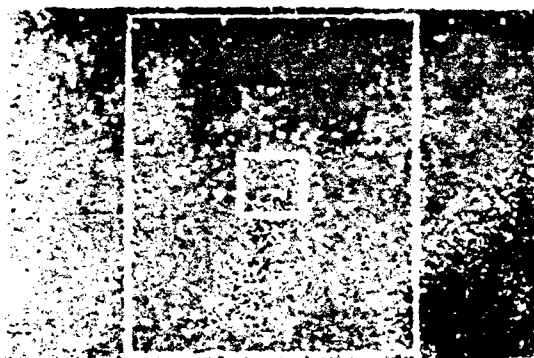
DAY	DATE	TIME (UT)
081	22/3	15:30
082	23/3	14:53
087	28/3	15:16
089	30/3	12:22 - 12:59
090	31/3	09:50 - 10:00
		13:00 - 14:51
092	02/4	12:19 - 12:56



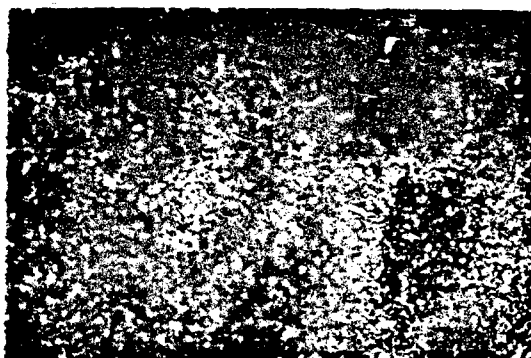
13:14 UT



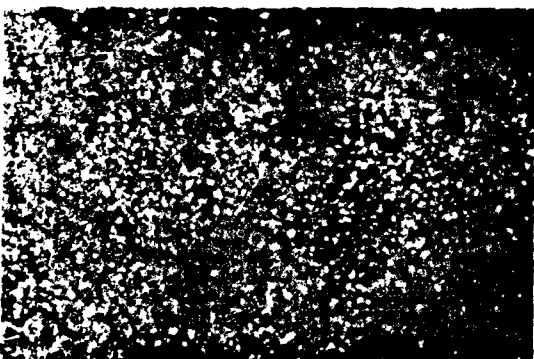
13:18



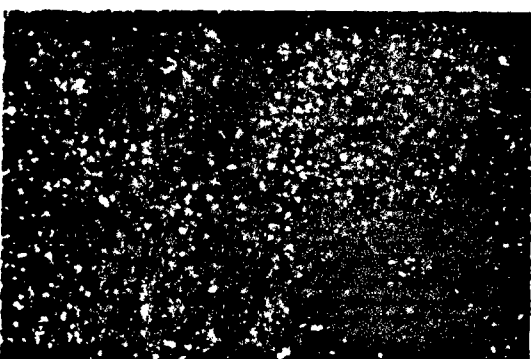
13:22



13:26



13:30



13:34

Figure 1 - Series of CCD images showing small scale wave structure in the near infrared zenith nightglow emissions. Each image has been flat fielded and color enhanced to highlight the wave features. The structures appear mainly yellow-green but brighter features are red. The camera was aimed at an azimuth of 280° and the near east-west aligned waves are almost vertical in the images.

ALOHA '90 Day 090

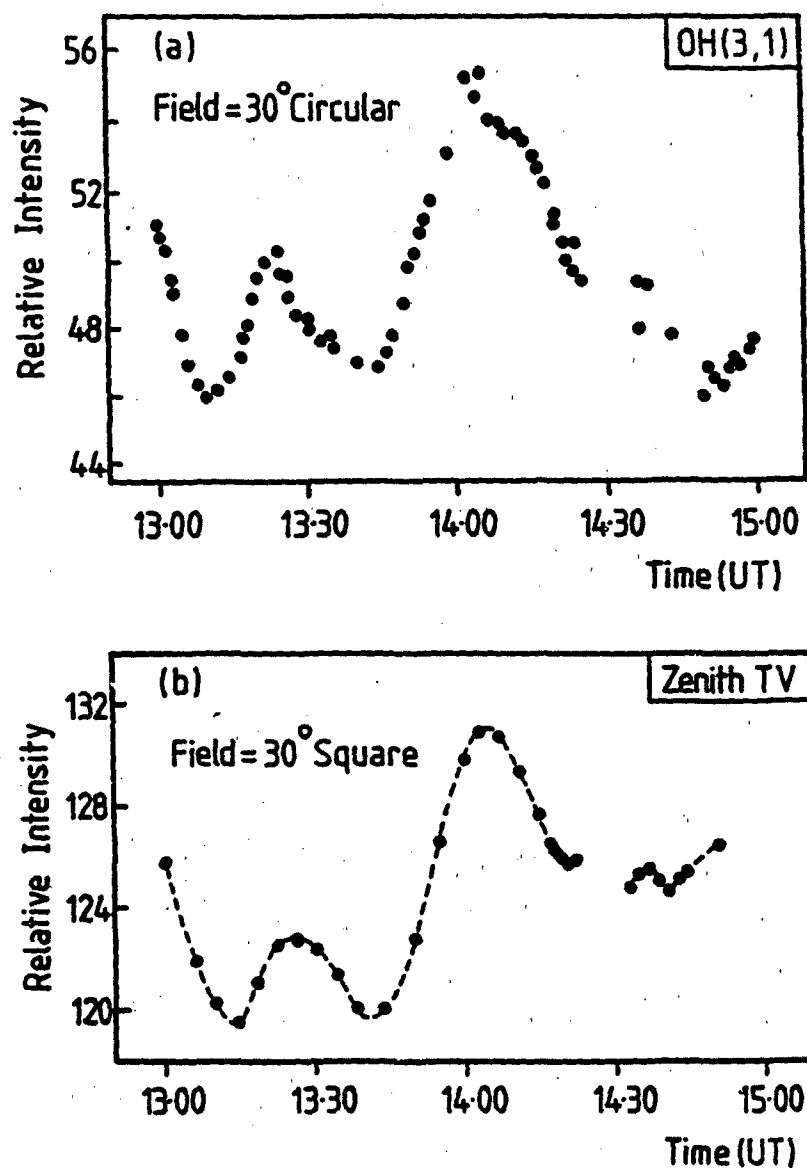


Figure 2 - Relative intensity of (a) the OH (3,1) band recorded by the spectrometer using a 30° circular field of view and, (b) the broad band NIR structure derived from the CCD images using a 30° square sample area.

ALOHA '90 Day090

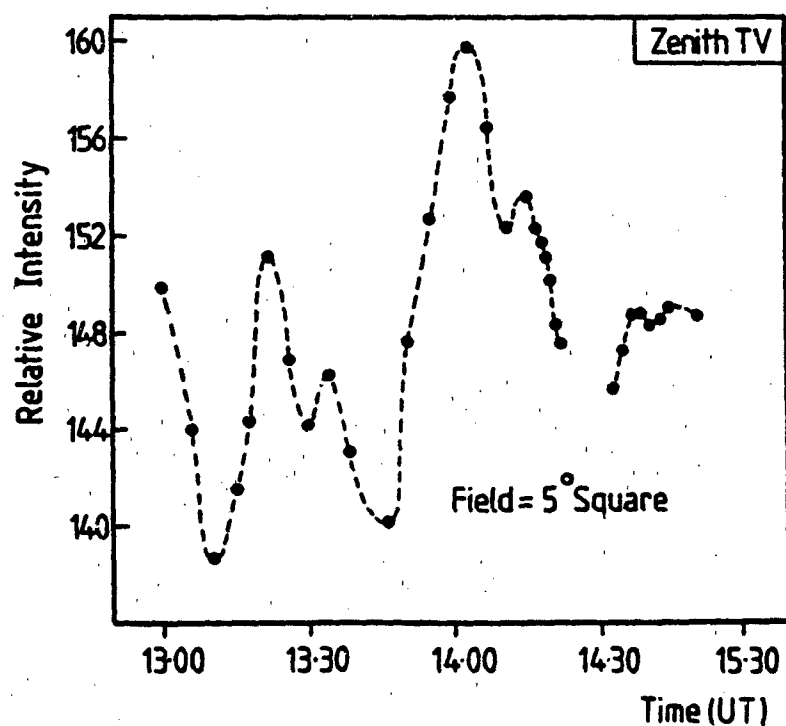
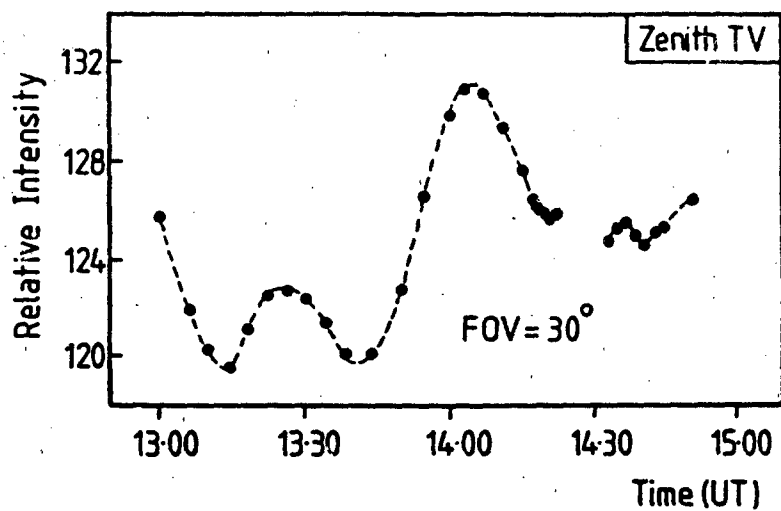


Figure 3 - Relative intensity of the CCD data determined using a 5° square sample area. For comparison the data are plotted on the same scales at Figure 2.

MAPSTAR
The University of Western Ontario
London, Canada

Report on UWO Sub-Contract with University of Cincinnati

Principal Investigator: R. P. Lowe

Period: 01 Feb 90 to 30 June 90

Project Name: Airglow Measurement Campaign, Hawaii

INTRODUCTION

This sub-contract was set-up to pay partial field costs (shipping, travel and living) of University of Western Ontario participation in the ALOHA '90 campaign of co-ordinate observations of mesopause region waves under the direction of Professor Chet Gardner, University of Illinois. Additional funding was provided by MAPSTAR/Utah State (data-processing and interpretation) and the Institute for Space and Terrestrial Sciences (salaries and additional travel and living).

SUMMARY OF FIELD ACTIVITIES

UWOMI-I, a Fourier transform interferometer was shipped to Maui for installation at the summit of Haleakela on March 22, 1991. It was seriously damaged in shipment and required extensive repairs before being put in operation on March 25. It remained on the summit until April 11, 1991. The system computer was damaged in a lightning storm on April 5, and attempts to repair it were unsuccessful. Eight nights of data were obtained consisting of over 7000 individual airglow spectra.

D. N. Turnbull (UWO/ISTS) was in charge of field operations and remained on site throughout the period of operations. P. Meier (UWO/ISTS) was present for the first week of operations to aid in initial set-up and service the damaged instruments. R. P. Lowe (UWO) acted as observing assistant for the last ten days of the operation.

RESULTS

All data has been processed and interpreted. Three papers based on the results obtained combined with those of other campaign participants will appear in a special issue of Geophysical Research Letters to be published in late 1991.

**END
FILMED**

DATE:

1-92

DTIC